Polynuclear metal clusters using polyalkoxide ligands

Thesis Submitted in Accordance with the Requirement of The University of Edinburgh for the Degree of Doctor of Philosophy

By

Georgios Karotsis

Supervised by Dr Euan K. Brechin

School of Chemistry
Faculty of Science and Engineering
University of Edinburgh
November **2010**

Dedication

This thesis is dedicated to Fr Raphael Pavouris, Fr John Maitland and Fr Avraamy Newman for always trying to give me what I really needed.

Declaration

I hereby declare that except where specific reference is made to other sources, the work contained in this thesis is the original work of the author. It has been composed by the candidate and has not been submitted, in whole or in part, for any other degree, diploma, or other qualification.

Georgios Karotsis

November 2010

Acknowledgements

My supervisor, Dr. Euan Brechin, deserves my utmost gratitude for his unending support, encouragement, and guidance. His patience, dedication to the field, and genuine interest in my work fuelled the results achieved in this thesis. A fine Scotsman, it was a privilege to work with Euan, and as such, I leave the University of Edinburgh with great memories. "Boss, when it comes to managing your group, you make Sir Alex Ferguson look like an amateur."

I am grateful to Dr. Constantinos Milios for introducing me not only to Dr. Euan Brechin, but also to the field of Molecular Magnetism. A great friend with tremendous patience and charisma, Costas has a phenomenal ability to transmit knowledge. Despite the fact that he supports the wrong football club, I look forward to many more meetings in Mike's…

My second supervisor, Prof. Simon Parsons, supported me on countless occasions. Not only is he a master in his field, Simon is a true gentleman.

Collaboration with Dr. Scott Dalgarno led to the achievement of everything that is published here in chapter two. Not only did Scott introduce me to the fascinating world of Calixarenes, but his enthusiasm for our work kept me motivated.

I would like to thank Dr. Giannis Papaefstathiou for his collaboration, guidance, and friendship. His expertise in characterizing extended networks was integral in writing chapter four. The meetings we had in Mike's Pub were very inspirational.

Dr. Wang Yi became like a brother to me. There are no words to describe the all-around support and friendship he provided. A great cook, running partner, and master of all things PC-related, Yi carried me through the tough times. He is the perfect combination of good gentle character and sharp intelligence. I could not have made it without Yi, and for that (plus three visits to Hellas so far), he is an honorary Hellene.

The individuals making up the Brechin Group became my second family. Dr. Maria Manoli supported me in the early stages of my research, and aside from entertaining us, she kept the lab tidy. Dr. Ian Gass, a.k.a 'Iron Man', taught me many things, not the least of which was how to look good in a kilt at his wedding. During his time as a post-doc with our group, Dr. Leigh Jones, a fine Welshman, assisted me in analyzing the results listed here in chapters three and four. Apart from being a good scientist, he is also an impressive football player and I hope his club Liverpool will see better days. Dr. Ross Inglis tolerated my 'loudness' in the lab, and I hope that he will now enjoy peace and quiet. His taste in movies is exceptional; however unfortunately, this is not the case with his taste in music. One day, I hope to attend another Cowdenbeath match with him. (Soon to be) Dr. Kevin Mason must be thanked for helping us win both the ChemSoc and St. Andrews Football Tournaments. The door is always open for you to again visit Athens. I want to thank Dr. Alessandro Prescimone for his hospitality in Pisa, and for providing assistance with Crystalography. Finally, I wish the best of luck to Tom and Stephanie, the newest members of the Brechin Group. I am sure they will enjoy their time as much as I did.

I am grateful to Dr. Marco Evangelisti for his assistance with MCE measurements and to Prof. Wernsdorfer Wolfgang for the single-crystal hysteresis and relaxation measurements. Sylvia Williamson also assisted with elemental analysis.

Derek, Raymond, John, and Tim always did their best to provide me with resources from the Chemistry stores. I am grateful to Stuart, the finest glass blower in Scotland, and Davy, the best equipment engineer, for keeping my pumps in good condition.

I am thankful to: Alex, Jason, Augustino, Bea and Manuel for their support and friendship and Nao 'The Prize' Valentino.

My family, the Karotsis clan, for constantly and selflessly giving me the support, love, and resources necessary to meet my goals.

I am indebted to the Orthodox Community of Edinburgh for being there…

Abstract

We have investigated the use of calix[4]arenes in 3*d* and 3*d*/4*f* chemistry which produced a family of 7 new complexes. These are: $[Mn^{III}_2Mn^{II}_2(OH)_2(TBC4)_2(DMF)_6]$ **(1)** , the analogous version with C4 **(2)**. $[Mn^{III}_4Gd^{III}_4(OH)_4(C4)_4(NO_3)_2(DMF)_6(H_2O)_6](OH)_2$ **(3)**, $[Mn^{III}_4Tb^{III}_4(OH)_4(C4)_4(NO_3)_2(DMF)_6(H_2O)_6](OH)_2$ **(4)**, $[Mn^{III}_4Dy^{III}_4(OH)_4(C4)_4(NO_3)_2(DMF)_6(H_2O)_6](OH)_2$ **(5)**, $[Cu^{II}_9(OH)_3(TBC4)_3Cl_2(DMSO)_6](Cu^{I}Cl_2)\cdot DMSO$ (6·DMSO) **(6)** and $[Cu^{II}_9(OH)_3(TBC4)_3(NO_3)_2(DMSO)_6](NO_3)\cdot$ DMSO (7·DMSO) **(7)**.

We continued with a series of Pseudo Metallocalix[6]arene planar disc complexes : $[Ni_7(OH)_6(L_1)_6](NO_3)_2$ **(8)**, $[Ni_7(OH)_6(L_1)_6](NO_3)_2.2MeOH$ **(9)**, $[Ni_7(OH)_6(L_1)_6](NO_3)_2.3MeNO_2$ **(10)**, $[Ni_7(OH)_6(L_2)_6](NO_3)_2.2MeCN$ **(11)**, $[Zn_7(OH)_6(L_1)_6](NO_3)_2.2MeOH.H_2O$ **(12)** and $[Zn_7(OH)_6(L_1)_6](NO_3)_2.3MeNO_2$ **(13)** and in the final part of this thesis we present a family of tetranuclear mixed valent Mn complexes using the tripodal ligand $heedH_2$: $[Mn^{II}_2Mn^{IV}_2O_2(heed)_2(EtOH)_6Br_2]Br_2$ **(14)**, $[Mn^{II}_2Mn^{IV}_2O_2(heed)_2(H_2O)_2Cl_4]$ **(15)**, $[Mn^{II}_2Mn^{IV}_2O_2(heed)_2(heedH_2)_2](ClO_4)_4$ **(16)**, $[Mn^{II}_2Mn^{IV}_2O_2(heed)_2(MeCN)_2(H_2O)_2(bpy)_2](ClO_4)_4$ **(17)**, $[Mn^{II}_2Mn^{IV}_2O_2(heed)_2(bpy)_2Br_4]$ **(18)**; and the 2-D network of tetranuclear $Mn^{II/IV}$ clusters $\{[Mn^{II}_2Mn^{IV}_2O_2(heed)_2(H_2O)_2(MeOH)_2(dca)_2]Br_2\}_n$ **(19)**. In total nineteen new complexes are reported. Studies of the magnetic properties show that **1** and **2** are SMM's, whilst complex **3** is an excellent magnetic refrigerant for low-temperature applications and **4** and **5** behave as low-temperature molecular magnets.

Abbreviations

ac	Alternating current
AFM	Antiferromagnetic
BVS	Bond Valence Sum
C4	Calix[4]arene
D	Zero Field Splitting Parameter
dc	Direct current
EPR	Electron Paramagnetic Resonance
EXAFS	Extended X-RayAbsorption Fine Structure
FM	Ferromagnetic
heedH2	N,N-bis(2-hydroxyethyl)ethylene diamine
MCE	Magnetocaloric Effect
OEC	Oxygen-Evolving Complex
PSII	Photosystem II
QTM	Quantum Tunnelling of the Magnetisation
s.e	Symmetry equivalent
SMMs	Single Molecule Magnets
SQUID	Superconducting quantum interference device
TBC4	p-^{t}But-calix[4]arene
ZFS	Zero field splitting

Table of Contents

Chapter 1 Introduction

This thesis describes the syntheses, structures and characterisation of a number of polynuclear cluster compounds using polyalkoxide-type ligands. Particular attention is given to their magnetic properties, since some behave as Single-Molecule Magnets (SMMs) or magnetic coolers. The importance of Mn-containing clusters, their origins in the field of bioinorganic chemistry and their development into nanomagnets and nanocoolers is discussed, together with the various strategies employed for their synthesis.

Manganese Cluster Chemistry

Mn cluster chemistry evolved approximately 30 years ago and continues to grow to this day. Its origins lie in biochemistry since Mn clusters are found in the active sites of a number of enzymes such as superoxide dismutase (mononuclear Mn site), catalases (dinuclear Mn) and the Oxygen-Evolving Complex (OEC) of photosystem II (PSII).[1] The goal for the synthetic chemist in this field is thus to synthesise model complexes that can reproduce – at least to some extent – the physical [be they structural, spectroscopic, magnetic or redox] properties of the naturally occurring material in order to understand the underlying chemistry, physics and biology present, with the ultimate aim of reproducing their function. The specific design and synthesis of tetranuclear Mn clusters, although of interest from a spin frustration perspective (*vide infra*), has mainly been pursued in order to make models for the complex responsible for the oxidation of water in the OEC of PSII in green plants and cyanobacteria. Recent crystallographic and polarised EXAFS studies on the PSII reaction centre of *Thermosynechococcus elongates* confirm the cluster to be an oxide-bridged [Mn_4Ca] complex with (mainly) peripheral carboxylate ligation (Figure 1). The protein environment and one chloride anion also play a crucial role for the water splitting activity. The [Mn-Ca] complex, as can be observed from the electron density map in Figure 1, displays two distinct regions of electron density: one larger spherical region which contains four metal ions of a similar size to manganese which are placed at the apices of a tetrahedron, and one smaller region which has one metal ion at its centre. One out of four metal centres in this larger region has been recognised as Ca^{2+}

with the cluster proposed to have the basic formula [Mn_3CaO_4]; this in turn is further connected to one additional Mn ion in the smaller region. Each oxygen atom in the [Mn_3CaO_4] cube-like cluster bridges three metal ions, with one also bridging to the "isolated" manganese ion. The Mn-Mn distances are ~2.7 Å, the Mn-Ca distances ~3.4 Å, and the distance between the "isolated" manganese centre and closest metal ions in the cluster unit is ~ 3.3 Å, typical for a Mn-O-Mn type bridge.

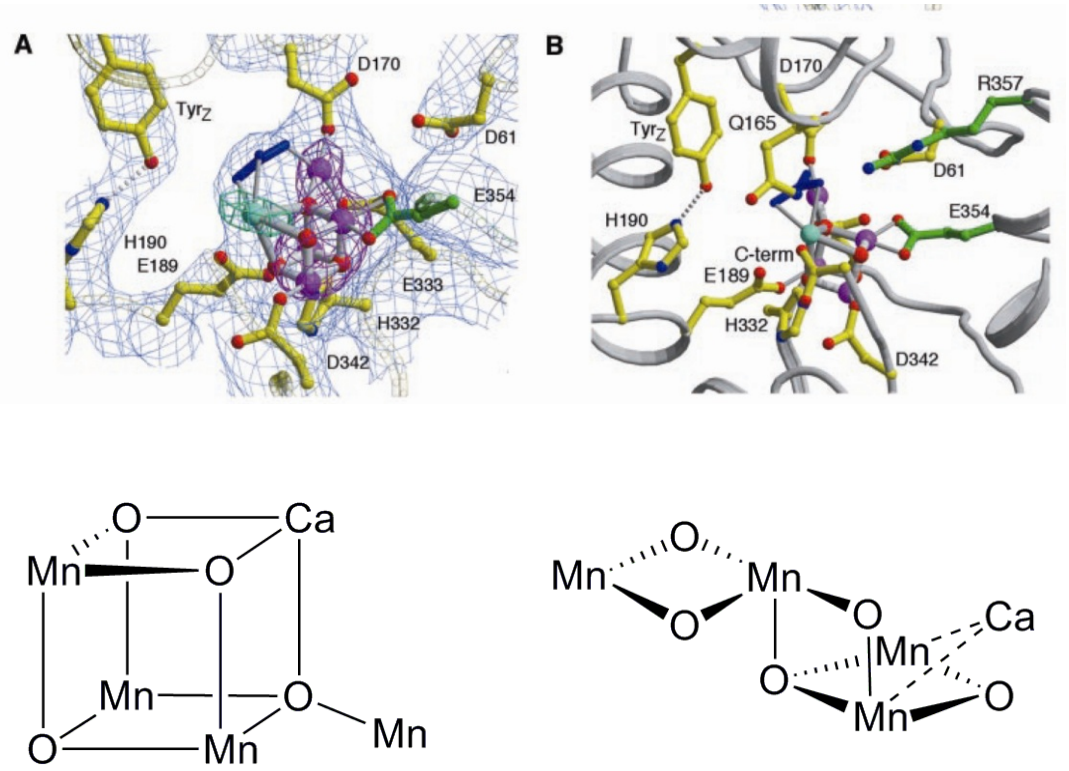

Figure 1: (Top) The single crystal X-ray structure of the OEC with (A) and without (B) the electron density map; pictures taken from Reference 2. (Bottom) A cartoon representation of the proposed metal-oxygen topology present in the [Mn_4CaO_4] cluster. Colour code: Mn = magenta, Ca = green

The link between this chemistry and the surge in activity in molecular magnetism probably stems from the Christou group who, in the 1980s, were particularly focussed on the synthesis of Mn clusters as models for the OEC in PSII. The work produced an enormous number of polymetallic mixed-valence Mn clusters – many of which actually contained [many] more than the four metals required for an accurate representation of the active site.[3] While attempting to make a [Mn_4] complex to model

the highest oxidation state of the biological cycle – via the reaction of $Mn(OAc)_2{\cdot}4H_2O$ with $KMnO_4$ – they instead accidentally isolated a dodecanuclear aggregate of formula $[Mn_{12}O_{12}(O_2CPh)_{16}(H_2O)_4]$. Strangely this was analogous to a complex published a decade earlier by Lis[4] who had reported the crystal structure and initial magnetic properties of $[Mn_{12}O_{12}(OAc)_{16}(H_2O)_4]$ (Figure 2), albeit without any attempt to interpret them. The magnetic properties of $[Mn_{12}O_{12}(O_2CPh)_{16}(H_2O)_4]$[5] were thoroughly investigated by Christou and co-workers who incorrectly deduced a spin ground state of $S = 14$ from SQUID magnetometry, which – at the time – would have been a world record value.[6] With hindsight we can say that this mistake was unsurprising because the magnetic properties of the cluster were like no other ever reported – indeed this was the dawn of Single-Molecule Magnetism.

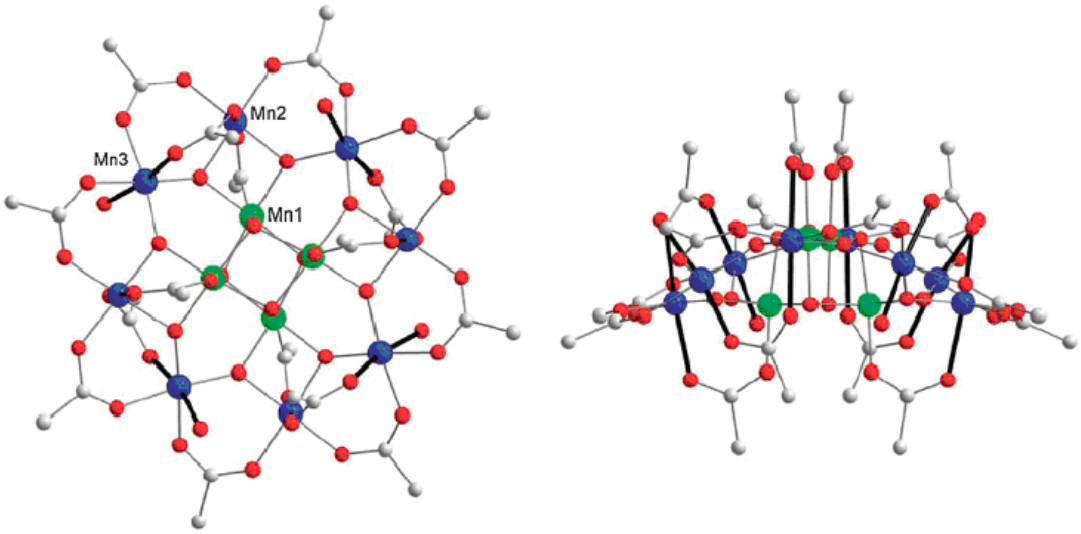

Figure 2. The molecular structure of $[Mn_{12}O_{12}(OAc)_{16}(H_2O)_4]$ and on the right the same molecular structure with emphasis on the orientation of the Mn^{3+} Jahn-Teller axis.

As a result of this paper an Italian group in Florence re-investigated the magnetic behaviour of Lis' $[Mn_{12}O_{12}(OAc)_{16}(H_2O)_4]$ via high field/frequency EPR spectroscopy in tandem with SQUID magnetometry[7] and correctly deduced a $S = 10$ ground state and a freezing of the magnetisation at low temperatures, analogous to that of super-paramagnets. This was thus the first "Single-Molecule Magnet (SMM) [although this phrase appeared later] and its discovery has inspired much beautiful chemistry and physics ever since (*vide infra*). Indeed there are several hundred papers on the $[Mn_{12}]$ complex and its analogues alone.

Background and General Magnetism Theory[8]

All substances exhibit diamagnetism ("dia" meaning "against" or "across"). As the name suggests a magnetic field applied to a purely diamagnetic material will induce a magnetic moment in that material which opposes the applied field. Paramagnetism ("para" meaning "with" or "along") is exhibited in materials with unpaired electrons. A magnetic field applied to a paramagnetic material will induce a magnetic moment in that material which aligns parallel to the applied field. Unpaired electrons have magnetic moments associated with them. If an electric field is applied to an unpaired electron, the lowest energy state that the electron can be in is that with its total angular momentum **J** (the sum of the orbital angular momentum **L** and spin angular momentum **S**) aligned with the magnetic field. Usually all electrons are paired. A pair of electrons will align antiparallel to one another, so they have no net magnetic moment. Substances in which all the electrons are paired are diamagnetic. If a substance has one or more unpaired electrons, these electrons will align with an applied magnetic field. Such a substance is paramagnetic (paramagnetic contributions to magnetisation are much larger than diamagnetic ones).

Exchange Interactions

Exchange interactions between unpaired electrons on paramagnetic metal centres within a polymetallic complex can occur in two ways: direct exchange and super-exchange. Either of these mechanisms can lead to ferromagnetic or antiferromagnetic (including canted antiferromagnetic) interactions (Figure 3).

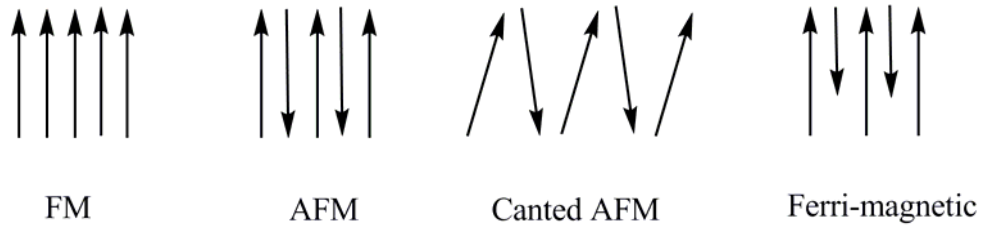

Figure 3: Ferromagnetic (FM), antiferromagnetic (AFM), canted antiferromagnetic and ferri-magnetic alignments of spins.

Ferromagnetic interactions are those in which the spins of electrons are induced to align parallel, and antiferromagnetic interactions are those in which the spins of electrons align antiparallel. Canting can occur in antiferromagnets where the spins do not align at exactly 180º so there is some overall magnetic moment even in the idealised 0 K case (Figure 3). As temperature is increased, thermal energy "scrambles" the spin directions causing exchange interactions to be nullified. Exchange interactions are vital in explaining short and long range order in materials in one, two or three dimensions. They also explain magnetic memory; if an array of spins are all ferromagnetically coupled, then when an applied field which has aligned the spins is switched off, there is some resistance to the spins relaxing into random directions.

Magnetic Anisotropy

Anisotropy means having properties that differ depending on the direction of measurement. The spins of unpaired electrons in metal ions can exhibit types of anisotropy (arising from distorted ligand fields and/or spin–orbit coupling), *i.e.* they can have preferential directions in which to point. There are three types of spin dimensionality: Heisenberg is totally isotropic *i.e.* spins can point in any direction with equal energy. XY spin refers to a system in which spins can point any direction in one plane (called the easy plane) with a lower energy than if they point out of the plane. Ising spin is a one dimensional spin: spins can point up or down along one axis (the easy axis) with a lower energy than pointing out of the axis. Anisotropy can occur in single ions (single ion anisotropy) and in larger molecular species and extended networks. In single ions anisotropy is usually equated with the presence of a triply degenerate (T) ground state, for example octahedral Co(II) [$^4T_1$ & $^4T_2$] and/or the

presence of a triply degenerate excited state that can mix with the ground state; a typical example of this is the Ni(II) ion.

Magnetisation and Susceptibility

When the spins of a substance are aligned, the sample is said to be magnetised. The magnetisation (M) of a paramagnet will increase as the field is increased and the spins align. When the spins are all aligned with the field the magnetisation of the sample is saturated, *i.e.* it has reached its saturation magnetisation (M_{sat}) the value of which depends on the number of unpaired electrons per molecule which can align with the field. For M_{sat} / μ_b mol^{-1} the relationship is given by Equation 1.

$$M_{sat} = gS \qquad \textbf{(1)}$$

The susceptibility of a substance is defined by the rate change of its magnetisation with respect to the change in field.

$$\chi = \frac{\partial M}{\partial H} \qquad \textbf{(2)}$$

At small field and high temperature this relationship can be approximated to:

$$\chi = \frac{M}{H} \qquad \textbf{(3)}$$

The susceptibility of a mole of substance, χ_m is made up of diamagnetic and paramagnetic contributions:

$$\chi_m = \chi_P + \chi_D \qquad \textbf{(4)}$$

The diamagnetic contribution is usually much smaller than the paramagnetic contribution, and is negative. This means that χ_p, the paramagnetic contribution to χ is always bigger than the molar susceptibility χ_m. The Curie law states that χ is inversely proportional to temperature:

$$\chi = \frac{C}{T} \qquad \textbf{(5)}$$

Where C is the Curie constant, defined as:

$$C = \frac{N_A g^2 \mu_b^2 S(S+1)}{3k_b} \qquad \textbf{(6)}$$

This in turn can be approximated to:

$$C = \frac{g^2}{8} S(S+1) \qquad \textbf{(7)}$$

Or for a system of n non-interacting metal ions:

$$C = \frac{g^2}{8} nS(S+1) \qquad \textbf{(8)}$$

For experimentally determined C an estimate of g can be obtained by simply rearranging (8):

$$g = \sqrt{\frac{8C}{nS(S+1)}} \qquad \textbf{(9)}$$

The Curie law was modified by Weiss to afford the Curie-Weiss Law which is applicable to materials with exchange interactions or magnetic anisotropy:

$$\chi = \frac{C}{T - \theta} \qquad \textbf{(10)}$$

Where θ is the Weiss constant; the sign of which indicates the type of exchange interaction present (negative for antiferromagnets, positive for ferromagnets).

Single Molecule Magnet Theory

Single-Molecule Magnets (SMMs) are molecules which exhibit some magnetic memory. Any molecule containing unpaired electrons can be magnetised upon the application of a field. Usually in the absence of a magnetic field, the m_s sub levels (of the ground state of the molecule) corresponding to different angular momentum orientations of the unpaired electrons (Figure 4) become degenerate, and are all equally populated, *i.e.* the electrons have no preference for the direction in which they point and thus the magnetisation of the sample is zero.

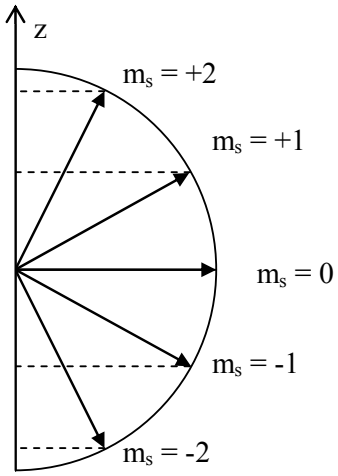

Figure 4. The m_s sub levels corresponding to different angular momentum directions of the unpaired electrons when the magnetic field is switched off.

However, a consequence of Ising-like (or axial) anisotropy is that the energies of different m_s sublevels may split - even in zero field. This zero field splitting (ZFS) is described by the axial ZFS parameter, D. The energies of the different m_s levels at zero field depend on D:

$$E = Dm_s^2 \qquad \textbf{(11)}$$

Consequently, an increase in $|D|$ or S increases the energy barrier (E or sometimes U) to the relaxation of the magnetisation from "up" to "down". It is difficult to predict the exact value [or sign] of $D_{molecule}$ however, though it has become apparent that relatively large values of D occur for molecules which have an anisotropic shape and include ions which exhibit substantial single ion anisotropy (d_{ion}). The splitting of the

m_s levels with a magnetic field (the Zeeman effect) increasing from zero (in the z direction) is shown in Figure 5.

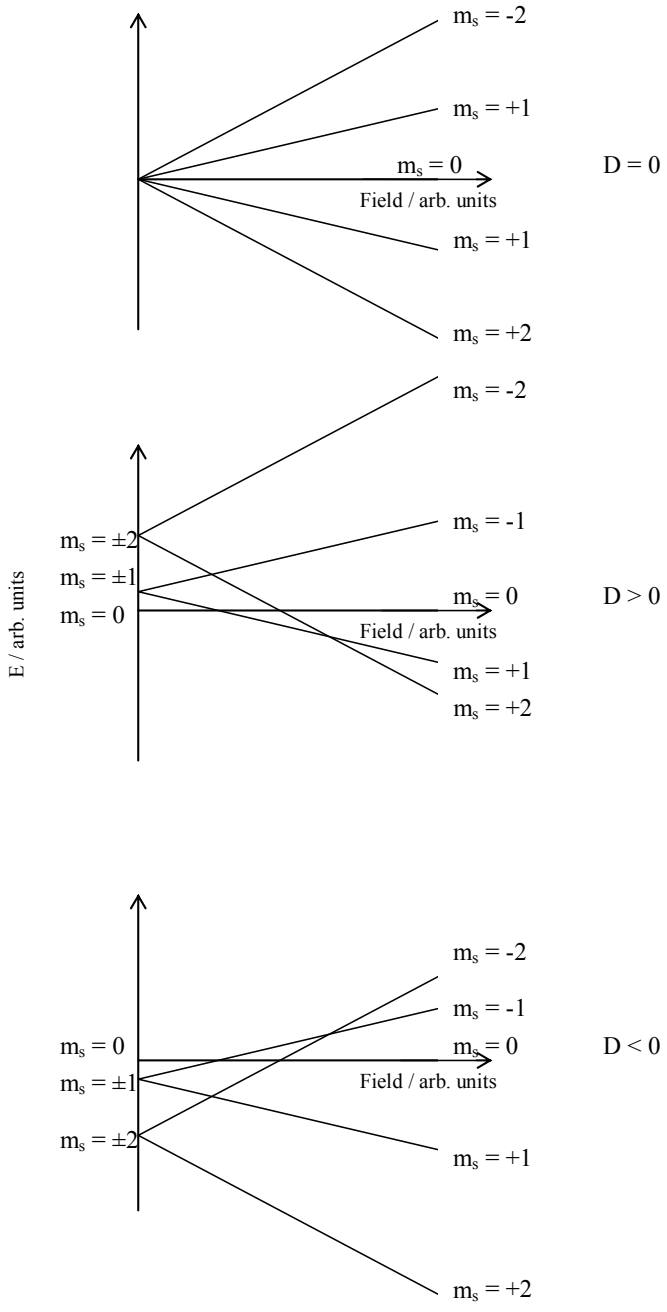

Figure 5 Splitting of the m_s levels with a magnetic field increasing from zero in the z direction.

If a sample with positive *D* is magnetised the spins will occupy the lowest energy state which, in the high field limit, is the m_s value which points in the direction of the field. In the case illustrated in Figure 5 this is $m_s = +2$. When the field is removed, the

spins can easily relax to the $m_s = 0$ level. However if D is negative then on removing the field the electrons must overcome the energy barrier between $m_s = +2$ (again using the example in Figure 5) and $m_s = 0$. The temperature below which this relaxation cannot occur spontaneously is called the blocking temperature (T_B). For integer spins this energy barrier is equal to Dm_s^2. When the energies of two m_s levels are coincident quantum tunnelling of the magnetisation (QTM) can occur; this – as is shown in Figure 6 - provides an alternative mechanism for demagnetisation. That is, the magnetisation tunnels through the barrier rather than going up and over the barrier. Thermal activation to states higher in energy than the ground state results in fast tunnelling between energetically coincident states and hence classically forbidden transitions can take place.

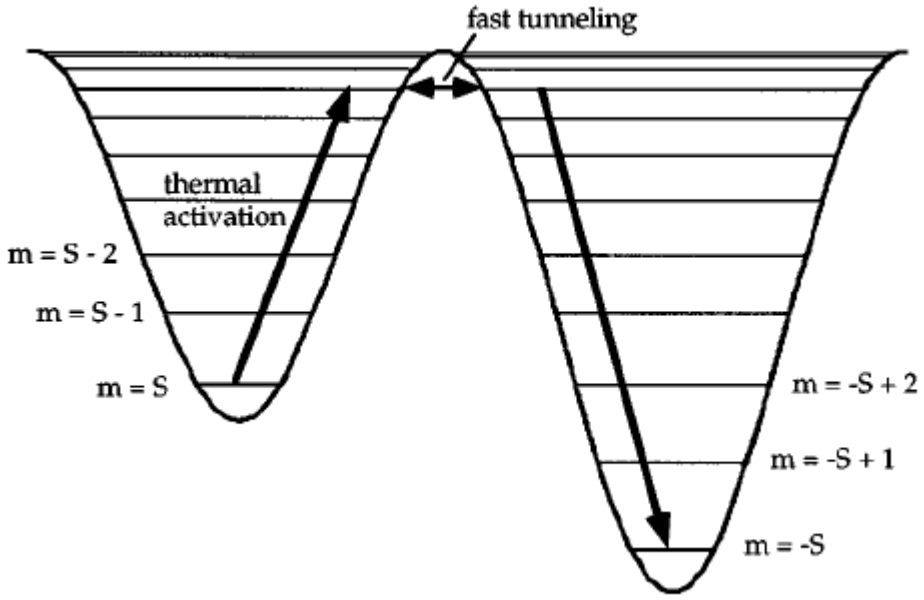

Figure 6: A schematic diagram illustrating the double well potential for SMMs. To travel from +*S* to –*S* the magnetisation must climb all the *Ms* rungs on the ladder before it can fall down the other side. An alternative to this thermally activated relaxation is QTM whereby the magnetisation can tunnel through the barrier between degenerate *Ms* levels.

Single Molecule Magnet History

For a SMM to have practical uses it must exhibit magnetic memory at temperatures close to room temperature, although specialist applications may become feasible at liquid nitrogen temperatures.[9] Values of U_{eff} (the effective barrier to magnetisation reversal) are typically below 70 K and this corresponds to the observation of

hysteresis loops in magnetisation versus field studies (the ultimate proof of SMM behaviour) at temperatures of only ~4 K (the blocking temperature, T_B) because of thermal population of levels other than the ground state at higher temperatures. A large amount of the work on SMMs is therefore aimed at raising the blocking temperature to higher levels. The first SMM reported was the mixed oxidation state manganese cluster $[Mn_{12}O_{12}(OAc)_{16}(H_2O)_4]$ (Figure 2)[4]. This prototype cluster has been studied in great detail with a vast variety of techniques such as High-Field EPR[10], ^{1}H-NMR[11], ^{13}C-NMR[12], inelastic neutron scattering[13] and magnetic circular dichroism[14] resulting in the publication of several hundred papers .The magnetisation of the Mn_{12} cluster is highly anisotropic and its relaxation time at very low temperatures becomes of the order of several years, giving rise to pronounced hysteresis loops below approximately 4 K . Perhaps more important than any proposed application is the fact that this molecule was the first object that truly straddled the classical/quantum interface and as such it provided scientists with an ideal system with which to investigate theoretically predicted quantum effects. For example, the first ever experimental observation of QTM and the first detailed descriptions of the dynamics of magnetisation relaxation. [15,16]

There are now several hundred SMMs and this introduction does not attempt to summarise these, simply because it would be impossible to do so or to do justice to the field, rather the attention of the reader is directed to the several excellent review articles[17] and books[18] recently published. Although SMMs are now known with several different transition metal (the majority are 3d metals[19] though some 4f[20] and 5d[21] examples are known) and lanthanide ions[22], the vast majority (approximately 80 %) involve Mn. This is due to two important factors. The first is that Mn in the 3+ oxidation state and in octahedral geometry exhibits a Jahn-Teller (JT) distortion. The JT distortion can be easily identified through X-ray crystallography by an elongation or compression of one of the axes of the octahedron compared to the other two axes (Fig 7). The reduction in symmetry is crucial because it increases the anisotropy of the ion (d_{ion}) and thus increases the anisotropy of the cluster ($D_{cluster}$), since to a crude approximation $D_{cluster}$ is a vectorial addition of d_{ion}. The second reason is that Mn in polymetallic clusters compounds is commonly found in three different oxidations states: Mn^{2+} (d^5), Mn^{3+} (d^4) and Mn^{4+} (d^3). Indeed it is far more common to see heterovalent Mn clusters than homovalent Mn clusters. This means that even if the

exchange interactions between nearest neighbours within the cluster are all antiferromagnetic (as they usually are) the net spin ground state is still likely to be non-zero. This affords Mn a huge advantage over its neighbours in the periodic table that have less oxidation state flexibility. Indeed in 2007 a compound of formula $[Mn_6O_2(Et\text{-}sao)_6(O_2CPh(Me)_2)_2(EtOH)_6])$ was the first to break the world record value of U_{eff} displayed by the prototype Mn_{12} molecule, displaying an energy barrier to magnetisation reversal of 86 K and a blocking temperature of 5 K[23].

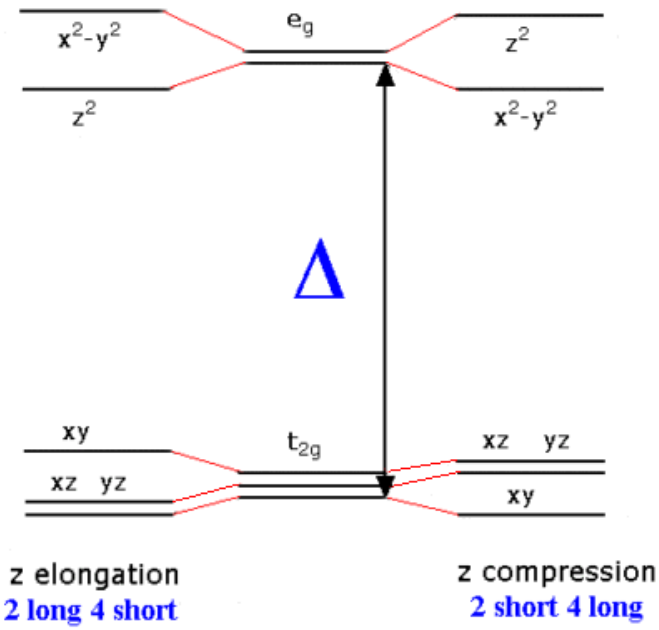

Figure 7: A schematic diagram illustrating Jahn Teller distortion and the effects upon orbital ordering of elongation and compression along the z-axis.

Magnetic Refrigerants

The high symmetry of many polynuclear clusters and the [related] observation that $D_{cluster}$ was often near zero, became a major obstacle for the creation of new SMMs with high effective energy barriers, despite the fact that chemists can regularly synthesise molecules with (very) large spin ground states (the current largest is S = 83/2[24]. Isotropic clusters with large spin ground states are however ideal candidates for displaying an enhanced magnetocaloric effect (MCE) and therefore have potential application as magnetic coolers[25]. The magnetocaloric effect is based on the

observation that the magnetic entropy S_m of a paramagnetic material changes when under the influence of an applied magnetic field. A spin S has $2S+1$ degeneracy in zero magnetic field and its magnetic entropy has a maximum value $S_m = R\ln(2S+1)$, where R is the gas constant. If a magnetic field H_f (Figure 8) is applied to the compound, (which is in a state of thermal equilibrium in a thermal bath at temperature T_i in magnetic field H_i) then the magnetic entropy will start to decrease isothermally. If the compound is thermally isolated and the field changes to H_f then adiabatic de-magnetisation occurs. When the total entropy of the system remains constant during the change in the magnetic field, ΔH, the change of magnetic entropy must be counter-balanced by an even but reverse change of entropy in the crystal, which results in a change in temperature ΔT_{ad} of the compound. If the change in the magnetic field decreases the entropy, then the change in temperature will be positive, alternatively if it increases the entropy, the change of temperature will be negative[26].

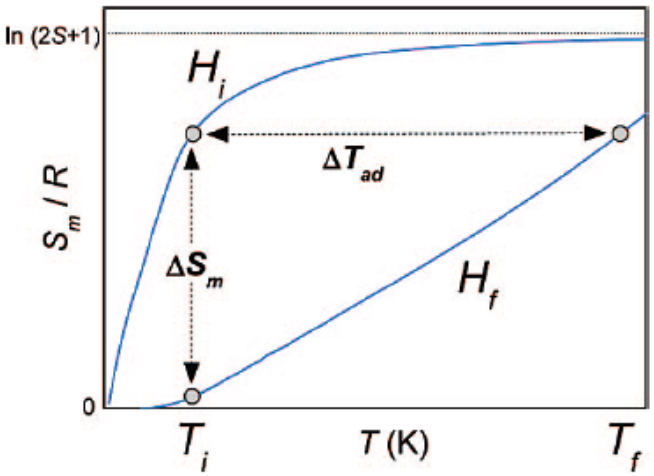

Figure 8: A schematic diagram illustrating magnetic entropy (S_m) as a function of temperature in two different magnetic fields H_i and H_f where $H_i<H_f$ for a paramagnet.

Recent studies have demonstrated that the MCE of selected molecular cluster compounds can be much larger than in the best, and conventionally studied, inter-metallic and lanthanide alloys, and magnetic nanoparticles.The recipe required for making such molecules has just been published[26] and in addition having a negligible anisotropy [which permits easy polarization of the net molecular spin], requires the presence of degenerate or low-lying excited spin states, since the so-added degrees of freedom result in extra magnetic entropy. In short, we must target high spin

(ferromagnetic) isotropic clusters displaying weak intra-molecular magnetic exchange. The [Mn_{12}] and [Fe_8] SMMs were the first to be investigated for magnetic refrigeration because of their well-defined S = 10 ground states, and although they displayed relatively large $-\Delta S_m$ values the large anisotropy present in both systems freezes the orientation of the molecular spins once the temperature is lowered below ~ 4K, limiting their applicability[26].The first isotropic molecular cluster studied was the heterometallic [Cr_7Cd] wheel,[27] but the problem in this case was the low value of the spin, S = 3/2. A huge step forward in the search for truly applicable molecular candidates was accomplished via the synthesis and study of highly-symmetric molecules with large values of the spin ground state. The first was [Fe_{14}] with an S = 25 ground state,[28,29] the second a ferromagnetic [Mn_{10}] supertetrahedron with S = 22 displaying practically zero anisotropy (Figure 9),[30] and the third a [Mn_{14}] disc[31]displaying a truly enormous enhancement of the MCE with values of $-\Delta S_m$ as large as 20 $Jkg^{-1}K^{-1}$ for liquid-helium temperatures and ΔB = 6 T - almost a factor of two larger than that of [$DyCo_2$] nanoparticles.[32]

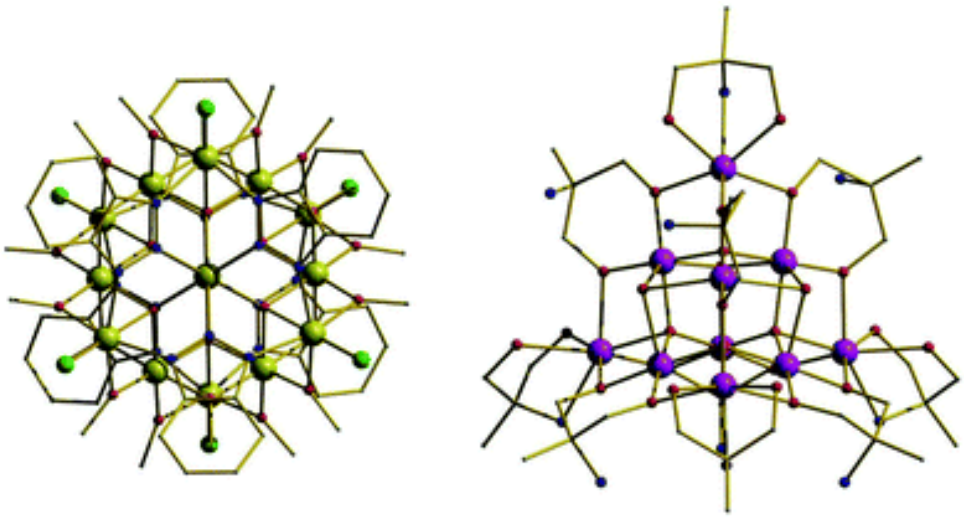

Figure 9. Molecular structures of Fe14 (left) and Mn10 (right). Yellow Fe, purple Mn, green Cl, red O, blue N.

Solvothermal Synthesis

Hydrothermal and solvothermal syntheses involve sealing reactants and water or some other solvent into a given volume and heating to temperatures above the solvent's boiling point. These high temperature and high pressure conditions can result in the

dissolution of species in solvents in which they would not normally dissolve, and large complex and highly symmetric molecules which may not be easily synthesised by other means can self-assemble. Hydrothermal synthesis has its origins in Geology where scientists were attempting to recreate the conditions within the earth's crust, and has been used successfully to synthesise quartz on an industrial scale[33].

Solvothermal synthesis allows reactants to pass through transition states that could not occur using conventional synthesis techniques at normal atmospheric pressure. Teflon lined autoclaves (Figure 10) provide inert containers in which reactions can proceed. These may not be heated above the melting point of Teflon (~250 ºC), though this rarely proves to be a significant drawback since such temperatures will likely also cause the decomposition of the organic ligands employed. Though now reasonably common in the synthesis of inorganic coordination polymers or MOFs the technique has been only sparingly employed for the synthesis of molecular inorganic coordination compounds[34].

Figure 12. High-pressure vessels used for hydrothermal synthesis.

Tripodal Alcohol Ligands

Tripodal alcohol ligands such as 1,1,1-tris(hydroxymethyl)ethane (H_3thme), 1,1,1-tris(hydroxymethyl)propane (H_3tmp) and pentaerythritol (H_4peol) (Scheme 1) were originally used by Zubieta and co-workers for the synthesis of [diamagnetic] oxovanadium and oxo-molybdenum clusters[35], but only sparingly for the synthesis of paramagnetic 3d transition metal clusters. The first example of the latter was a mixed-valent decametallic Mn cluster of formula $[(Et_4N)_2[Mn_{10}O_2Cl_8(thme)_6]$ whose structure is based on an edge-sharing bi-octahedron[36]. For some years now, the Brechin group has been building new polynuclear metal clusters, SMMs and magnetic coolers with tripodal alcohol ligands of general formula $RC(CH_2OH)_3$ (where R = H, CH_3, Et *etc*) and their many derivatives (Scheme 1). The disposition of the three alkoxide arms of the tri-anions of $RC(CH_2OH)_3$ pro-ligands direct the formation of triangular $[M_3]$ units where each arm of the ligand bridges one edge of the triangle. These triangular building blocks then self-assemble to form elaborate architectures (M_9 partial icosahedra, M_{10} supertetrahdra, Mn_{32} truncated cubes *etc*) whose topologies are dependent on reaction conditions and/or the presence of other bridging and/or terminal co-ligands such as carboxylates or β–diketonates *etc*.[37] A natural extension to these studies is the investigation of the coordination chemistry of analogous organic molecules in which one (or more) of the alcohol 'arms' is replaced by an alternative functional group(s), for example an amine group. While each alkoxide arm has the potential to bridge up to three metals (and thus a maximum of seven metals per tripodal ligand), the $–NH_2$ 'arm' is likely, if bonded, to act solely as a monodentate/terminal capping unit.

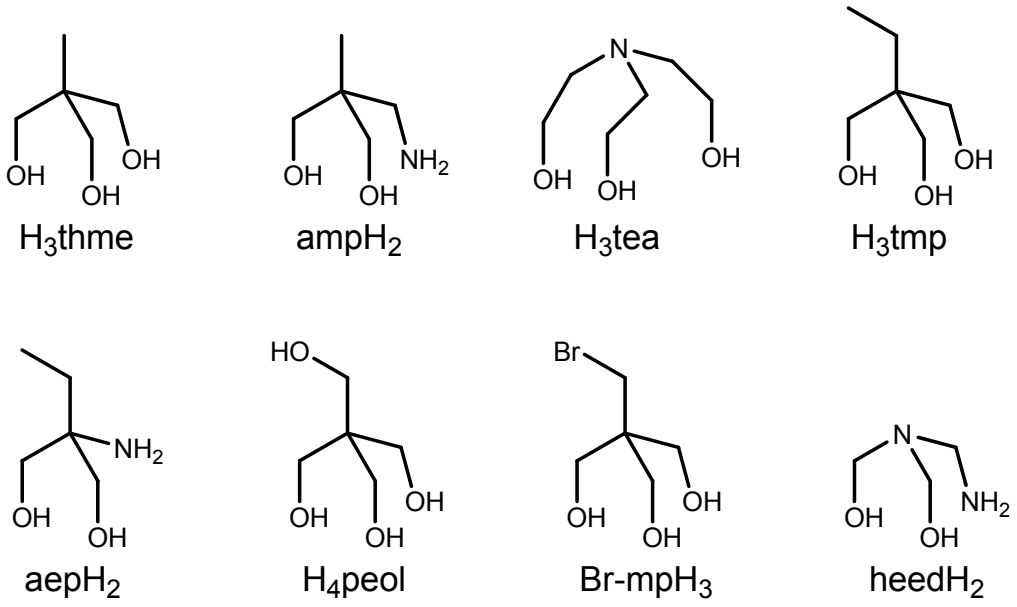

Scheme 1. The structures of 1,1,1-tris(hydroxymethyl)ethane (H_3thme); 2-Amino-2-methyl-1,3-propanediol ($ampH_2$); triethanolamine (H_3tea); 1,1,1-tris(hydroxymethyl)propane (H_3tmp); 2-amino-2-ethyl-1,3-propanediol ($aepH_2$); pentaerythritol (H_4peol); 2-(Bromomethyl)-2-(hydroxymethyl)-1,3-propanediol (Br-mpH_3); N,N-bis(2-hydroxyethyl)ethylene diamine ($heedH_2$).

The next logical step in this strategy is the use of tetrapodal alkoxides such as calix[4]arenes. Calix[4]arenes are cyclic molecules that have been used extensively in the formation of supramolecular structures and in various fields of coordination chemistry[38]. Calix[4]arene (C4, Scheme 2), is a cyclic polyphenol that is synthetically accessible on a large scale *via* the parent *p*-^{t}Bu derivative (TBC4), and this molecule is the typical starting point for synthetic alteration to the general molecular framework. In a bowl-conformation, the calix[4]arene polyphenolic pocket at the lower-rim is an attractive feature for metal complexation. Phenolic calixarenes display a tendency to form multinuclear metal ion complexes. Of the factors which determine the nuclearity of the clusters, the calixarene ring size and the capacity of the phenoxide donors to act as bridges are obviously important and offers prospects for considerable development of cluster chemistry. The polyphenolic nature of calix[n]arenes (where n = 4-8) also suggests they should be excellent candidates as ligands for the isolation of molecular nanomagnets, but to date their use in the isolation of paramagnetic cluster compounds is rather limited. The group of Luneau

has synthesised a dinuclear cobalt(II) complex with calix[8]arene exhibiting strong magnetic anisotropy of the cobalt(II) ions[39]and a series of $V^{III}V^{IV}_5$ compounds of formula $[V_6O_6(OCH_3)_8(TBC4)(ROH)]^-$ with *p-tert*-butylcalix[4]arene (TBC4) obtained under anaerobic solvothermal conditions[40].

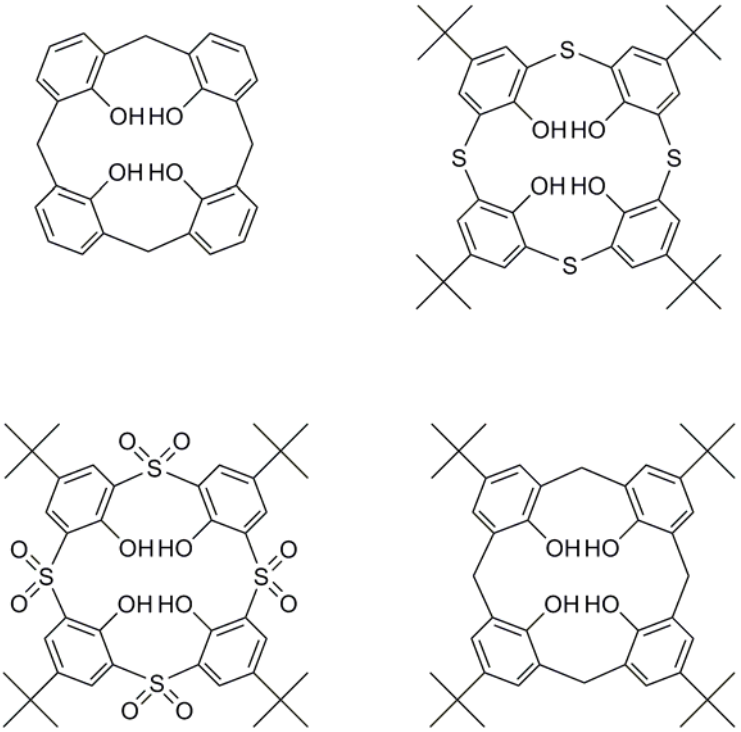

Scheme 2. The structures of calix[4]arene (C4), *p-tert*-butylthiacalix[4]arene, *p-tert*-butylsulfinylcalix[4]arene and *p-tert*-butylcalix[4]arene (TBC4) respectively.

Thiacalix[4]arenes, on the other hand, and their oxidised derivatives (Scheme 2) possess additional donor atoms and these have been widely used in the formation of a number of polynuclear transition metal or lanthanides clusters[41]. The additional donor atoms (relative to C4 or TBC4) around the molecular skeleton play a key role in supporting complex formation, taking part in the bonding within the metal cluster framework. Each thiacalix[n]arene possesses donor atoms both on the lower rim position and on the cyclic framework itself (-S-, -SO-, or -SO_2-). Larger and more flexible thiacalix[6]arenes can bind up to five metal ions inside the coordination cavity formed when it adopts the pinched cone conformation . Sulfonylcalix[4]arenes show a strong affinity for lanthanides ions with recent examples from the groups of Luneau[42] and Miyano[43].

Project Aims

The work described in this thesis is focused on the synthesis and structural and magnetic characterisation of polynuclear clusters using polyalkoxide ligands (such as Calix[4]arenes and heedH_2) for use as single-molecule magnets and magnetic coolers.

Physical Methods

Elemental analyses (C, H, N) were performed by the EaStCHEM microanalysis service. IR spectra were recorded as KBr pellets in the 4000-400 cm^{-1} range on a JASCO FT/IR-410 spectrometer. Variable temperature magnetic susceptibility (dc and ac) measurements were made on a Quantum Design MPMS-XL SQUID magnetometer equipped with a 7T magnet. Data were collected on powdered samples restrained in eicosane to prevent torquing. Diamagnetic corrections were applied using Pascal's constants. Magnetic studies below 1.8 K were carried out by Dr Wolfgang Wernsdorfer at the Institut Néel in Grenoble (http://neel.cnrs.fr/spip.php?rubrique51) on single crystals using a micro-SQUID apparatus operating down to 40 mK. Specific heat measurements were carried out and analysed by Dr Marco Evangelisti in CSIC, Zaragoza (http://icma.unizar.es/) using a Quantum Design Physical Property Measurement System (PPMS) setup for the $0<H<7$ T magnetic field range. Single crystal X-ray diffraction data were collected at 150 K on a Bruker Smart Apex CCD diffractometer equipped with an Oxford Cryosystems LT device, using Mo radiation. The structures were solved by direct methods (SHELXS) and refined by full-matrix least squares against F^2 (CRYSTALS) [44].

References

1 V.L.Pecoraro, Editor, Manganese redox enzymes, VCH, New York (1992)

2. K. Ferreira, T. M. Iverson, K. Maghlaoui, J. Barber and S. Iwata., *Science*, 2004, **303**, 1831

3. G. Christou, *Acc. Chem. Res*., 1989,22,328.

4. T. Lis, B. Jezowska-Trzebiaowska, *Acta Crystallogr,* 1977, B33,2112.

5. P. D. W. Boyd, Q. Li, J. B. Vincent, K. Folting, H. R. Chang, W. E. Streib, J. C. Huffman, G. Christou and D. N. Hendrickson, *J. Am. Chem. Soc.,* 1988, **110**, 8537.

6. A. Caneschi, D. Gatteschi, J. Laugier, P. Rey, R. Sessoli, C. Zanchini., *J. Am. Chem. Soc.,* 1988, **110**,2795.

7. A. Caneschi, D. Gatteschi, R. Sessoli, A. L. Barra, L. C. Brunel, M. Guillot, *J. Am. Chem. Soc*., 1991, **113**, 5873

8. S. Blundell, Magnetism in condensed matter, OUP, Oxford, 2001

9. W.Wernsdorfer, *Nature Materials*. **6**, 174-176.

10.(a) A. L. Barra, D. Gatteschi, R. Sessoli, *Chem-Eur. J.,* 2000, **06**, 1608. (b) A. L. Barra, *Appl. Magn. Reson*., 2001, 21, 619.

11. D. Procissi, B. J. Suh, A. Lascialfari, F. Borsa, A. Caneschi, A. Cornia, *J.Appl. Phys.,* 2002, **91**, 7173.

12. R. M. Achey, P. L. Kuhns, W.G. Moulton, A. P. Reyes, N. S. Dalul, *Polyhedron*, 2001, **20**, 1745.

13. S. Carretta, E. Liviotti, G. Amoretti, R. Caciuffo, A. Caneschi, D. Gatteschi, *Phys. Rev. B*. 2002, 65.

14. E. J. L. McInnes, E. Pidcock, V. S. Oganesyan, M. R. Cheesman, A. K. Powell, A. J. Thomson, *J. Am. Chem. Soc.,* 2002, **124**,9219.

15. J. R. Friedman, M. P. Sarachik, J. Tejada, J. Maciejewski, R. Ziolo, *J. Appl. Phys*. 1996, 79, 6031.

16. W. Wernsdorfer, R. Sessoli, *Science* 1999, **284**.

17. A. J. Tasiopoulos and S. P. Perlepes, *Dalton Trans*., **2008**, 5537

18. R. Winpenny, Editor, Single molecule magnets and related phenomena, Springer 2006.

19. C. Sangregario, T. Ohm, C. Paulsen, R. Sessoli, D. Gatteschi, *Phys. Rev. Lett*. 1997, 78, 4645 (b) H. Andres, R. Basler, A. J. Blake, E. K. Brechin, C. Cadiou, G.

Chaboussant, C. M. Grant, H. U. Gudel, S G. Harris, M. Murrie, S. Parsons, C. Paulsen, F. Semdini, V. Villar, W. Wernsdorfer, R. E. P. Winpenny, *Chem.Eur. J*. 2002, **08**, 4867 (c) Z. Sun, D. N. Hendrickson, C. M. Grant, S. L. Castro, G. Christou, *Chem. Commun*. 1998, 721.

20. (a) S. Osa, T. Kido, N. Matsumoto, N. Re, A. Pochaba, J. Mrozinski, *J. Am. Chem. Soc.,* 2004, **126**,420. (b) C. M. Zaleski, E. C. Depperman, J. W. Kampf, M. L. Kirk, V. L. Pecoraro, *Angew. Chem. Int. Ed*. 2004, **43**, 3912. (c) A. Mishra, W. Wernsdorfer, K. A. Abboud and G. Christou, *J. Am. Chem. Soc.,* 2004, **126**,15648. (d) A. Mishra, W. Wernsdorfer, S. Parsons, G. Christou, E. K. Brechin, *Chem. Commun*., 2005, 2086
21. E. J Schelter, A. V. Prosvirin, K. R. Dunbar, *J. Am. Chem. Soc.,* 2004, **126**,15004.
22. (a) N. Ishikawa, M. Sugita, W. Wernsdorfer, *J. Am. Chem. Soc.,* 2005, **127**,3650; (b) N. Ishikawa, M. Sugita, W. Wernsdorfer, *Angew. Chem. Int. Ed*. 2005, **44**, 2931.
23. C. J. Milios, A. Vinslava, W. Wernsdorfer, S. Moggach, S. Parsons, S. P. Perlepes, G. Christou, E. K. Brechin, *J. Am. Chem. Soc.,* 2007, **129**,2754.
24. A. M. Ako, I. J. Hewitt, V. Mereacre, R. Clerac, W. Wernsdorfer, C. E. Anson, A. K. Powell, *Angew. Chem. Int. Ed*. 2006, **30**, 2754.
25. For a review see: M. Evangelisti, F. Luis, L. J. de Jongh, M. Affronte*, J. Mater. Chem*., 2006, 16, 2534.
26. M. Evangelisti, E. K. Brechin, *Dalton Trans*., 2010, **39**, 4672.
27. M. Affronte, A. Ghirri, S. Carfetta, G. Amoretti, S. Piligkos, G. A. Timco and R. E. P. Winpenny, *Appl. Phys. Lett*., 2004, **84**, 3468.
28. M. Evangelisti, A. Candini, A. Ghirri, M. Affronte, E. K. Brechin, E. I. J. McInnes, *Appl. Phys. Lett*., 2005, **87**, 72504.
29. R. Shaw, R. H. Laye, L. F. Jones, D. M. Low, C. T. Eeckelaers, Q. Wei, C. J. Milios, S. Teat, M. Helliwell, J. Raftery, M. Evangelisti, M. Affronte, D. Collison, E. K.Brechin, E. J. L. McInnes, *Inorg. Chem*., 2007, **46**, 4968.
30. M. Manoli, R. D. L. Johnstone, S. Parsons, M. Murrie, M. Affronte, M. Evangelisti, E. K. Brechin, *Angew. Chem. Int. Ed*. 2007, **46**, 4456.
31. M. Manoli, A. Collins, S. Parsons, A. Candini, M. Evangelisti, E. K. Brechin, *J. Am. Chem. Soc.,* 2008, **130**,11129.
32. S. Ma, W. B. Cui, D. Li, N. K. Sun, D. Y. Geng, X. Jiang, Z. D. Zhang, *Appl. Phys. Lett.*, 2008, 92, 173113.

33. A. Rabeneau, *Angew. Chem. Int. Ed*. *Engl*. 1985, **24**, 1026.

34. R. H. Laye, , E. J. L. McInnes, *Eur. J. Inorg. Chem*., 2004, **14**, 2811

35. M. I. Khan, J. A. Zubieta, *Prog. Inorg.Chem*., 1995, **43**, 1.

36. M. Cavaluzzo, Q. Chen, J. A. Zubieta, *Chem. Commun*., **131**,(1993).

37. E. K. Brechin, *Chem. Commun*, **2005**, 5141.

38. L. R. MacGillivray, J. L. Atwood, *Nature* 1997, 389, 469; O. Ugono, K. T. Holman, *Chem. Commun*. 2006, 2144; S. J. Dalgarno, S. A Tucker, D. B. Bassil, J. L. Atwood, *Science*, 2005, 309, 2037.

39. S. Petit, G. Pilet, D. Luneau, L. F. Chibotaru, L. Ungur, *Dalton Trans*., 2007, 40, 4582.

40. C. Aronica, G. Chastanet, E. Lueva, S. A. Borshch, J. M. Clemente-Juan, D. Luneau, *J. Am. Chem. Soc.,* 2008, **130**,2365.

41. C. Desroches, G. Pilet, P. A. Szilagyi, G. Molnar, S. A. Borshch, A. Bousseksou, S. Parola, D. Luneau*, Eur. J. Inorg. Chem*., 2006, 357.

42. C. Desroches, G. Pilet, S. A. Borshch, S. Parola, D. Luneau, *Inorg. Chem*., 44, 9112, 2005.

43. (a) T. Kajiwara, N. Iki, M. Yamashita, *Coord. Chem. Reviews*, 251, 2007, 1734.; (b) T. Kajiwara, N. Kon, S. Yokozawa, T. Ito, N. Iki, S. Miyano, *J. Am. Chem. Soc.,* 2002, **124**,11274.

44. P. W. Betteridge, J. R. Carruthers, R. I. Cooper, K. Prout, D. J. Watkin, *J. Appl. Crystallogr*., 2003, **36**, 1487.

Chapter 2: Calix[4]arene clusters as single-molecule magnets and magnetic coolers.

Introduction

The use of methylene-bridged calix[4]arenes in 3*d* and 3*d*/4*f* chemistry produces a series of very exciting clusters. In this chapter we present the first Mn cluster and the first ever single-molecule magnet to be isolated using any methylene bridged calix[*n*]arene - a ferromagnetically coupled mixed-valence $[Mn^{III}_2Mn^{II}_2]$ complex housed between either two TBC4s or two C4s, $[Mn^{III}_2Mn^{II}_2(OH)_2(TBC4)_2(DMF)_6]$ (**1**) and $[Mn^{III}_2Mn^{II}_2(OH)_2(C4)_2(DMF)_6]$ (**2**) . To date almost all SMMs have been made via the self-assembly of 3d metal ions in the presence of bridging/chelating organic ligands.[1] However, very recently an exciting new class of SMMs, based on 3d metal clusters (or single lanthanide ions) housed within polyoxometalates,[2] has appeared. These types of molecules, in which the SMM is completely encapsulated within (or shrouded by) a "protective" organic or inorganic sheath have much potential for design and manipulation: for example, for the removal of unwanted dipolar interactions, the introduction of redox activity, or to simply aid functionalisation for surface grafting.[3] The series is extended by a family of clusters of general formula $[Mn^{III}_4Ln^{III}_4(OH)_4(C4)_4(NO_3)_2(DMF)_6(H_2O)_6](OH)_2$ (where C4 is calix[4]arene; Ln = Gd (**3**), Tb (**4**), Dy (**5**)). The molecular structure describes a square of Ln^{III} ions housed within a square of Mn^{III} ions. Magnetic studies reveal that **3** has a large number of molecular spin states that are populated even at the lowest investigated temperatures, whilst the ferromagnetic limit $S = 22$ is being approached only at the highest applied fields. This, combined with the high magnetic isotropy, enables the complex to be an excellent magnetic refrigerant for low-temperature applications. Replacement of the isotropic Gd^{III} ions with the anisotropic Tb^{III} and Dy^{III} ions "switches" the magnetic properties of the cluster so that they (**4** and **5**) behave as low-temperature molecular magnets displaying slow relaxation of the magnetisation. The chapter concludes with the report and structural-magnetic studies of the first ever poly-nuclear Cu^{II} clusters to be isolated using any methylene bridged calix[4]arene as

a new supramolecular building block; enneanuclear Cu^{II} tri-capped trigonal prisms housed between TBC4s.

Results and Discussion

The reaction of $MnBr_2$ with TBC4 and NEt_3 in a solvent mixture of MeOH/DMF results in the formation of the complex $[Mn^{III}_2Mn^{II}_2(OH)_2(TBC4)_2(DMF)_6]$ (**1**) which crystallises as purple blocks that are in the monoclinic space group $P2_1/c$. The cluster (Figure 2.1) comprises a planar diamond or butterfly-like $[Mn^{III}_2Mn^{II}_2(OH)_2]$ core in which the wing tip Mn ions (Mn1) are in the 3+ oxidation state and the body Mn ions (Mn2) in the 2+ oxidation state. This is a common structural type in Mn SMM chemistry,[4] but the oxidation state distribution here is highly unusual, being "reversed" from the norm in which the body Mn ions are almost always 3+. Indeed the "reversed" core has been seen only once before, in the cluster $[Mn^{III}_2Mn^{II}_2(teaH)_2(acac)_4(MeOH)_2]^{2+}$ ($teaH_3$ = triethanolamine) and its analogues.[5] The Mn^{3+} ions are in distorted octahedral geometries with the Jahn-Teller axes defined by O5(DMF)-Mn1-O6(OH). The four equatorial sites are occupied by the oxygen atoms (O1-O4) of the TBC4, two of which bridge in a μ_2-fashion to the central Mn^{2+} ions (Mn1-O4-Mn2, 103.5°; Mn1-O1-Mn2, 105.4°). These are connected to each other (Mn2-O6-Mn2', 94.7°) and to the Mn^{3+} ions (Mn1-O6-Mn2, 100.4°; Mn1-O6-Mn2', 98.8°) via two μ_3-bridging OH^- ions, with the two remaining equatorial sites (completing the distorted octahedral geometry on Mn2) filled by terminal DMF molecules. There are no inter-molecular H-bonds between symmetry equivalents of **1** in the crystal structure with the closest interactions being between neighbouring DMF molecules at ca. 3.3 Å. The only inter-molecular interaction with the core of **1** is from a disordered methanol of crystallisation that hydrogen bonds to O4.

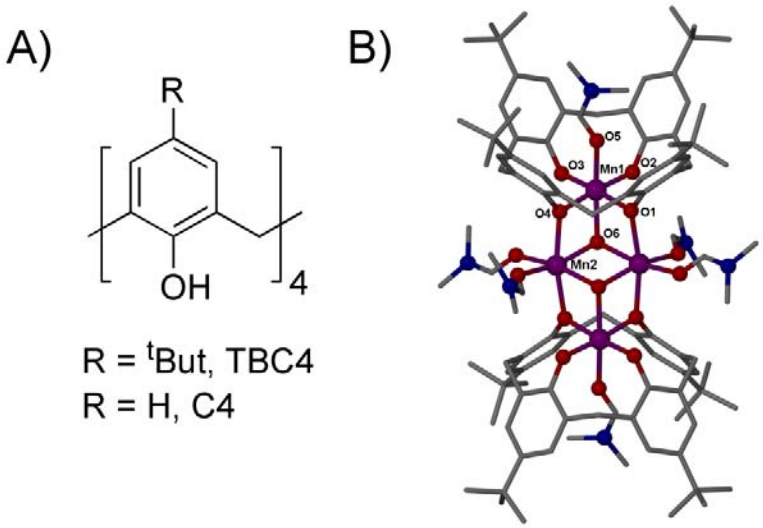

Figure 2.1. A) Structure of the calix[4]arenes used in SMM formation. B) Single crystal X-ray structure of **1**. Colour code: Mn = purple, O = red, N = blue, C = silver. Selected atoms are labeled and H-atoms have been omitted for clarity.

Notably, the orientation of the endo-TBC4 DMF molecule in **1** (Figure 2.2) is atypical and is driven by coordination. To our surprise we could not find a report on the solid state structure of the DMF solvate of TBC4. Solvothermal re-crystallisation of TBC4 from DMF resulted in the formation of large colourless crystals (Figure 2.3) that were suitable for X-ray diffraction studies. The crystals are in a tetragonal cell that is common for solvates of TBC4,[6] and structural analysis shows the expected bi-layer arrangement in which the DMF molecules are oriented with methyl groups inserted into the calixarene cavity as might be expected (Figure 2.4). For comparison, the extended structure of **1** (Figure 2.4) shows a bi-layer type arrangement that is skewed relative to the planar arrangement shown in Figure 2.4A. This is most likely attributable to the restriction of TBC4 orientation - that is dictated by cluster formation - in addition to the presence of the peripheral DMF ligands on Mn2 and its symmetry equivalent (Figure 2.1B). Furthermore, the almost completely encapsulated cavity bound DMF molecule in **1** should have little effect over bi-layer orientation relative to the DMF solvate of TBC4 considering that guest protrusion from the cavity is similar in both cases (see Figures 2.2 and 2.3 respectively).

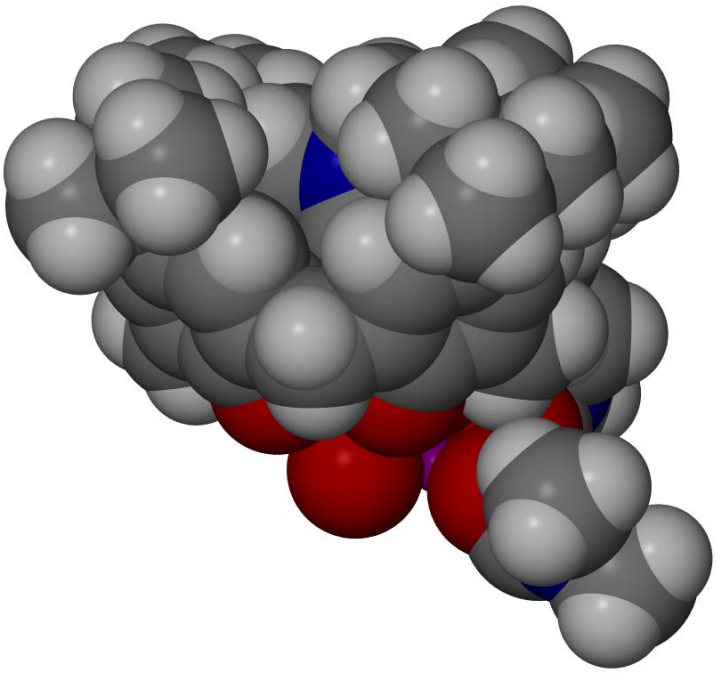

Figure 2.2. Space filling representation of the asymmetric unit in **1** showing the endo-cavity DMF molecule only slightly protruding from TBC4 cavity.

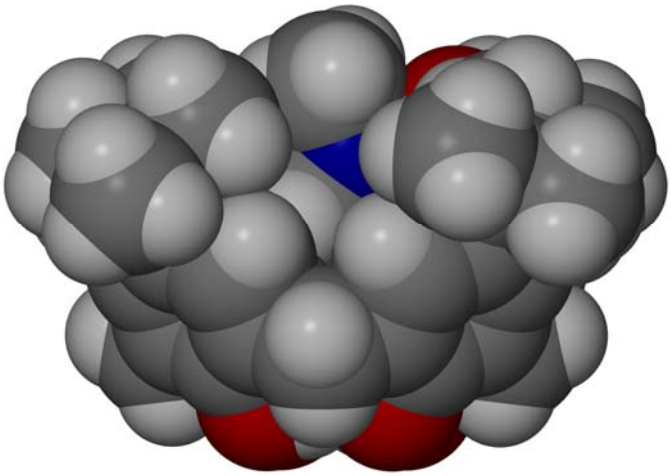

Figure 2.3. Space filling representation of the endo-cavity guest molecule in the DMF solvate of TBC4. Note the similar guest protrusion to that shown in Figure 2.2.

Although the extended structure in **1** does deviate from true planarity, the clusters are nevertheless arranged in bi-layers that have an inter-layer separation of ~ 19 Å (Figure 2.4B).

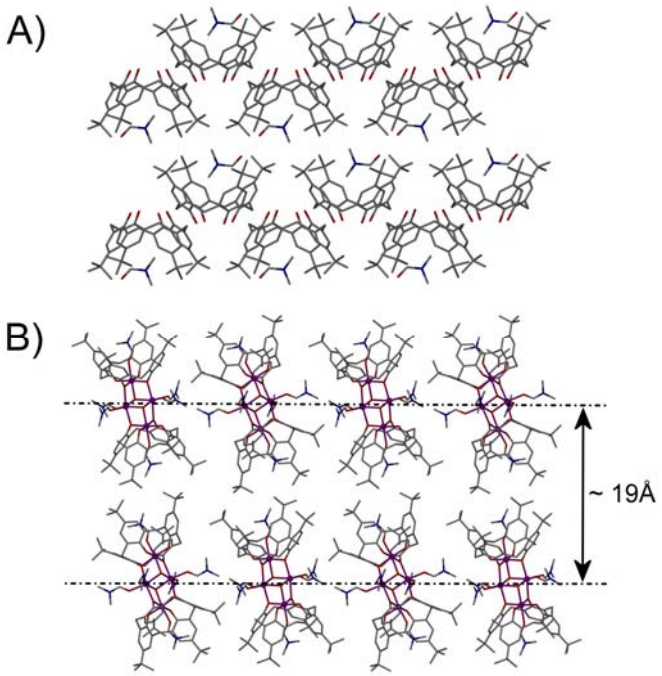

Figure 2.4 A) Extended structure of TBC4·DMF. B) The extended structure of **1** showing the inter-planar separation between layers of clusters. Figures not to scale and hydrogen atoms omitted for clarity.

Magnetic Studies

With respect to the magnetic properties of **1**, dc susceptibility measurements were carried out in the 300 - 5 K temperature range in an applied field of 0.1 T. The room temperature $\chi_M T$ value of 15.5 cm^3 K mol^{-1} is larger than the spin-only value expected for an uncoupled $[Mn^{III}_2Mn^{II}_2]$ unit of 14.75 cm^3 K mol^{-1} (Figure 2.5). The value then increases very slowly with decreasing temperature reaching a maximum of ~25 cm^3 K mol^{-1} at 5 K. The behaviour - similar to that reported for other $[Mn^{III}_2Mn^{II}_2]$ clusters - is suggestive of dominant but weak intra-molecular ferromagnetic exchange.[4] The experimental data can be satisfactorily fitted using the (standard)[4b] isotropic 2*J* model of Figure 2.5, affording the parameters J_{bb} = -2.43 cm^{-1} and J_{wb} = +1.84 cm^{-1} for g = 2.0 (fixed). With these parameters the spin ground state of the system is an S = 7 spin

state, with numerous excited states lying just above it, defining a quasi-continuum of states. Interestingly the magnitude of the exchange interactions closely resembles that observed for **2**, but in that case distortions of the Mn^{2+}-O-Mn^{2+} central core resulted in all the exchange interactions being very weakly antiferromagnetic.[5] We also note that the exchange interactions are likely much smaller than the single ion zero-field splitting (zfs, weak exchange limit) and thus the low lying multiplets cannot properly be described as total *S* states.

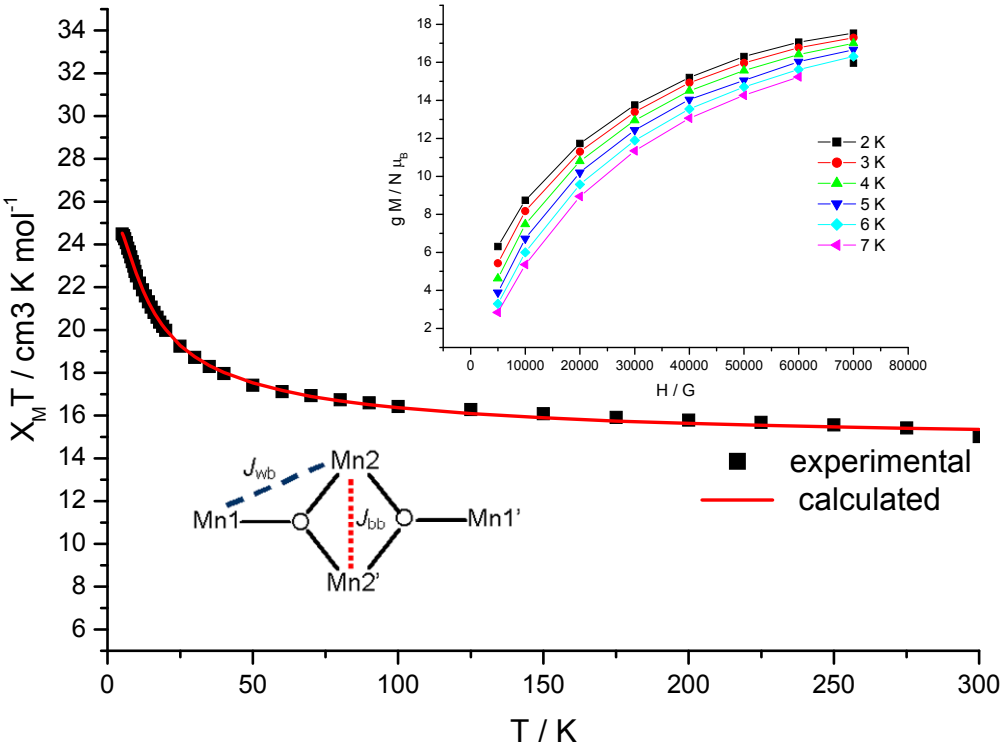

Figure 2.5. Plot of $\chi_M T$ versus *T* for **1**. The solid line is a fit of the experimental data using the cartoon scheme shown in the lower inset. Inset (top): Magnetisation ($M/N\mu_B$) vs *H* data in the 2-7 K and 0.5 - 7 T temperature and field ranges.

This picture is also reflected in the magnetisation versus field data (collected in the ranges 0.5 – 7.0 T and 2 – 7 K and plotted in the inset of Figure 2.5) which shows *M* increasing only slowly with *H*, rather than quickly reaching saturation as one would expect for an isolated spin ground state. This is indicative of the population of low lying levels with smaller magnetic moment, which only become depopulated with the application of a large field - and so we cannot describe the system within the giant

spin approximation. Ac susceptibility studies carried out on crystalline samples of **1** in the 1.8-10.0 K range in a 3.5 G field oscillating at frequencies up to 1000 Hz (Figure 2.6) display the tails of frequency-dependent out-of-phase (χ_M'') signals (suggestive of SMM behaviour) but no peaks.

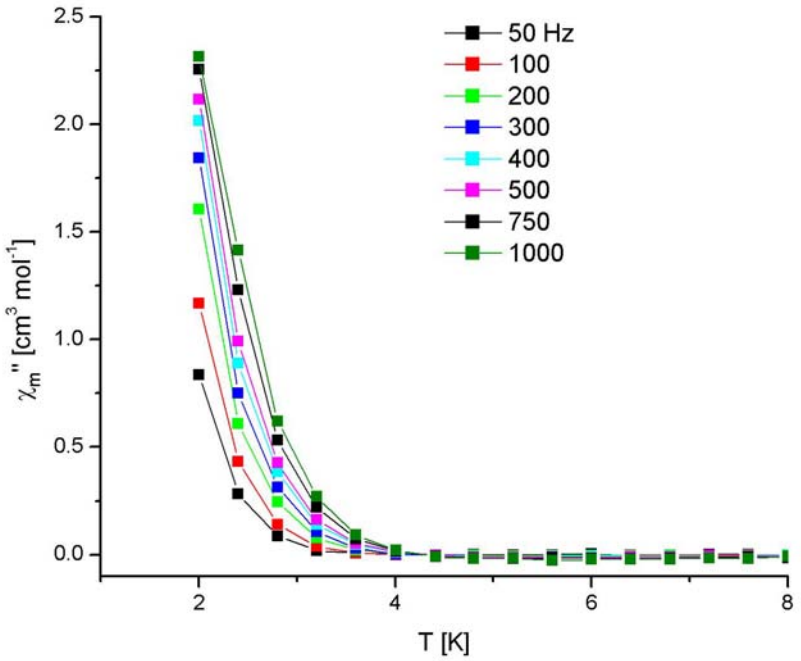

Figure 2.6. Plot of the out-of-phase (χ_M'') ac susceptibility versus T for complex **1** at the indicated frequencies and temperature range.

Hysteresis loop measurements carried out on single crystals using a micro-SQUID assembly with the field applied along the easy axis of magnetisation,[7] show temperature and sweep rate dependent hysteresis loops confirming SMM behaviour (Figure 2.7). The loops are indicative of a well-isolated SMM (*i.e.* no inter-cluster interactions) with quantum steps, but one in which many excited states are clearly mixed with the ground state, in agreement with the powder data above. In addition to the contribution of excited states, crystal defects, nuclear spins, dipolar interactions and/or disorder (if present) will also lead to the broadening of steps.

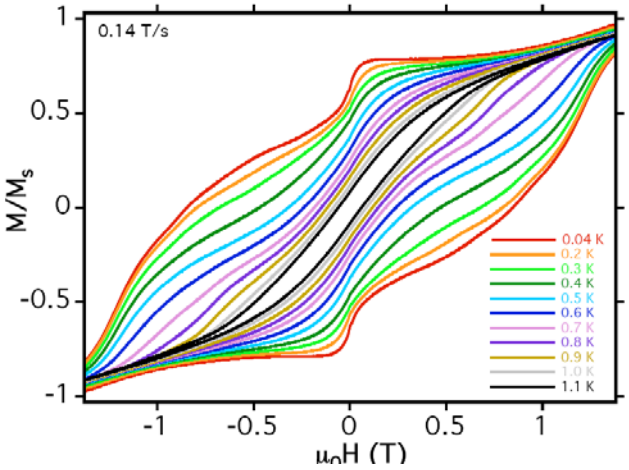

Figure 2.7. Hysteresis loops measured on single crystals of **1**, M is normalised to its saturation value.

To demonstrate generality of the calix[4]arene based SMM motif, the same synthetic route with C4 in place of TBC4 resulted in the formation of thin weakly diffracting purple crystals. X-ray diffraction studies showed the crystals to be of poor quality, but afforded a partial structure. Formation of the C4 based SMM (**2**) core that is analogous to **1** was confirmed in the partial structure by observation of the main atomic positions, as shown in Figure 2.8. Examination of the extended structure shows that **2**, relative to **1**, assembles as a bi-layer with a markedly shorter inter-layer spacing of ~ 13.5 Å (Figure 2.8B). This reduced inter-layer spacing is likely due to both removal of the ^{t}But groups from the upper rim, and the subsequent protrusion of the DMF methyl groups from the C4 cavity. As a result of cavity occupation, there appears to be no notable interactions between neighbouring C4s (Figure 2.9). This clearly shows that substitution at the calixarene upper rim has a dramatic effect on assembly within resulting bi-layers, and suggests that alteration of these groups may afford a degree of supramolecular control with this system.

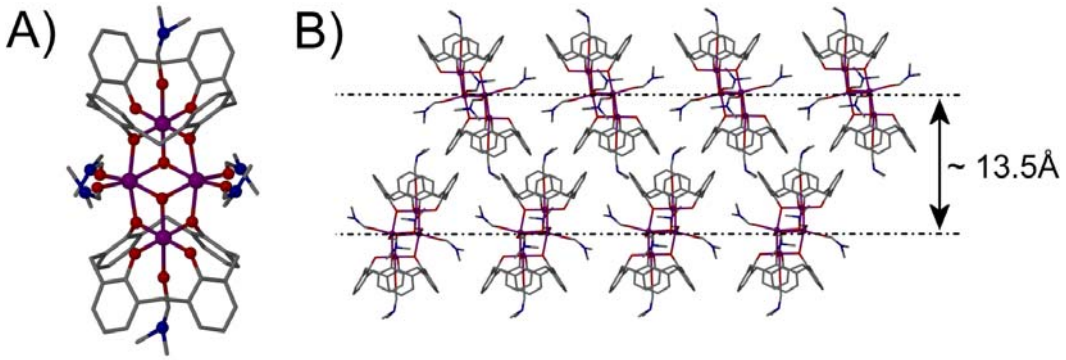

Figure 2.8. A) Partial single crystal X-ray structure of **2**. B) The extended partial structure of **3** showing the inter-planar separation between layers of SMMs. Figures not to scale and hydrogen atoms omitted for clarity.

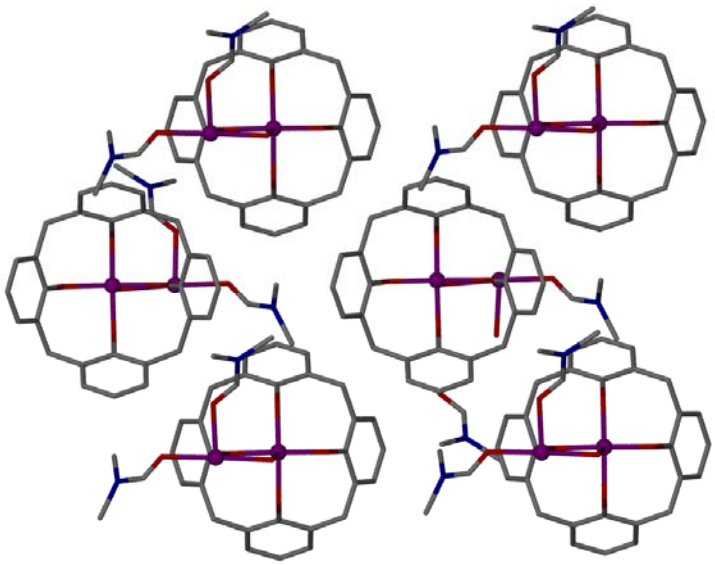

Figure 2.9. Cross section of part of the extended partial structure of **2** showing no notable interactions between neighbouring C4s.

To conclude, we have presented the first Mn cluster and the first SMM to be isolated using any methylene bridged calix[*n*]arene. This SMM formation is general for calix[4]arenes and given the vast range of methylene bridged derivatives available, this motif presents a virtually unbounded range of SMMs that possess huge scope for materials design. The calix[4]arenes provide a protective skin both above and below the SMM layer, and alteration to the upper rim properties of the calixarene framework will provide control over bi-layer packing, inter-layer spacing, and three dimensional

order in general. Alteration of the guest in the calixarene cavity, and also the ligands at the peripheral Mn coordination sites will provide further opportunities for controlling self-assembly and tuning of the magnetic properties of these new SMMs. This will be the focus of future studies, as will be obtaining a more accurate structure of **2** and examining its magnetic properties. In addition to this, subsequent/additional guest exchange or intercalation within layers of the crystal lattice holds further potential to alter the properties of these new interesting materials.

After the synthesis and characterization of SMMs with methylene bridged TBC4, we extended our study to the syntheses, structures and magnetic properties of a family of $[Mn^{III}_4Ln^{III}_4]$ clusters, the first methylene bridged calix[*n*]arene based 3*d*-4*f* molecules, in which the replacement of one Ln(III) ion for another invokes dramatic changes in the observed magnetic properties in otherwise structurally analogous molecules.

The reaction of $Mn(NO_3)_2{\cdot}4H_2O$ and $Ln(NO_3)_3{\cdot}6H_2O$ with C4 and NEt_3 in a solvent cocktail of MeOH/DMF results in the formation of complexes with the general formula $[Mn^{III}_4Ln^{III}_4(OH)_4(C4)_4(NO_3)_2(DMF)_6(H_2O)_6](OH)_2$, where Ln = Gd (**3**), Tb(**4**), or Dy (**5**). Crystals of **3** are in the monoclinic space group *C*2/*c*, whilst those of **4** and **5** are found to crystallise in the triclinic space group *P*-1. The C4 supported clusters in all three complexes are structurally analogous, differing only in the number of co-crystallised solvent molecules (which are badly disordered), and so for the sake of brevity discussion will be limited to complex **3**, highlighting any specific differences between the molecules at appropriate stages. The cluster (Figure 2.10) comprises a near-planar octametallic core describing a "square" of Mn(III) ions encasing a "square" of Gd(III) ions. The $\{Mn_4\}$ square has dimensions 6.591 × 7.042 Å and the $\{Gd_4\}$ square 3.915 × 3.929 Å, with the latter rotated approximately 45° with respect to the former. This is a very unusual motif, but has also been observed recently in the cluster $[Mn_4Nd_4(OH)_4(fcdc)_2(Piv)_8(bdea)_4]{\cdot}H_2O$ (fcdc = ferrocene dicarboxylate; piv = pivalate or trimethyacetate; $bdeaH_2$ = *N*-butyldiethanolamine).[8] The central $[Gd^{III}_4(OH)_4(NO_3)_2]$ unit comprises the four Gd(III) ions connected to each other via four μ_3-OH^- ions (O12 and O16 and symmetry equivalents) and two η^2, η^2, μ_3-NO_3^- ions. The OH^- ions also bridge to the four $[Mn^{III}(C4)(DMF)]$ corner units of the $\{Mn_4\}$ square. The μ_3-TBC4 ligands are fully deprotonated with two oxygen atoms (O1, O4 and O7, O8 and symmetry equivalents) bonding terminally to the

Mn(III) ions and two (O2, O3 and O6, O9 and symmetry equivalents) μ-bridging to the central $\{Gd_4\}$ square. The Mn ions lie in distorted octahedral geometries in $\{O_6\}$ coordination spheres with the Jahn-Teller axes (O10-Mn2, 2,225 Å, Mn2-O16, 2.218 Å; O5-Mn4, 2.261 Å, Mn4-O12, 2.221 Å) described by the DMF-Mn-OH vectors; *i.e.* across the diagonal of the $\{Mn_4\}$ square. The Gd(III) ions are eight coordinate and are in distorted square antiprismatic geometries with their remaining coordination sites filled by a combination of terminal H_2O molecules, which form intra-molecular H-bonds to the terminally bonded O-atoms of the C4 ligands (e.g. O8…O11, 2.642 Å) and inter-molecular H-bonds to hydroxide anions, and DMF molecules.

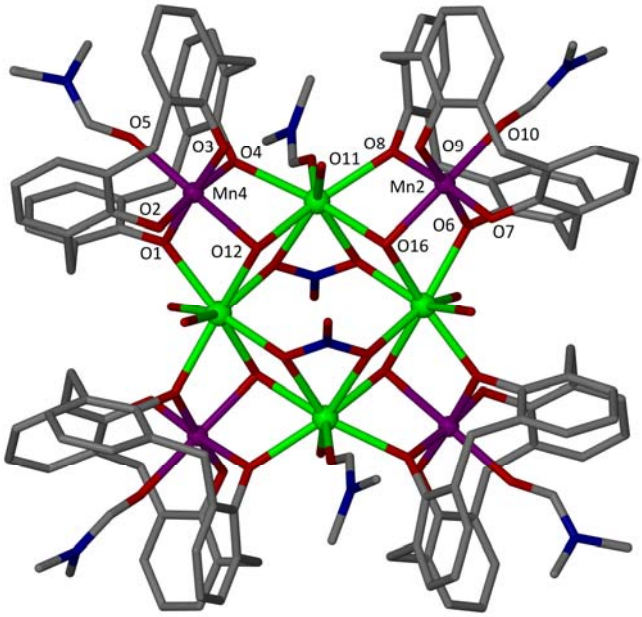

Figure 2.10. Molecular structure of **3** showing the coordination environments around the Mn^{III} and Gd^{III} centres. Hydrogen atoms, hydroxide anions and co-crystallized DMF molecules omitted for clarity. Colour code Mn = purple; O = red; N = dark blue; C = grey; Ln = green.

Examination of the extended structures of **3** – **5** shows that symmetry equivalent clusters pack together to form two types of complex arrangement. Disorder is present in the solvent molecules co-crystallised with the clusters in each of the crystal lattices, and this is severe enough to preclude detailed analysis of the inter-molecular interactions between all of the structural components in each crystal structure. The structure of **3** differs to those of **4** and **5** (isostructural), and packing of the asymmetric unit shows that four [Mn(III)-C4] sub-units assemble in a pseudo-capsule assembly to

produce a DMF rich microenvironment between the corner units of nearest-neighbour clusters (Figure 2.11A). These are reminiscent of hexameric calixarene based molecular capsules, and suggest that appropriately functionalized C4 molecules could be employed in cluster formation to invoke templated self-assembly into nanometer scale assemblies containing large internal volumes.[9a,c,e] The extended structures of isostructural **4** and **5** (Figure 2.11B) show the formation of a similar type of pseudo-capsule assembly. Three [Mn(III)-C4] sub-units assemble to produce a second type of DMF microenvironment, while the fourth neighbouring sub-unit points away from the centre of the capsule-like assembly. Notably, the [Mn(III)-C4] sub-unit found in the $[Mn^{III}_2Mn^{II}_2]$ SMM shown in Figure 2.1 is preserved in these new hybrid 3*d*-4*f* complexes. This indicates that this is indeed a favourable structural sub-unit (or "metalloligand") for Mn(III), and that these moieties may well be exploited in the formation of other complexes and supramolecular architectures, whose self-assembly may be governed by relatively small changes in reaction conditions.

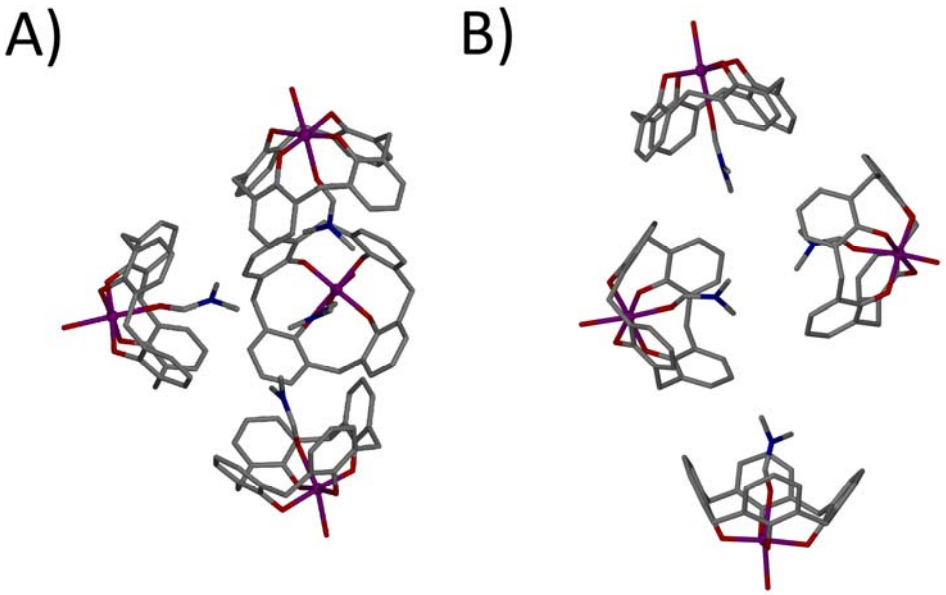

Figure 2.11. Partial extended structures of **3**(A) and **4** (and isostructural **5**, B) showing the packing of [Mn(III)-C4] sub-units in each case. A) Four corner units of nearest-neighbour clusters form a pseudo-capsule assembly containing a DMF microenvironment that is reminiscent of other calixarene based molecular capsules.[9a,c,e] B) Three corner units of nearest-neighbour clusters form a related assembly, albeit with one pointing away from the DMF microenvironment relative to that shown in A. Figures not to scale.

Magnetic Studies

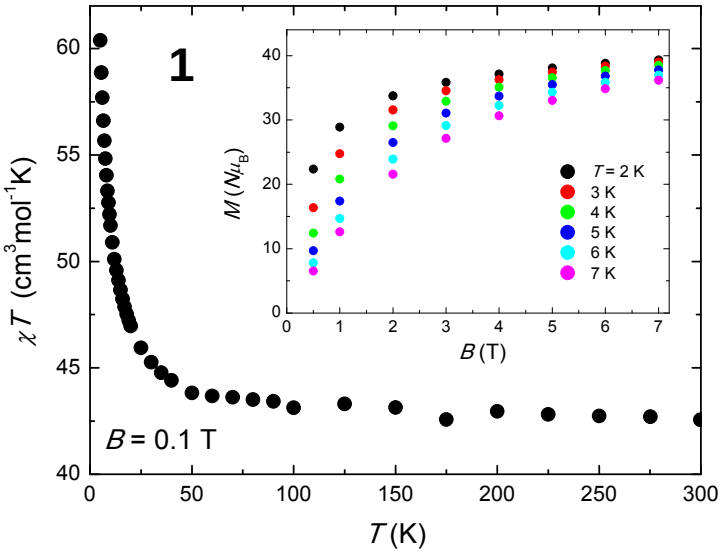

Figure 2.12. Temperature dependence (5 – 300 K) of the dc-susceptibility for **3** collected in an applied field of 0.1 T. Inset: magnetisation of **3** versus applied field for several temperatures.

We investigated the magnetic properties of **3** by dc-susceptibility experiments in the 300 -5 K temperature range in an applied field B of 0.1 T (Figure 2.12). The room-temperature χT value of ~42.8 cm^3 K mol^{-1} is close to the spin-only (g = 2.0) value expected for an uncoupled [$Mn^{III}_4Gd^{III}_4$] unit of ~43.5 cm^3 K mol^{-1}. The value stays essentially constant as the temperature is decreased until approximately 50 K, below which it increases, reaching a maximum of ~60.5 cm^3 K mol^{-1} at 5 K. This behaviour is suggestive of very weak intra-molecular exchange and one would expect a nesting, and thus population of, several S states even at the lowest temperatures studied. This is reflected in the low temperature χT value, which is well below that expected for a ferromagnetically coupled cluster with an isolated S = 22 ground state (253 cm^3 K mol^{-1}), and can also be seen in the magnetisation versus field data (collected in the 2 – 7 K temperature range for applied fields up to 7 T, and plotted in the inset of Figure 2.12) which shows M increasing only slowly with B, rather than quickly reaching saturation as one would expect for an isolated spin ground state. This is indicative of

the population of low lying levels with smaller magnetic moment, which only become depopulated with the application of a large field. This result suggests **1** to be an excellent candidate for magnetic refrigeration.[10b] To validate this statement, our preliminary studies focused on the determination of the magnetic entropy change ΔS_m of **1** by analysing the experimental $M(B)$ data of Figure 2.12. In an isothermal process of magnetisation, ΔS_m can be derived from the Maxwell relations by integrating over the magnetic field change $\Delta B = B_f - B_i$, i.e., $\Delta S_m(T)_{\Delta B} = \int[\partial M(T,B)/\partial T]_B dB$.[11,12,13] The so-obtained ΔS_m is depicted in Figure 2.13 for several field changes. It can be seen that $-\Delta S_m$ increases gradually with increasing ΔB reaching a value of 19.0 J kg^{-1} K^{-1} at T = 4 K, achieved for the experimentally accessible maximum ΔB of 7 T. This is amongst the highest values ever reported for this temperature range.[13] We also note that the observed magnetic entropy changes are much larger than the maximum allowable entropy for an isolated S = 22 spin ground state, i.e. $R \ln(2S + 1) = 3.8\ R$ = 9.0 J kg^{-1} K^{-1}. This demonstrates that the presence of low-lying excited spin states can have a strong and positive influence on the magneto-caloric effect.[13]

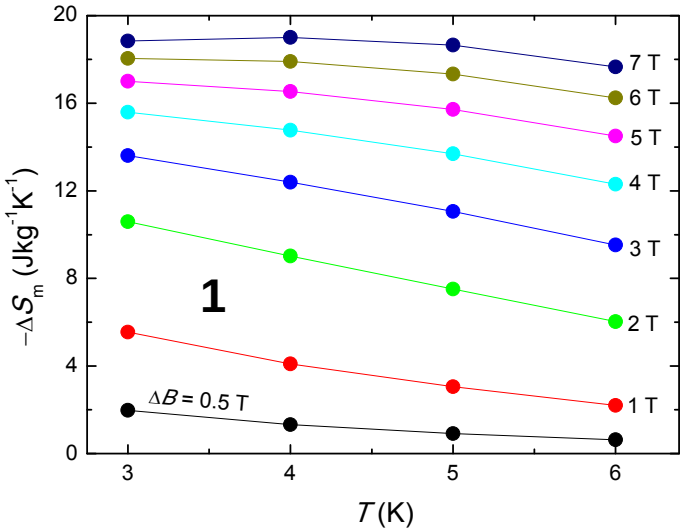

Figure 2.13. Temperature dependencies of the magnetic entropy change of **1** for applied field changes ΔB.

We next turn to the study of the magneto-caloric effect of **3** by means of heat capacity (*C*) experiments, emphasizing that the measurement of the heat capacity as a function of temperature in constant magnetic field provides the most complete characterisation of the MCE in magnetic materials.[12,13] The top panel of Figure 2.14 depicts the experimental heat capacity curves of **3** in the 30 – 0.3 K temperature range for several applied fields. It can be seen that the curves collected at temperatures below 1 K are strongly dependent on the applied field, and that they span over three orders of magnitude in units of *R* for the investigated field changes. The zero-field curve achieves a maximum of ~4 *R* for *T* = 0.8 K, whilst the field-independent lattice contribution has a value of 6 x10^{-3} *R* for the same temperature. The relevant feature is the broad specific heat anomaly that shifts towards higher temperatures on increasing applied field; we attribute this to the field-splitting of the spin multiplets of the molecule. We stress, however, that this behaviour cannot be reproduced by a simple model based on a well-defined *S* = 22 spin ground state (which would not exceed ~1 *R*). To explain the excess of experimental heat capacity, we need to invoke the contribution arising from the population of low-lying excited spin states, corroborating the previous magnetisation experiments. In the high-temperature range a large field-independent contribution appears that can be attributed to the lattice phonon modes of the crystal. The dashed line in the top panel of Figure 2.14 represents a fit to this contribution with the well-known low-temperature Debye function, yielding a value of Θ_D = 23 K for the Debye temperature, typical for this class of cluster complex.[11b]

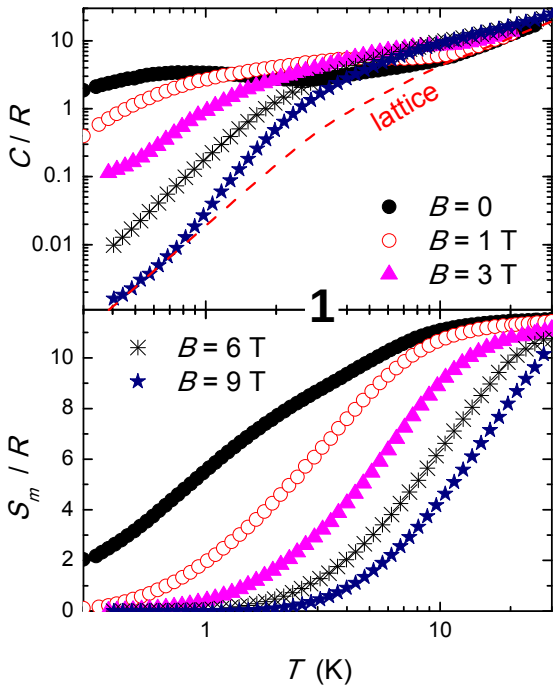

Figure 2.14. Top: temperature dependencies of the heat capacity of **3** normalised to the gas constant R collected for B = 0, 1, 3, 6 and 9 T. Dashed line is the fitted lattice contribution. Bottom: temperature dependencies of the experimental magnetic entropy for several B, as obtained from the respective magnetic contributions to the total heat capacity.

From the experimental heat capacity, the temperature dependence of the magnetic entropy S_m is obtained by integration, i.e., using $S_m(T,B) = \int C_m/T \, dT$, where the magnetic heat capacity C_m is obtained from C upon subtracting the lattice contribution. The so-obtained S_m is shown in the bottom panel of Figure 2.14 for the corresponding applied fields. As further evidence of the participation of excited spin states, we note that the experimental $S_m(T)$ by far exceeds the value expected for an isolated $S = 22$ ground state, i.e. 3.8 R.

It now becomes straightforward to obtain the magnetic entropy changes ΔS_m of **3**, whose temperature-dependencies are depicted in the top panel of Figure 2.15 for several field changes. Any uncertainty in the determination of the field-independent lattice contribution is irrelevant for this calculation and cancels out since we are dealing with differences between entropies. The $\Delta S_m(T,\Delta B)$ curves are consistent with the preliminary estimates obtained in Figure 2.13, proving the validity of employing both the magnetization and heat capacity data in the analysis. Furthermore, we

observe that $-\Delta S_m$ reaches the extremely large value of 21.3 J kg^{-1} K^{-1} at liquid-helium temperature for the investigated field change ΔB = (9 – 0) T.

The analysis of the heat capacity data also permits us to estimate the adiabatic temperature change ΔT_{ad} by using $\Delta T_{ad}(T)_{\Delta B} = [T(S_m)_{Bf} - T(S_m)_{Bi}]S_m$ directly from the experimental magnetic entropy S_m depicted in Figure 2.14 (bottom panel). The bottom panel of Figure 2.15 shows that the maximum in ΔT_{ad} gradually decreases and shifts to lower temperatures by decreasing the field change ΔB. Indeed, it changes from ΔT_{ad} = 9.0 K for ΔB = (9 – 0) T at T = 4.4 K to ΔT_{ad} = 2.0 K for ΔB = (1 – 0) T at T = 2.0 K. In other words the magnetic field dependence of the adiabatic temperature change increases from 1 to 2 K/T, respectively, making **3** one of the finest refrigerants in the liquid-helium temperature range.[12,10b]

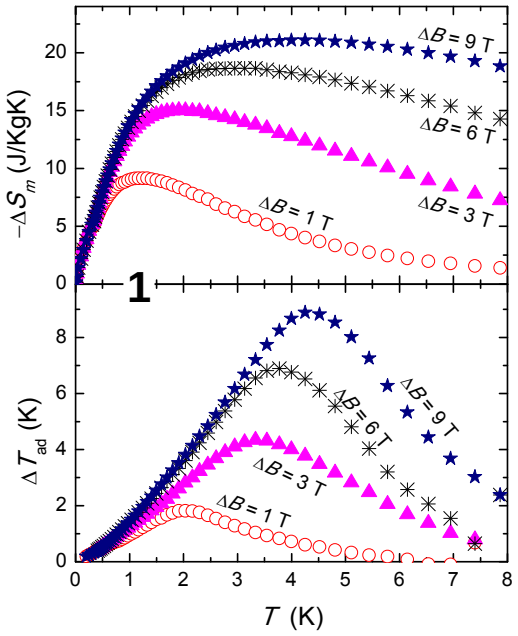

Figure 2.15. Top: temperature dependencies of the magnetic entropy change of **3** for the indicated applied-field changes ΔB. Bottom: temperature dependencies of the adiabatic temperature change of **3** for the indicated ΔB. Both $\Delta S_m(T,\Delta B)$ and $\Delta T_{ad}(T,\Delta B)$ curves are obtained from the heat capacity data of Figure 2.14.

We have pointed that negligible anisotropy is a major requirement for achieving an enhanced magneto-caloric effect with polymetallic molecules. As is well established, a large magnetic anisotropy promotes single-molecule magnet (SMM) behaviour, for which slow relaxation of the net spin per molecule is obtained below a super-paramagnetic blocking temperature. The consequence is that the blocked molecular spins tend to lose thermal contact with the lattice at low temperatures,[14] resulting in a

lower magnetic entropy and therefore a lower MCE. The effect of the anisotropy on the efficiency of a polymetallic molecule in terms of magnetic refrigeration has already been demonstrated by means of simple numerical simulations, and experimentally using a large variety of molecules from the prototype Mn_{12} SMM to the [ideally] isotropic Mn_{10} supertetrahedron.[13] However, to the best of our knowledge, no example has yet been provided of a molecular refrigerant in which the degree of anisotropy can be experimentally and exclusively altered/tuned without structural alteration. The $[Mn^{III}_4Ln^{III}_4]$ molecular cluster can provide such a playground since the identity of the Ln(III) can be easily changed. By replacing the zero-orbital moment Gd^{III} ion (**3**) with the anisotropic Tb^{III} (**4**) or Dy^{III} (**5**) ion, one can expect to observe abrupt changes in the magneto-thermal properties of these otherwise structurally analogous molecules.

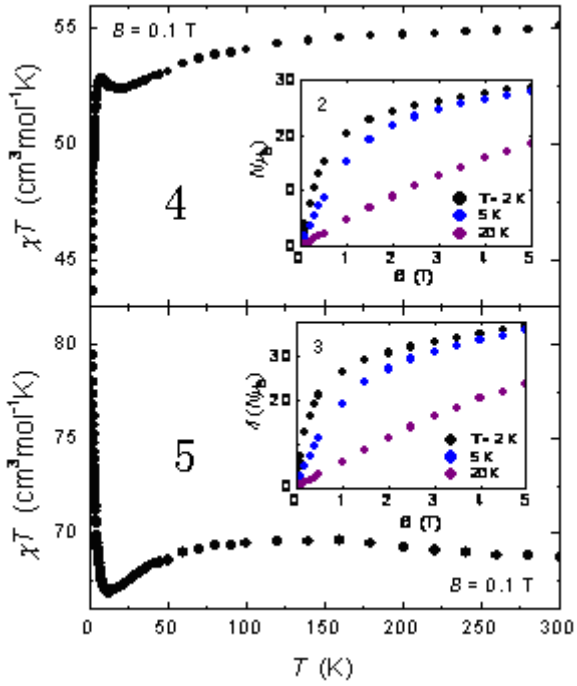

Figure 2.16. Temperature dependence (5 – 300 K) of the dc-susceptibility for **4** (top) and **5** (bottom) collected in an applied field of 0.1 T. Insets: magnetisation of **4** (top) and **5**(bottom) versus applied field for T = 2, 5 and 20 K.

Figure 2.16 depicts the dc-susceptibility measurements for **4** and **5**, collected in the 300 – 2 K temperature range for an applied field B of 0.1 T. Let us first examine complex **4**; terbium(III) is a non-Kramers ion with a $^7F_6$ ground state. The fit of the experimental $\chi(T)$ data to the Curie-Weiss law in the 300 – 5 K temperature range provides a small θ = –0.16 K, suggesting that the metallic ions are only weakly

magnetically correlated. The room-temperature χT value of **4** is ~55.5 cm^3 K mol^{-1} in reasonable agreement with the spin-only (g = 2.0) value expected for an uncoupled [$Mn^{III}_4Tb^{III}_4$] unit of ~59.3 cm^3 K mol^{-1}. The value stays essentially constant as the temperature is decreased until approximately 150 K, below which it decreases smoothly down to 22 K reaching a value of ~52.3 cm^3 K mol^{-1}. The 22 – 7 K temperature range is marked by an upward shift in the χT value that, considering the relatively large inter-cluster spacing, we associate to ferro- or ferrimagnetic intra-molecular exchange. In the lowest temperature range, χT sharply decreases to ~43.5 cm^3 K mol^{-1} at 2 K, suggesting either antiferromagnetism or perhaps more likely the progressive depopulation of excited states of the lanthanide ions. A similar conclusion may be drawn by looking at the field dependence of the magnetisation (inset of Figure 2.16, top panel). On increasing field, the onset of a net molecular moment promotes a relatively quick increase of the magnetisation reaching 20.5 $N\mu_B$ at B = 1 T for T = 2 K, after which it increases linearly without saturating. Likewise for **3**, we expect the crystal field to split the $^6H_{15/2}$ ground state of dysprosium(III). Contrary to **4**, the fit of the experimental $\chi(T)$ data to a Curie-Weiss law in the 300 – 5 K temperature range provides a very small, but positive value [θ = +0.35 K] suggesting that the ferro- or ferrimagnetic component is relatively stronger in **5**. The $\chi T(T)$ value stays essentially constant from room temperature down to nearly 100 K, below which it experiences a small decrease to ~66.8 cm^3 K mol^{-1} at T = 12.6 K. The lowest temperature range is then characterised by an abrupt increase in χT, which reaches ~79.5 cm^3 K mol^{-1} at T = 2 K, corroborating the presence of a stronger ferro- or ferrimagnetic interaction than observed in **4**. This is also supported by the larger experimental values of the magnetisation, whose field dependence [qualitatively] is very similar to that of **4** (inset of Figure 2.16, bottom panel).

Because of the anisotropy induced by the Tb^{III} and Dy^{III} ions, and the observation that each molecular unit develops a net magnetic moment at low temperatures, it is reasonable to expect super-paramagnetic behaviour. We therefore investigated the dynamic properties of **4** and **5** by means of ac-susceptibility experiments. Both complexes show out-of-phase signals (χ'') at temperatures above 2 K (Figure 2.17), indicative of either a phase transition or slow relaxation of the magnetisation.

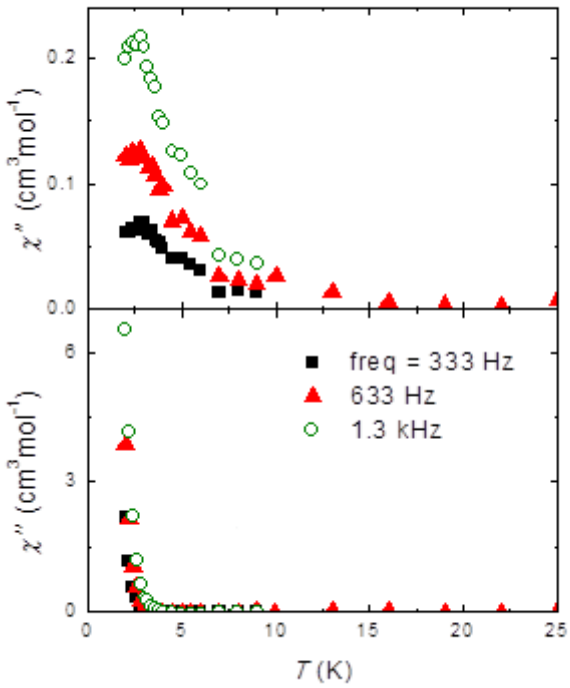

Figure 2.17. Temperature dependence of the out-of-phase ac-susceptibility for **4** (top) and **5** (bottom), collected in zero-applied field and for the excitation frequencies 333, 633 and 1300 Hz, as labeled.

In order to discriminate between these two phenomena, we extended our experiments to the lower temperature region, obtaining the results depicted in Figure 2.18.

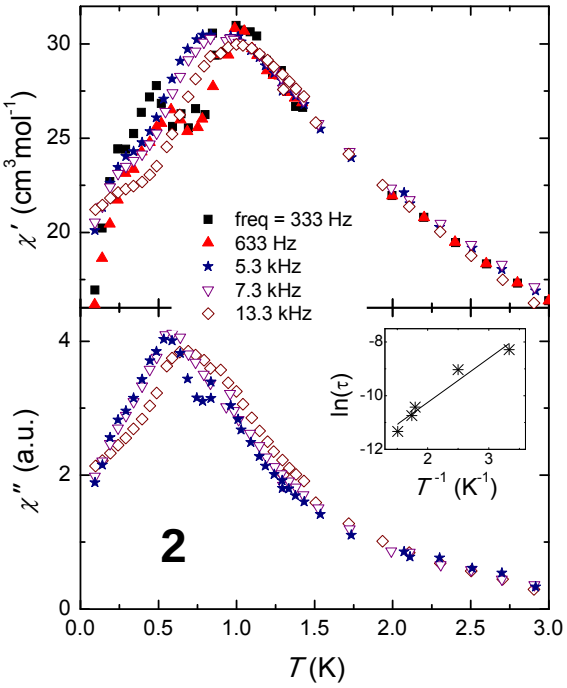

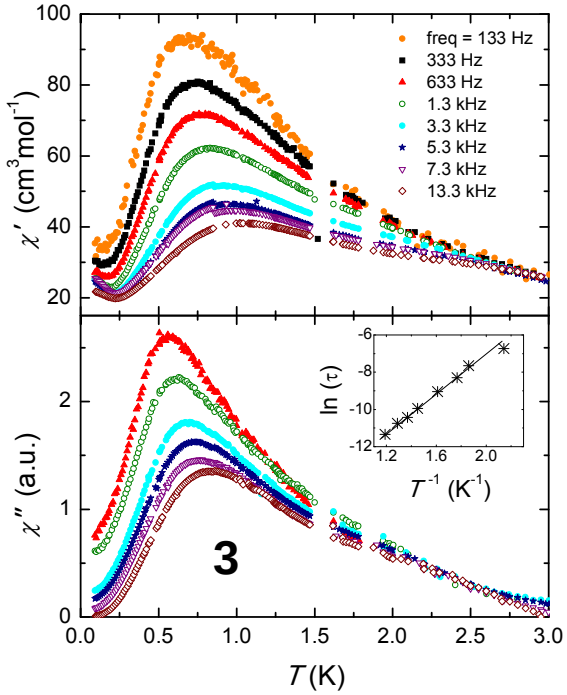

Figure 2.18. Temperature dependence of the in-phase (χ', top) and out-of-phase (χ'', bottom) ac-susceptibility for **4** (left) and **5** (right), collected in zero-applied field and for the indicated excitation frequencies. Insets: semi-logarithmic plots of the (main) zero-field relaxation time. The straight lines are fits to the Arrhenius law.

The main feature is a cusp in the in-phase component χ' of the ac-susceptibility which occurs at approximately 0.9 K for both complexes, accompanied by a non-zero out-of-phase component (Figure 2.18), with both maxima in χ' and χ'' being frequency (f) dependent. The experimental data suggest super-paramagnetic blocking of the molecular spins below T_B corresponding to the temperature at maximum absorption. Using the average value T_B = 0.9 K, the frequency shift of T_B, nominally $\Delta T_B/(T_B \Delta \log f)$, where ΔT_B is the change in T_B for the given change in frequency $\Delta \log f$, provides the values of 0.5 and 0.2 for **4** and **5**, respectively, which are comparable to that of other super-paramagnets.[15] The relaxation time for superparamagnets with an anisotropy barrier U is usually described with the Arrhenius law, typical of a thermal activation process: $\tau = \tau_0 \exp(U/k_B T)$, where $\tau = 1/2\pi f$ and τ_0 is an attempt frequency. We have fitted the cusp in the out-of-phase susceptibility with the above equation. The results are presented in Figure 2.18 (insets), affording $\tau_0 = 1\times10^{-7}$ s and U/k_B = 3.0 K for **4**, and $\tau_0 = 3\times10^{-8}$ s and U/k_B = 5.0 K for **3**. Closer inspection of the low-temperature ac-susceptibility (Figure 2.18) reveals that the magnetic relaxation in these materials is particularly complex, since other (secondary) relaxation pathways can be spotted besides the main one taking place at 0.9 K. Indeed, for both complexes, a rather broad frequency-dependent "shoulder" is observed in the 2 – 3 K temperature range. For **4**, a secondary cusp is observed in $\chi''(T)$ at somewhat higher temperature than that of the main feature. For **5**, the maximum absorption of a faster relaxation mechanism takes place below 80 mK, temperatures not experimentally accessible with our setup. The frequency dependence of the ac-susceptibility below 3 K suggests that both **4** and **5** are single-molecule magnets. Therefore, it is not a surprise that heat capacity experiments performed on **4** and **5** (Figure 2.19) can detect no sign of long-range magnetic order (in the form of a sharp lambda-like anomaly), a result also expected on the basis of structure considerations (see above). The complicated magnetic behaviour of these materials is also observed in Figure 2.19. For example the zero-field C curve of complex **4** shows a broad anomaly close to T = 3 K, followed by a second one at 1 K, and a third detected at the lowest investigated temperature, the latter being clearly visible in the case of in-field measurements.

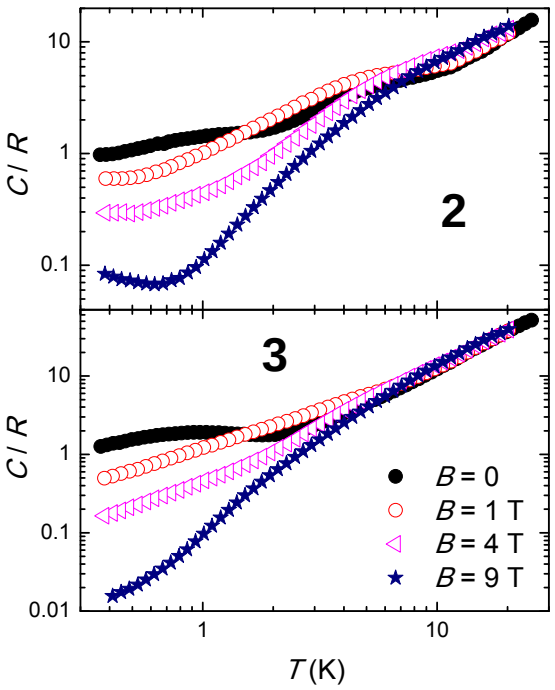

Figure 2.19. Temperature dependence of the heat capacity normalised to the gas constant *R* for **4** (top) and **5** (bottom) collected for *B* = 0, 1, 4 and 9 T, as labeled.

The measurements of the heat capacity of **3** and **4** indicate that these molecules would not be suitable for use as molecular refrigerants. This is simply understood by looking at the field-dependent curves and their absolute values in units of *R*. By comparing the results of Figure 2.19 with that obtained with an excellent refrigerant such as **3** (Figure 2.14), it can be seen that the zero-field heat capacities of **4** and **5** are notably smaller than that of **3** in the (magnetic dependent) low-temperature region. Furthermore, the change of applied field from 0 to 9 T causes the heat capacities of **4** and **5** to change by one-to-two orders of magnitude at best, i.e. more than an order of magnitude less than in **3**. Likewise, the changes in the magnetic entropy follow the same trend, allowing us to conclude that the anisotropy of the lanthanide ion is of crucial importance for dictating the performance of this family of molecules as magnetic refrigerants.

To conclude, we have expanded our initial studies into $[Mn^{III}_4Ln^{III}_4]$ cluster formation with calixarenes as supporting ligands so that we tailor these 3*d*/4*f* clusters of general formula $[Mn^{III}_4Ln^{III}_4(OH)_4(C4)_4(NO_3)_2(DMF)_6(H_2O)_6](OH)_2$ to include either Gd, Tb or Dy as desired. Magnetic studies show that the $[Mn^{III}_4Gd^{III}_4]$ cluster is an excellent

magnetic refrigerant for low-temperature applications. The molecular anisotropy added by replacing Gd with Tb or Dy results in (a) superparamagnetic behaviour of the $[Mn^{III}_4Tb^{III}_4]$ and $[Mn^{III}_4Dy^{III}_4]$ clusters with blocking temperatures in the temperature region below 1 K, and (b) poor performance of these clusters in terms of magnetic refrigeration. The [Mn(III)-C4] sub-unit is common to $[Mn^{III}_2Mn^{II}_2]$ SMMs and the $[Mn^{III}_4Ln^{III}_4]$ clusters reported here, and we are currently exploring the use of this moiety in the formation of alternative cluster assemblies through variation in reaction conditions. The substitution of other lanthanides in the $[Mn^{III}_4Ln^{III}_4]$ cluster motif is underway with a view to fully characterising the magnetic properties of the entire series of analogous clusters.

In the final part of this Chapter we present our initial forays into the coordination chemistry of Cu(II) and discuss the syntheses and structures of the first poly-nuclear Cu^{II} clusters to be isolated using any methylene bridged calix[*n*]arene - enneanuclear Cu^{II} tri-capped trigonal prisms housed between three TBC4s. These assemblies are pseudo-trigonal planar in nature, and show versatility in solid state packing akin to that of the TBC4 solvates.

Reaction of $CuCl_2{\cdot}2H_2O$, TBC4, NEt_3 and NH_4ClO_4 in a solvent mixture of EtOH/DMSO for three hours produces $[Cu^{II}_9(OH)_3(TBC4)_3Cl_2(DMSO)_6](Cu^{I}Cl_2){\cdot}DMSO$ (**6**·DMSO) which crystallises as dark green blocks that are in the monoclinic space group *C*2/*c* (Fig. 2.20B). The identical reaction with $Cu(NO_3)_2{\cdot}3H_2O$ produces the analogous complex $[Cu^{II}_9(OH)_3(TBC4)_3(NO_3)_2(DMSO)_6](NO_3){\cdot}$ DMSO (**7**·DMSO) which crystallises as dark green blocks that are in the tricilinc space group $P\bar{1}$. Structural analysis of **6** shows the metallic core [which is common to both] to describe a tri-capped trigonal prism of Cu^{II} ions; where Cu1, Cu3, Cu5 and symmetry equivalents Cu1*, Cu3* and Cu5* form the trigonal prism, with Cu2, Cu4 and Cu4* centres capping the square faces (Fig. 2.20B – 2.20D). The "upper" and "lower" triangular faces are each capped by a ["μ_3"]Cl^- ligand (Cl1 and Cl1*) that shows long contacts with Cu1, Cu3 and Cu5 of 2.818, 2.897 and 2.828 Å respectively. These anions reside within hydrophobic pockets generated by ligated solvent molecules on Cu1, Cu3 and Cu5 (and symmetry equivalents).

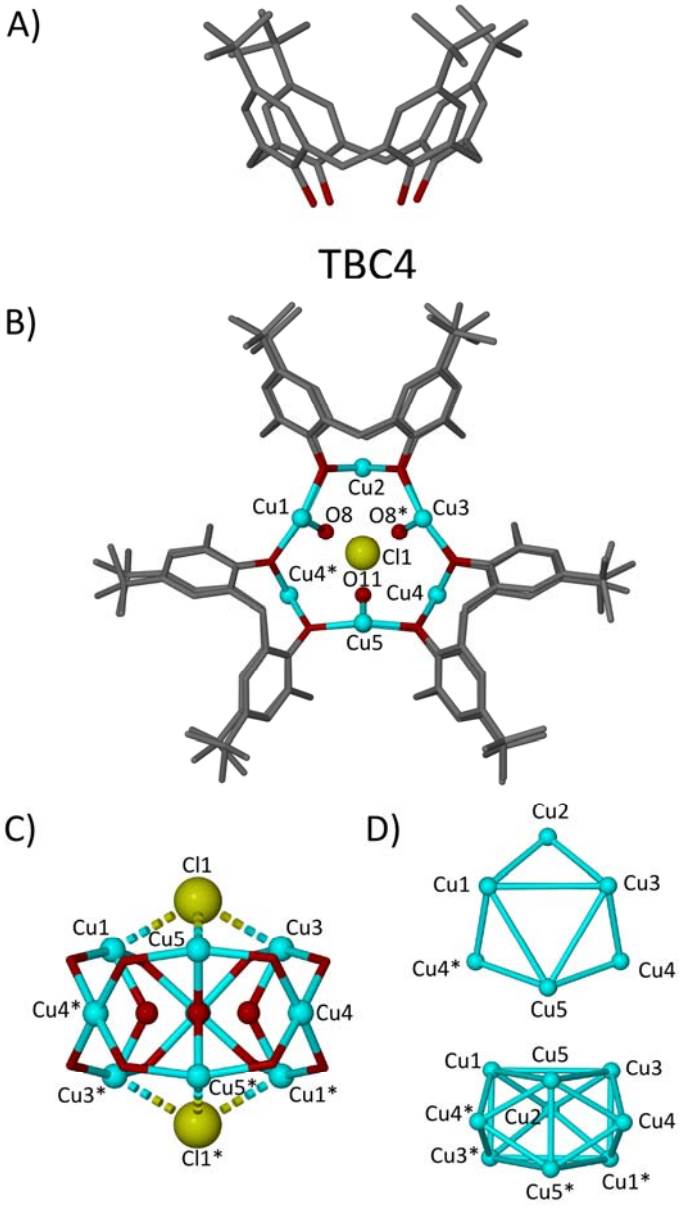

Figure. 2.20 A) Structure of *p*-^{t}But-calix[4]arene. B) The molecular structure of the cation in **6**, viewed down the triangular face of the prism (top). C) The magnetic core of the cation in **6** viewed perpendicular to the triangular face of the prism. Red spheres represent μ_2-OH^- ligands, while red sticks represent TBC4 lower-rim oxygen atoms. Contacts between Cl^- anions and Cu centres are shown as dashed lines. D) Orthogonal views of the tri-capped trigonal prismatic core of the cation in **6**. Colour code: Cu(II) = light blue, O = red, Cl = yellow. Hydrogen atoms, both non-coordinating and coordinating DMSO ligands, and the $Cu^{I}Cl_2$ anion have been omitted for clarity. Figures not to scale.

Within the trigonal prism, the two triangular faces are linked to each other via three μ_2-OH^- ligands (O8, O11 and O8*) along each vertical edge of the prism

(Fig. 2.20C). The μ_5-TBC4 ligands use all four μ_2-O-atoms to chelate the face-capping Cu^{II} ions (Cu2, Cu4 and Cu4*), further bridging to each of the Cu ions on the vertices of the square face of the prism (Fig. 2.20C). The Cu^{II} ions defining the trigonal prism are 5-coordinate when considering the contacts with Cl^- anions and the coordination of DMSO molecules. The face capping Cu^{II} ions are square planar, being bonded only to the O-atoms of the TBC4 ligand. The cation in **6** carries an overall charge of 1+, and charge balance is provided by the linear $[Cu^{I}Cl_2]^-$ anion (Fig. 2.21).[16]

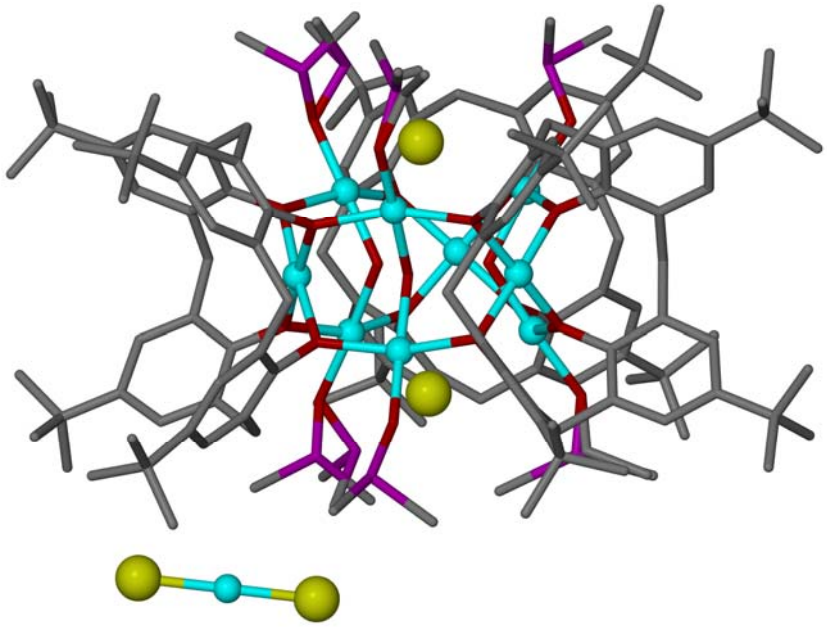

Figure 2.21. Cluster and the $Cu^{I}Cl_2$counterion found in the single crystal structure of **6**.

The cation in **7** is analogous to that of **6**, the only difference being in the triangular face-capping anions. Two ["η^1, μ_3"] NO_3^- anions, one of which is disordered over two positions, reside at the "upper" and "lower" triangular faces of the prism (Fig. 2.22 and 2.23).

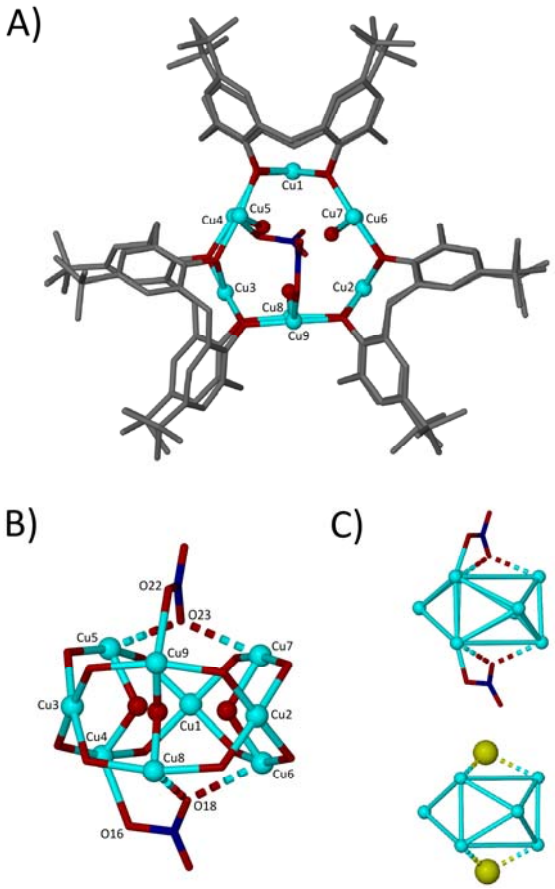

Figure. 2.22 A) The molecular structure of the cation in **7**, viewed down the triangular face of the prism (top). B) The magnetic core of the cation in **7** viewed perpendicular to the triangular face of the prism. Additional contacts between NO_3^- anions and Cu centres are shown as dashed lines. C) Tri-capped trigonal prismatic cores of the cations in **6** and **7** showing distortion due to nitrate anions. Colour code: Cu(II) = light blue, O = red, Cl = yellow, N = dark blue. Hydrogen atoms, both non-coordinating and coordinating solvent molecules and the additional NO_3^- anion have been omitted for clarity. The disordered nitrate anion in the core of **7** is shown in only one position. Figures not to scale.

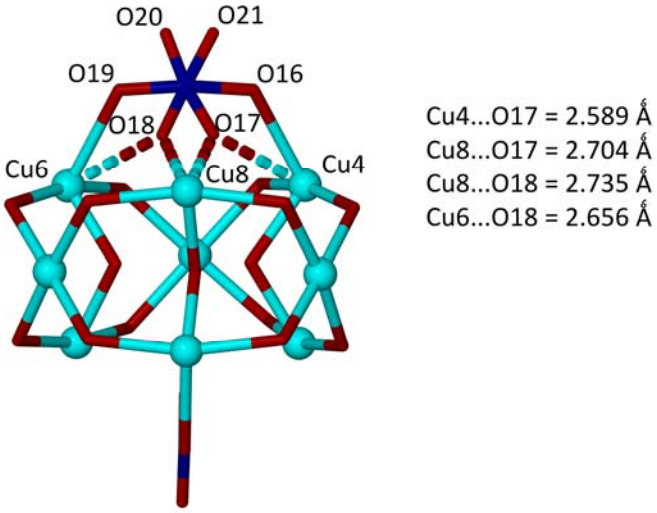

Figure 2.23. Detailed information relating to the coordination and long contacts associated with the disordered NO_3^- anion in the cation found in **7**.

The ordered nitrate anion coordinates to Cu9 with an N-O22-Cu bond length of 2.383 Å, and shows long contacts from O23 to Cu5 and Cu7 with distances of 2.669 and 2.625 Å respectively (Fig 2.22B). In one position, the second and disordered anion coordinates to Cu4 with a bond length of 2.337 Å, and shows long contacts from O18 to Cu6 and Cu8 with distances of 2.656 and 2.735 Å respectively (Fig 2.22B). Similar distances are observed in the second disordered position (Fig. 2.23). As in **6**, the anions in **7** reside in hydrophobic pockets generated by ligated DMSO molecules on the Cu centres of the trigonal prism (Fig. 2.24).

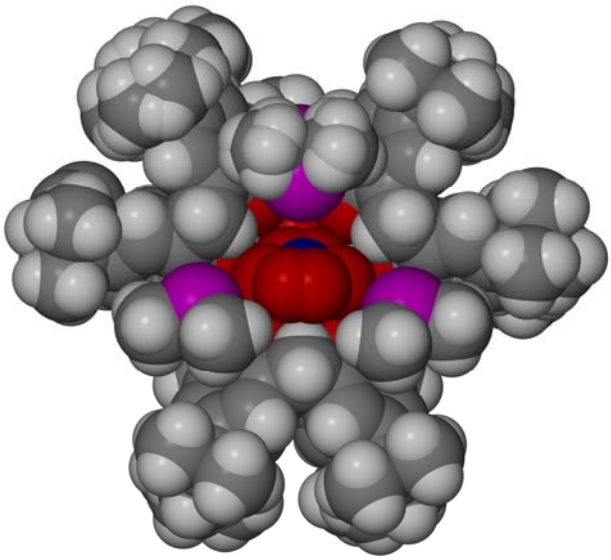

Figure 2.24. Space filling representation of the disordered NO_3^- anion residing in the pocket generated by ligated DMSO molecules on the Cu centres of the trigonal prism in cation **7**.

The disordered anion within the cation in **7** lies near perpendicular to its ordered equivalent, and this "asymmetric bonding" of the face-capping NO_3^- appears to cause a structural distortion of the metallic core skeleton relative to that observed in **6** (Fig. 2.22C). In this distortion, one of the triangular faces of the prism becomes more scalene and twisted with respect to the other. The cation in **7** also carries a +1 charge, and an additional (and disordered) NO_3^- counter anion present in the crystal lattice provides charge balance.

Examination of the extended structures of both **6** and **7** show interesting features when compared with the DMSO solvate of TBC4 (Fig. 2.25). The solvate forms a commonly observed up-down bi-layer arrangement (Fig. 2.25A),[17a,b] where each TBC4 cavity lies opposite ^{t}Bu groups from a neighbouring bi-layer, and is occupied by a disordered DMSO molecule.[17c] The calixarene cavities in both **6**and **7** are also found to be occupied by DMSO molecules, some of which are disordered. In addition, interstitial spaces are occupied by disordered DMSO molecules and Cu^ICl_2 or disordered NO_3^- anions in **6** and **7** respectively. Although the cationic fragments in **6** and **7** are similar in shape, these pack in rather different ways, both of which mimic the nature of TBC4 bi-layer formation within sheets.[17] As shown in Figure 2.25B, the cationic fragments in **6** pack so that each calixarene cavity is opposite a solvent occupied space between two cluster bound TBC4 molecules. This space itself is reminiscent of a calixarene cavity due to the angle between neighbouring TBC4 molecules within the fragment, thereby giving rise to bi-layer type character within a sheet of cations. The cationic fragments in **7** pack in such a way that three different types of solvent or anion occupied void are observed (Fig. 2.25C). In the central fragment shown in Figure 2.25C, two TBC4 cavities are opposite calixarene cavities of neighbouring clusters. The third TBC4 cavity within this fragment is opposite a space between two calixarenes in a neighbouring cluster, which is similar to the packing observed in **6**. Finally, two spaces between neighbouring TBC4s in the central fragment in Figure 2.25C are found to be opposite spaces from neighbouring catioins. These differences show that despite having very similar shapes, these species are capable of packing in markedly different manners to mimic the behaviour of TBC4 in bi-layer form.[17]

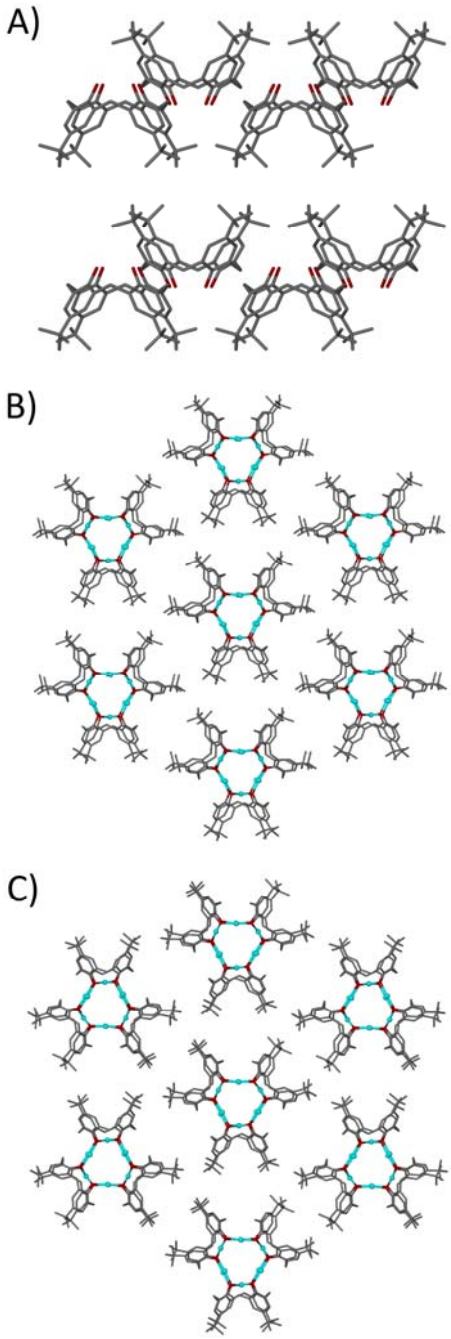

Figure. 2.25 A) The bi-layer arrangement found in the TBC4·DMSO solvate.[17] B) Packing of pseudo-trigonal planar cation fragments in **6**. C) Packing of pseudo-trigonal planar cation fragments in **7**. Hydrogen atoms and solvent molecules are omitted for clarity. Anions and ligated solvent molecules are omitted in B and C for clarity. Figures not to scale.

Solid state dc magnetic susceptibility (χ_M) data on dried **6** and **7** were collected in a 0.1 T field in the 5-300 K range. Since both show the same behaviour we describe **7** only.

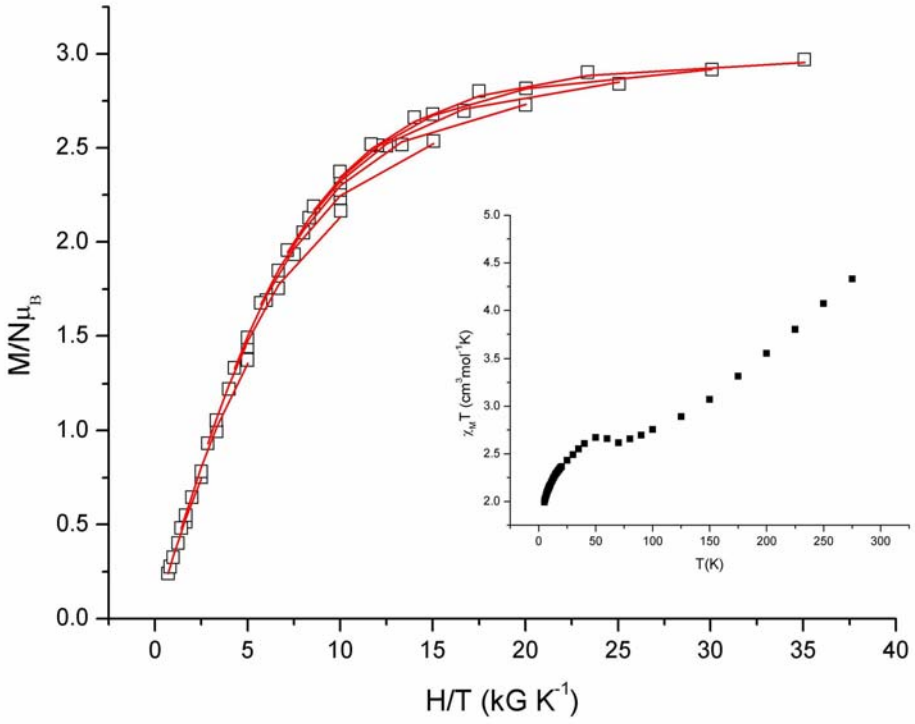

Figure 2.26. Plot of reduced magnetisation ($M/N\mu_B$) versus H/T measured in the 0.5 - 7 T field range between 2 - 7 K. The red lines represent the fit of the experimental data by a matrix diagonalization method employing the Hamiltonian $\hat{H} = D(\hat{S}_z^2 - S(S + 1)/3) + \mu_B g H \hat{S}$. This gives an S = 3/2 ground state with g = 2.02 and D = -0.1 cm^{-1}. The inset shows a plot of $\chi_M T$ versus T in the 300 - 5 K temperature range using an applied field of 0.1 T.

The $\chi_M T$ value at 300 K of 4.25 cm^3 K mol^{-1} (Figure 2.26) is near that expected for a [Cu$^{II}_9$] unit with g = 2.25 (4.27 cm^3 K mol^{-1}). As the temperature is decreased the value of the $\chi_M T$ product decreases rapidly to ~2.6 cm^3 K mol^{-1} at 100 K where it plateaus, before decreasing once more below ~40 K. The data suggests relatively strong antiferromagnetic exchange between the Cu(II) ions with the low temperature plateau indicative of an S = 3/2 ground state [and the <40 K drop assigned to intermolecular interactions and/or Zeeman effects]. The value of the

ground state is confirmed by magnetisation measurements (Figure 2.26) performed in various magnetic fields and in the 1.8-10 K temperature range which saturate at $M/N\mu_B \approx 3$. If one assumes that the larger Cu-O-Cu angles the stronger the AF exchange [Cu-O(H)-Cu > Cu-O(TBC4)-Cu], then a cartoon picture of the ground state is one of the Cu ions in the trigonal prism being "spin-up" and the face capping Cu ions being "spin-down".

In conclusion we have synthesised and characterised a new enneanuclear tri-capped trigonal prismatic Cu(II) cluster that is supported by calixarene ligands. The facile exchange of anions in the cluster core suggests that the formation of this motif is highly favoured, and that the anion binding pocket on either side of the prism is capable of adapting to anions of markedly different nature. The clusters are pseudo-trigonal planar and show versatility in packing behaviour, mimicking aspects of the solid state behaviour of TBC4. Future studies will explore cluster versatility towards different anions, and exchange of DMSO ligands both on the Cu(II) centres around the trigonal faces of the prism, and within the cavities of the calixarenes. Such alteration may have profound effects on the assembly of the clusters in the solid state and the resulting magnetic properties of these new complexes.

Syntheses

All reactions were performed under aerobic conditions and all reagents and solvents were used as purchased.

$MnCl_2 \cdot 4H_2O$ (0.1 g, 0.5 mmol) and TBC4 (0.1 g, 0.15 mmol) were dissolved in a mixture of DMF (10 ml) and MeOH (10 ml) and stirred for 1 hour. X-ray quality crystals were obtained in good yield (40%) after slow evaporation of the mother liquor. Elemental analysis (%) calculated for $C_{106}H_{146}Mn_4N_6O_{16}$: C 64.30, H 7.43, N 4.24; Found: C 64.02, H 7.54, N 4.21.

Crystal data for TBC4·DMF: $C_{47}H_{63}N_1O_5$, M = 722.0, Colourless Block, 0.50 × 0.42 × 0.38 mm^3, tetragonal, space group $P4/n$ (No. 85), $a = b$ = 12.6880(18), c =

13.001(2) Å, V = 2093.0(5) Å^3, Z = 2, Bruker Nonius X8 Apex II diffractometer, Mo-K□ radiation,□□ = 0.71073 Å, T = 100(2)K, 2□$_{max}$ = 49.8º, 7253 reflections collected, 1825 unique (R_{int} = 0.0613). Final *GooF* = 1.134, *R1* = 0.0652, *wR2* = 0.1650, *R* indices based on 1340 reflections with I >2sigma(I) (refinement on F^2). A number of restraints were applied due to disorder in the DMF guest molecule and the ^{t}Bu groups of the TBC4. CCDC number: 741028.

Crystal data for 1: $C_{108}H_{154}Mn_4N_6O_{18}$, M = 2044.13, Purple Block, 0.44 □ 0.38 □ 0.20 mm^3, monoclinic, space group $P2_1/c$ (No. 14), a = 20.455(3), b = 11.2777(17), c = 24.513(4) Å,□□ = 111.871(2)°, V = 5247.8(13) Å^3, Z = 2, Bruker Apex II CCD diffractometer, Synchrotron radiation,□□ = 0.77490 Å, T = 100(2)K, 2□$_{max}$ = 50.4º, 42709 reflections collected, 7304 unique (R_{int} = 0.0868). Final *GooF* = 1.018, *R1* = 0.0551, *wR2* = 0.1418, *R* indices based on 5120 reflections with I >2sigma(I) (refinement on F^2). CCDC number: 741029.

Unit cell parameters for partial structure of 2: Monoclinic, space group $P2_1/c$ (No. 14), a = 12.6152(23), b = 12.5692(22), c = 28.1584(54) Å,□□ = 105.859(3)°, Bruker Apex II CCD diffractometer, Synchrotron radiation,□□ = 0.77490 Å, T = 100(2)K. Crystal quality precluded full structural characterisation.

$Mn(NO_3)_2{\cdot}4H_2O$ (0.1 g, 0.39 mmol), $Gd(NO_3)_2{\cdot}6H_2O$ (0.1 g, 0.22 mmol) and C4 (0.1 g, 0.23 mmol) were dissolved in a mixture of DMF (10 cm^3) and MeOH (10 cm^3). Following 5 minutes of stirring, NEt_3 (0.2 g, 1.97 mmol) was added dropwise, and the resulting purple solution was stirred for a further hour. X-ray quality crystals were obtained in good yield (40%) after slow evaporation of the mother liquor. Elemental analysis (%) calculated for (**3**), $C_{130}H_{140}Mn_4Gd_4N_8O_{40}$: C 47.27, H 4.27, N 3.39; Found: C 47.02, H 4.14, N 3.27.

Complexes **4** and **5** were made in an analogous manner using $Tb(NO_3)_3{\cdot}6H_2O$ and $Dy(NO_3)_3{\cdot}6H_2O$ in place of $Gd(NO_3)_3{\cdot}6H_2O$. Elemental analysis (%) calculated for (**4**), $C_{135}H_{155}Mn_4Tb_4N_9O_{43}$: C 47.04, H 4.53, N 3.66; Found: C 46.98, H 4.24, N 3.59. Elemental analysis (%) calculated for (**5**), $C_{130}H_{140}Mn_4Dy_4N_8O_{40}$: C 46.97, H 4.24, N 3.37; Found: C 46.51, H 4.18, N 3.25.

General crystallographic details: Data for **3**[20c] and **4** were collected on a Bruker Nonius X8 Apex II diffractometer operating with MoKα radiation (λ = 0.71073 Å) at *T* = 100(2) K. Data for **5** were collected on a Bruker Apex II CCD diffractometer operating with synchrotron radiation (λ = 0.77490 Å) at *T* = 100(2) K. The routine SQUEEZE was applied to the data for **3** – **5** due to the presence of badly disordered solvent molecules.[23] In all cases, this had the effect of dramatically improving the agreement indices. **Crystal data for 3:**[20c] $C_{130}H_{122}Gd_4Mn_4N_8O_{42}$, *M* = 3317.12, Black Block, 0.25 × 0.20 × 0.18 mm^3, monoclinic, space group *C*2/*c* (No. 15), *a* = 34.41(3), *b* = 12.397(9), *c* = 32.15(4) Å, β = 98.14(3)°, *V* = 13576(22) Å^3, *Z* = 4, $2\theta_{max}$ = 46.8º, 56018 reflections collected, 9621 unique (R_{int} = 0.0831). Final *GooF* = 1.015, *R1* = 0.0462, *wR2* = 0.1217, *R* indices based on 7169 reflections with I >2sigma(I) (refinement on F^2). **Crystal data for 4:** $C_{135}H_{155}Mn_4N_9O_{43}Tb_4$, *M* = 3447.12, Black Block, 0.40 × 0.32 × 0.28 mm^3, triclinic, space group *P*-1 (No. 2), *a* = 17.87(5), *b* = 19.62(5), *c* = 23.80(7) Å, α = 102.46(4), β = 104.83(4), γ = 96.28(4)°, *V* = 7754(37) Å^3, *Z* = 2, $2\theta_{max}$ = 46.5º, 143013 reflections collected, 21725 unique (R_{int} = 0.0857). Final *GooF* = 0.977, *R1* = 0.0507, *wR2* = 0.1290, *R* indices based on 14442 reflections with I >2sigma(I) (refinement on F^2). **Crystal data for 5**: $C_{130}H_{140}Dy_4Mn_4N_8O_{40}$, *M* = 3324.26, Purple Plate, 0.20 × 0.06 × 0.02 mm^3, triclinic, space group *P*-1 (No. 2), *a* = 17.805(2), *b* = 19.781(2), *c* = 23.563(3) Å, α = 102.752(2), β = 104.586(2), γ = 96.203(2)°, *V* = 7714.9(15) Å^3, *Z* = 2, D_c = 1.431 g/cm^3, F_{000} = 3320, Bruker Apex II CCD Diffractometer, synchrotron radiation, λ = 0.77490 Å, *T* = 100(2)K, $2\theta_{max}$ = 51.1º, 64375 reflections collected, 22184 unique (R_{int} = 0.0609). Final *GooF* = 0.921, *R1* = 0.0511, *wR2* = 0.1219, *R* indices based on 15071 reflections with I >2sigma(I) (refinement on F^2), 1764 parameters, 147 restraints. Lp and absorption corrections applied, μ = 2.877 mm^{-1}.

$CuCl_2{\cdot}2H_2O$ (0.2 g, 11 mmol) , TBC4 (0.1 g, 0.15 mmol), NH_4ClO_4 (0.117 g, 1 mmol) and NEt_3 (0.2 g, 1.9 mmol) were dissolved in a mixture of 10 cm^3 of DMSO and 10 cm^3 of EtOH and stirred for 3 h. X-ray quality crystals of **6** were obtained in good yield (~45%) after slow evaporation of the mother liquor. Elemental analysis (%) calculated (found) for $C_{144}H_{195}Cu_{10}O_{21}S_6Cl_4$: C, 53.52 (53.90), H 6.08 (5.96). The same procedure was employed for **7**, replacing $CuCl_2{\cdot}2H_2O$ with $Cu(NO_3)_2{\cdot}3H_2O$ (0.2

g, 8.2 mmol) and EtOH with MeOH. Elemental analysis (%) calculated (found) for $C_{144}H_{195}Cu_9N_3O_{30}S_6$: C, 53.84 (54.03), H 6.12 (6.09), N, 1.31 (1.25).

References

[1] G. Aromí, E. K. Brechin, *Struct. Bonding*., **2006**, *122*, 1-69.

[2] (a) C. Ritchie, A. Ferguson, H. Nojiri, H. N. Miras, Y.-F. Song, D.-L. Long, E. Burkholder, M. Murrie, P. Kögerler, E. K. Brechin, L. Cronin, *Angew. Chem. Int. Ed.* **2008**, *47*, 5609 – 5612; (b) M. A. AlDamen, J. M. Clemente-Juan, E. Coronado, C. Martí-Castaldo, A. Gaita-Ariño, *J. Am. Chem. Soc.* **2008**, *130*, 8874 –8875; (c) J.-D. Compain, P. Mialane, A. Dolbecq, I. Martyr Mbomekallé, J. Marrot, F. Sécheresse, E. Rivière, G. Rogez, W. Wernsdorfer, *Angew. Chem. Int. Ed*. **2009**, *48*, 3077 –3081.

[3] A. Giusti, Gaëlle Charron, S. Mazerat, J.-D. Compain, P. Mialane, A. Dolbecq, E. Rivière, W. Wernsdorfer, R. N. Biboum, B. Keita, L. Nadjo, A. Filoramo, J.-P. Bourgoin, T.Mallah, *Angew. Chem. Int. Ed*., **2009**, *48*, 4949-4952.

[4] (a) E. K. Brechin, J. Yoo, M. Nakano, J.C. Huffman, D. N. Hendrickson, G. Christou, *Chem. Commun*., 1999, 783-784; (b) J. Yoo, E. K. Brechin, A. Yamaguchi, M. Nakano, J. C. Huffman, A. L. Maniero, L.-C. Brunel, K. Awaga, H. Ishimoto, G. Christou, and D.N. Hendrickson, *Inorg. Chem*. **2000,** *39*, 3615-3623.

[5] L.M. Wittick, L.F. Jones, P. Jensen, B. Moubaraki, L.Spiccia, K. J. Berry and K. S. Murray, *Dalton Trans.*, 2006, 1534-1543.

[6] For example see: G. D. Andreetti, R. Ungaro, A. Pochini, *J. Chem. Soc., Chem. Commun.*, **1979**, 1005-1007; E. B. Brouwer, G. D. Enright, J. A. Ripmeester, *J. Am. Chem. Soc.*, **1997**, *119*, 5404-5412; J. L. Atwood, L. J. Barbour, A. Jerga, B. L. Schottel, *Science*, **2002**, *298*, 1000-1002.

[7] (a) W. Wernsdorfer, Adv. Chem. Phys., 2001, 118, 99-190; (b) W. Wernsdorfer, Supercond. Sci. Technol., 2009, 22, 064013.

[8]Mereacre, V.; Ako, A.; M.; Filoti, G.; Bartolomé, J.; Anson, C. E.; Powell, A. K. *Polyhedron*, **2010**, 29, 244.

[9] For example see: (a) MacGillivray, L. R.; Atwood, J. L. *Nature*, **1997**, *389*, 469. (b) Orr, G. W.; Barbour, L. J.; Atwood, J. L. *Science*, **1999**, *285*, 1049. (c) Gerkensmeier, T.; Iwanek, W.; Agena, C.; Froehlich, R.; Kotila, S.; Nather, C.;

Mattay, J. *Eur. J. Org. Chem*. **1999**, 2257. (d) Atwood, J. L.; Barbour, L. J.; Dalgarno, S. J.; Hardie, M. J.; Raston, C. L.; Webb, H. R. *J. Am. Chem. Soc.*, **2004**, *126*, 13170. (e) Dalgarno, S. J.; Tucker, S. A.; Bassil, D. B.; Atwood, J. L. *Science*, **2005**, *309*, 2037. (f) Ugono, O.; Holman, K. T. *Chem. Commun*., **2006**, 2144. (g) Barrett, E. S.; Dale, T. J.; Rebek Jr., J. *J. Am. Chem. Soc*. **2007**, *129*, 3818.

[10] Evangelisti, M.; Candini, A.; Affronte, M.; Pasca, E.; de Jongh, L. J.; Scott, R. T. W.; Brechin, E. K. *Phys. Rev. B*, **2009**, *79*, 104414.

[11] (a) Spichkin, Yu. I.; Zvezdin, A. K.; Gubin, S. P.; Mischenko, A. S; Tishin, A. M. *J. Phys. D: Appl. Phys*., **2001**, *34*, 1162. (b) Evangelisti, M.; Luis, F.; de Jongh, L. J.; Affronte, M. *J. Mater. Chem*., **2006**, *16*, 2534.

[12] See for example: (a) Zimm, C.; Jastrab, A.; Sternberg, A.; Pecharsky, V. K.; Gschneidner Jr., K. A.; Osborne, M.; Anderson, I. *Adv. Cryog. Eng*., **1998**, *43*, 1759; (b) Pecharsky, V. K.; Gschneidner Jr., K. A. *J. Magn. Magn. Mater*., **1999**, *200*, 44; (c) Gschneidner Jr., K. A.; Pecharsky, A. O.; Pecharsky, V. K. in *CryocoolersII*, ed. R. S. Ross Jr., Kluwer Academic/Plenum Press, New York, **2001**, p. 433.

[13] Evangelisti, M.; Brechin E, K.; *Dalton Trans*., **2010**, *39*, 4672, and references therein.

[14]. Evangelisti, M.; Luis, F.; Mettes, F. L.; Aliaga, N.; Aromí, G.; Alonso, J. J.; Christou, G.; de Jongh, L. J. *Phys. Rev. Lett.* **2004**, *93*, 117202.

[15] Mydosh, J. A. in "Spin glasses: an experimental introduction", Taylor and Francis, London, 1993.

[16] A CCDC search gives a total of 92 hits. See for example: A. Khan, J. D. Silversides, L. Madden, J. Greenman and S. J. Archibald, *Chem. Commun*. 2007, 416; Y. Ueno, Y. Tachi and S. Itoh, *J. Am. Chem. Soc*., **2002**, 124, 12428.

[17] (a) J. A. Ripmeester, G. D. Enright, C. I. Ratcliffe, K. A. Udachin, I. L. Moudrakovski, *Chem. Commun.*, **2006**, 4986; (b) S. J. Dalgarno, P. K. Thallapally, L. J. Barbour and J. L. Atwood, *Chem. Soc. Rev.* **2007**, 36, 236; c) B. M. Furphy, J. B. Harrowfield, M. I. Ogden, B. W. Skelton, A. H. White, F. R. Wilner, *J. Chem. Soc., Dalton Trans.* **1989**, 2217.

Chapter 3: A Family of Double-Bowl Pseudo Metallocalix[6]arene Discs

Introduction

This chapter reports the synthesis and magnetic characterisation of a series of planar $[M_7]$ (M = Ni^{II}, Zn^{II}) disc complexes $[Ni_7(OH)_6(L_1)_6](NO_3)_2$ (**8**), $[Ni_7(OH)_6(L_1)_6](NO_3)_2.2MeOH$ (**9**), $[Ni_7(OH)_6(L_1)_6](NO_3)_2.3MeNO_2$ (**10**), $[Ni_7(OH)_6(L_2)_6](NO_3)_2.2MeCN$ (**11**), $[Zn_7(OH)_6(L_1)_6](NO_3)_2.2MeOH.H_2O$ (**12**) and $[Zn_7(OH)_6(L_1)_6](NO_3)_2.3MeNO_2$ (**13**) (where HL_1 =2-iminomethyl-6-methoxy-phenol, HL_2 = 2-iminomethyl-4-bromo-6-methoxy-phenol). Each member exhibits a double-bowl *pseudo* metallocalix[6]arene topology whereby the individual $[M_7]$ units form molecular host cavities which are able to accommodate various guest molecules (MeCN, $MeNO_2$ and MeOH). Magnetic susceptibility measurements carried out on complexes **8** and **11** indicate weak exchange between the Ni^{II} centres.

Supramolecular chemistry has rapidly become a vast and multidisciplinary field with applications including catalysis,[1] anion sensing recognition,[2] gas sequestration / storage[3] and species transportation towards drug delivery,[4] and consequently is of interest to scientists of wide ranging disciplines. One particularly interesting facet of supramolecular chemistry concerns the expression of high degrees of local and extended topological control onto a molecule (e.g. a host unit) in terms of its partaking in intermolecular interactions with other species (e.g. a guest molecule). This is achieved via careful structural manipulation of these molecules (and molecular assemblies) giving rise to complex molecular architectures possessing targeted synergic chemical and physical properties. Although supramolecular host-guest chemistry has been readily exhibited and widely reported with a vast array of organic receptor moieties,[5] the engagement of magnetically interesting inorganic host units is still relatively rare.[6] In the previous chapter the fields of supramolecular chemistry and molecular magnetism were combined to produce tetranuclear $[Mn_4]$ Single-Molecule Magnets[7] and a $[Mn_4Gd_4]$ magnetic cooler,[8] each built entirely using bowl-like calix[4]arene ligands - a cyclophane synonymous with host-guest supramolecular chemistry.[9] By

employing this particular ligand attempts have been made to purposefully exercise site specific cluster growth (i.e. the $\{Mn_4\}$ and $\{Mn_4Gd_4\}$ motifs can only be formed at the lower rim of the Calix[4]arene ligands) and spatial separation of the individual $[Mn_4]$ units to promote magnetic dilution.[10]

In this chapter the synthesis and characterization of a family of ferromagnetic planar disc $[Ni_7]$ complexes which possess double-bowl metallocalix[6]arene topologies and themselves exhibit host-guest behaviour allowing direct comparison to supramolecular calix[*n*]arene behaviour is reported. The work described in detail below serves as an extension to our initial findings, namely the report on the founder members of this extended family.[11]

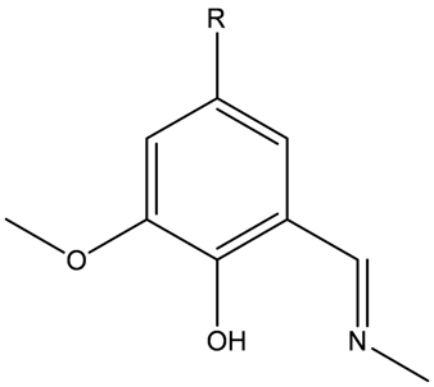

Scheme 3.1: Structure of the Schiff base ligands HL_1 and HL_2 utilised in this work (R = H (HL_1), Br (HL_2)).

Results and Discussion

The first complex of this series to be discovered was the heptanuclear complex $[Ni_7(\mu_3\text{-}OH)_6(L_1)_6](NO_3)_2$ (**8**) which was obtained via the ethanolic reaction of $Ni(NO_3)_2{\cdot}6H_2O$ and HL_1 (Scheme 3.1) in the presence of NaOH. The green hexagonal crystals of **8** crystallize in the trigonal space group P-3c1 in approximately 30% yield (Fig. 3.1). The core in **8** is best described as a body centred hexagon whereby six Ni^{II} ions surround a central Ni^{II} centre to form a planar disc. Although topologically analogous $[Mn_7]$,[12] $[Fe_7]$[13] and $[Co_7]$[14] complexes are known, the synthesis of **8** represents the first example for Ni^{II}. All Ni^{II} centres exhibit distorted octahedral geometries. The six μ_3-bridging OH^- ions (O1 and symmetry equivalent, s.e) link the central nickel (Ni1) to the six peripheral nickel ions (Ni2 and s.e.). The central Ni^{II} ion is located at a site with imposed $\bar{3}$ symmetry with the NO_3^- nitrogen atom (N2) sitting on a threefold axis. The remainder of the asymmetric unit comprises a second Ni^{II} centre (Ni2) along with one L^- unit and one hydroxy group (O1-H1) occupying general positions. Each of the six trigonal pyramidal OH^- ions are situated alternately above and below the $[Ni_7]$ plane (Figure 3.1). The six singly deprotonated (at the phenolate site) L_1^- ligands bridge the peripheral Ni^{II} centres via a $\mu\text{-}\eta^1\text{:}\eta^2\text{:}\eta^1$ coordination mode. These ligands are situated alternately above and below the $[Ni_7]$ plane which gives rise to a double-bowl conformation in which the $[Ni_7]$ core is the basal plane, reminiscent of a metallocalix[6]arene concave unit (Figure 3.1). Full crystallographic parameters obtained for **8** (and all other members) are documented in Table 3.1.

Table 3.1: Crystallographic data for complexes 8-11

	8	**9**	**10**	**11**
Formula[a]	$C_{54}H_{66}N_8O_{24}Ni_7$	$C_{56}H_{66}N_8O_{26}Ni_7$	$C_{57}H_{75}N_{11}O_{30}Ni_7$	$C_{58}H_{66}Br_6N_{10}O_{24}Ni_7$
M_W	1622.12	1678.14	1709.25	2177.64
Crystal System	Trigonal	Trigonal	Trigonal	Monoclinic
Space group	P-3c1	P-3c1	P-3c1	C2/c
a/Å	13.806(2)	13.913(2)	13.933(2)	28.8575(14)
b/Å	13.806(2)	13.913(2)	13.933(2)	11.1352(3)
c/Å	23.270(5)	23.141(5)	22.742(5)	27.4079(13)
α/°	90	90	90	90
β/°	90	90	90	109.603(3)
γ/°	120	120	120	90
V/Å^3	3841.2(11)	3879.6(11)	3823.4(11)	8296.6(7)
Z	2	2	2	4
T/K	150	150	150	150
λ[b]/Å	0.71070	0.71070	0.71070	0.71070
D_c/g cm^{-3}	1.402	1.437	1.485	1.743
μ(Mo-Ka)/ mm^{-1}	1.749	1.736	1.762	1.516
Meas./indep.(R_{int}) refl.	2306 / 1376 (0.0802)	2335 / 2034(0.0679)	2333 / 1835(0.0502)	7348 / 3779 (0.0511)
wR2 (all data)	0.2446	0.2155	0.1725	0.1325
$R1$[d,e]	0.1209	0.0751	0.0604	0.1090
Goodness of fit on F^2	1.091	1.047	1.191	0.852

[a] Includes guest molecules.[b] Mo-Kα radiation, graphite monochromator. [c] $wR2= [\Sigma w(|F_o^2| - |F_c^2|)^2 / \Sigma w|F_o^2|^2]^{1/2}$. [d]For observed data. [e] $R1= \Sigma||F_o| - |F_c|| / \Sigma|F_o|$.

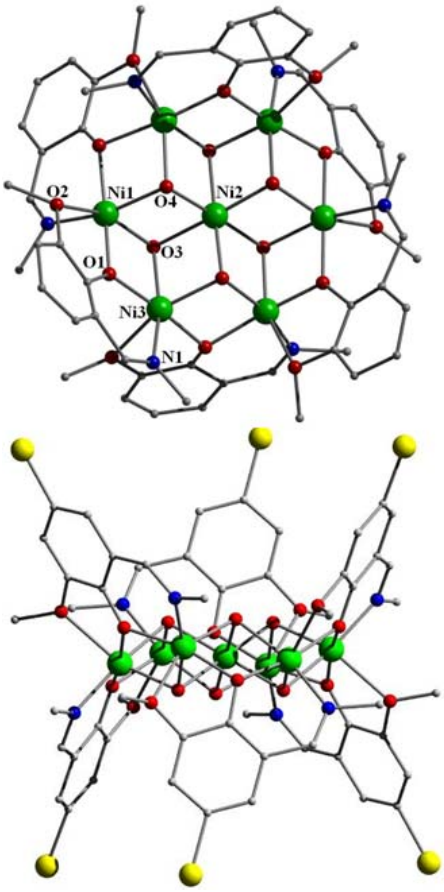

Figure 3.1: Molecular structures of complexes 8 (top) and 4 (bottom) viewed perpendicular and parallel to the [Ni_7] plane respectively.

Close scrutiny of the double-bowl conformation in **8** shows approximate bowl dimensions of 6.20 × 4.21 × 11.70 Å (base × depth × rim diameter). The [Ni_7] units in **8** stack on top of one another resulting in the formation of psuedo-superimposable 1D columns (Figure 3.1 bottom) whereby each moiety is spaced at a $[Ni_7]_{plane}$-$[Ni_7]_{plane}$ distance of 11.64 Å.[13] Furthermore the unit cell in **8** possesses four such 1D columns, each unit linked by a 120º rotation (Figure 3.2).

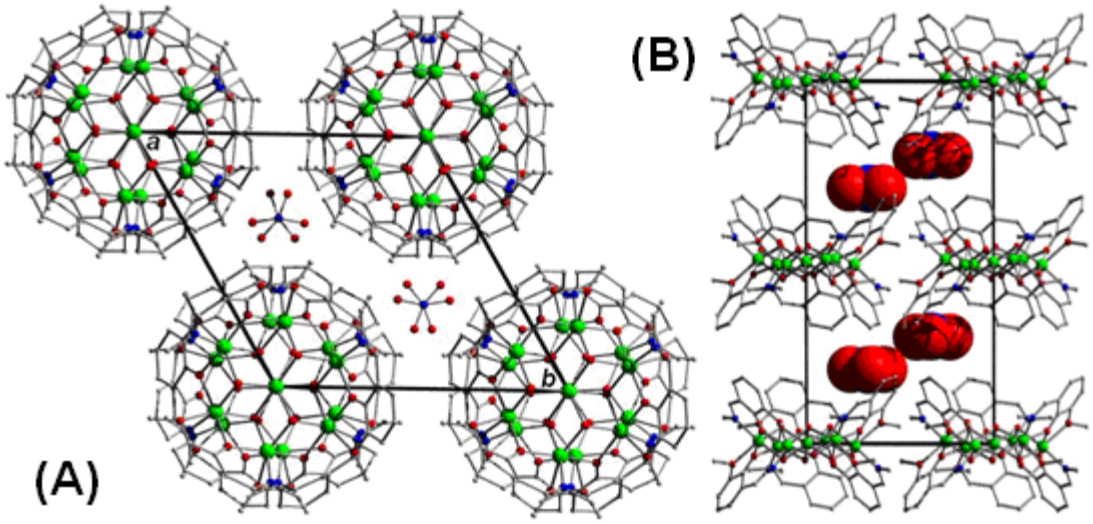

Figure 3.2: (A) Crystal packing observed in 8 as viewed down the *c* axis of the unit cell respectively. Note that packing of 9 is identical to that of 8 minus disordered $MeNO_2$ guests. (B) View along *a* axis of the cell in 8. H-atoms omitted for clarity. Large spheres represent NO_3^- counter anions.

The [Ni_7] moieties are connected into 1D columnar arrays *via* zig-zag shaped belts of NO_3^- anions (each comprising six NO_3^- ions), located above and below the individual [Ni_7] units with C-H···O bonding interactions between the NO_3^- oxygen atoms (one unique, O4) and protons (H1A and H5) of the L_1^- ligands (H1A···O4 = 2.59 Å and H5···O4 = 2.44 Å). The NO_3^- belts act as 'molecular zips' by pairing up individual [Ni_7] complexes to form molecular cavites each of approximate volume ~265.9 $Å^3$,[15] formed by two juxtaposed pseudo metallocalix[6]arene [Ni_7] bowl units (Figure 3.4 below). For complete molecular cavity dimensions in the crystal of **8** (and all other analogues) see Table 3.2.

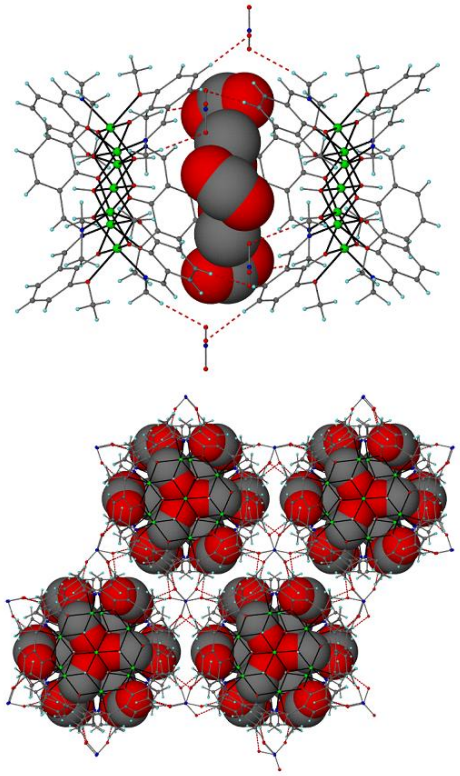

Figure 3.3: Crystal structure of 9 as viewed perpendicular to the [Ni_7] cores; (bottom) Crystal packing observed in 9. Dashed lines represent H-bonding interactions within the individual [Ni_7] units in 9. The guest disordered MeOH molecules are shown as space filled spheres (red = O, grey = C).

Although void of guest moieties, the fascinating double bowl metallocalix[6]arene cavities observed in **8** led to their investigation as rare examples of paramagnetic host receptors. Initial work involved the replacement of EtOH (used in production of the *empty* host **8**) with the smaller MeOH solvent in order to encourage guest occupancy. This was proved successful with the isolation of the host-guest complex $[Ni_7(OH)_6(L_1)_6](NO_3)_2.2MeOH$ (**9**), which crystallises in the same trigonal P-31c space group as **8** in ~40% yield. This improved yield when compared to the preparation of **8** is presumably due to the increased solubility of NaOH in MeOH. Complex **9** also exhibits a central Ni^{II} (Ni1) of imposed $\bar{3}$ symmetry and a N atom of the NO_3^- counter anion (N2) located on a threefold rotation axis. The molecular cavities in **9** are similar to those in **8** (6.20 × 4.16 × 11.81 Å (base × depth × rim diameter)), while the $[[Ni_7]_{plane}$-$[Ni_7]_{plane}$ distance of 11.57 Å is also comparable to that of **8** (Table 3.2 below). Complex **9** differs with respect to **8** only in that the H-bonded cavities in **9** (of calculated volume of ~

293.7 $Å^3$) are of the required dimensions to accommodate two guest MeOH molecules. When small molecules are located within such highly symmetrical molecular cavities, it is common to observe crystallographic disorder and the MeOH guest molecules in **9** are no exception.

The first disordered MeOH guest (atoms C20-O10) has only $1/6^{th}$ occupancy and thus periodically occupies positions in between the NO_3^- counter anions (which form the aforementioned zig-zag belt) and partakes in H-bonding interactions (O4…O10 = 2.86 Å). The second MeOH guest (C21-O9) lies within the molecular cavity in **9** at the midpoint between the two [Ni_7] planes (possessing a two-fold axis along the C-O vertex) where it is also disordered over three sites with respect to the three fold rotation axis inherent to the cell (Figure 3.3). This central MeOH guest shows no significant signs of supramolecular interactions within or outwith its host cavity. This is not particularly surprising as this central MeOH guest moiety lies over 4 Å away from the nearest μ_3-OH^- protons (O1(H1)…O9 = 4.10 Å).

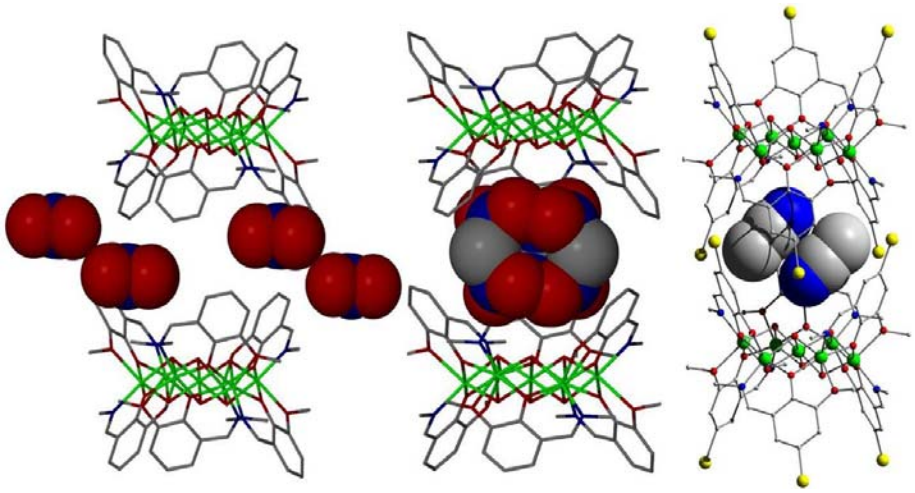

Figure 3.4: Molecular structures of 8, 10 and 11 highlighting (left) the empty cavity and belt of NO_3^- anions in 8, (middle) the disordered guest $MeNO_2$ molecules in 10 and (right) the two MeCN guests located inside the cavities of 11.

It was decided to attempt the encapsualtion of a larger guest molecule which would invoke H-bonding interactions within the molecular cavity and promote affinity towards its host receptor. It was decided to utilise $MeNO_2$ unit as a potential guest on the assumption that its O-atoms would interact with the H atoms of the μ_3-OH^- bridges within the [Ni_7] host cavity units. This was achieved,

producing the complex $[Ni_7(OH)_6(L_1)_6](NO_3)_2 \cdot 3MeNO_2$ (**10**), formed by dissolution and recrystallisation of **8** from $MeNO_2$ in ~15 % yield. In the crystals of **10** the host cavity has a calculated volume of 283.8 $Å^3$ and is occupied by three $MeNO_2$ guests which are related crystallographically via a three fold rotation. As

	8	**9**	**10**	**11**
Cavity Volume ($Å^3$)	265.9	293.7	283.8	265.9

observed in **9**, the trigonal planar $MeNO_2$ guests also experience disorder whereby the methyl carbon atoms (C10 and s.e) lie on a two fold axis. These orientations are most likely to exist in the up-down-up anti-parallel configuration with respect to the three fold rotation symmetry they share, as any other spatial arrangement would result in significant steric effects (Figure 3.4). As predicted the three interact within the cavity via hydrogen bonding interactions between their O-atoms (O5 and O6) and the nearby μ_3-OH^- protons of the two $[Ni_7]$ units which line the cavity floors (O1···O5 = 3.08 Å; O1···O6 = 3.25 Å).

In order to alter the interior size and shape of the molecular cavities highlighted in **8-10** towards subsequent modification and / or control of guest preference, it was decided to attempt to increase the bowl depth (in relation to complexes **8-10**) by utilising the Br-analogue of HL_1, namely the pro-ligand 2-iminomethyl-4-bromo-6-methoxy-phenol (HL_2). To this end an ethanolic solution of $Ni(NO_3)_2.6H_2O$, the ligand HL_2 and NaOH was left to stir for 4 h. The mother liquor was then left evaporate slowly, but no crystalline product was obtained. The subsequent green powder produced was redissolved in numerous *potential guest* solvents (MeOH, $MeNO_2$, MeCN). Interestingly only the MeCN guest species was successfully incorporated in the form of the complex $[Ni_7(OH)_6(L_2)_6](NO_3)_2 \cdot 2MeCN$ (**11**), which was formed in ~23 % yield and crystallises in the monoclinic C2/c space group (cf. **8-10**). In this case each cavity accommodates two MeCN molecules which exhibit a head-to-tail conformation (Figure 3.4 (right)). The MeCN guests are held in place via H-bonding between their N-atoms (N5) and a proton (H3A) of an μ_3-OH^- bridging ion belonging to the neighbouring $[Ni_7(OH)_6]$ core (N5···H3A(O3) = 2.36 Å).

Cavity dimensions (Å) (base × depth × rim)	6.20 × 4.21 × 11.70	6.20 × 4.16 × 11.81	6.20 × 4.08 × 12.04	6.22 × 6.18 × 11.90
$[M_7]_{plane}$-$[M_7]_{plane}$ dist. (Å)	11.64	11.57	11.37	11.14

Table 3.2: Molecular Cavity dimensions observed in the crystals of 8-11

The central Ni^{II} ion (Ni4) located at the centre of **11** lies on an inversion centre with the remaining three metal centres (Ni1-3) and all other atoms in the asymmetric unit occupying general positions. The employment of L_2^- in the construction of **11** does indeed significantly alter the cavity size and shape, as the crystal structure shows the formation of a deeper bowl of dimesions 6.22 × 6.18 × 11.90 Å (base × depth × rim diameter). As observed in **8-10** the individual $[Ni_7]$ units in **11** again arrange into superimposable 1D columns, which propagate along the *b* direction of the unit cell. The stacking of the $[Ni_7]$ units along *b* is supported by two complementary O-H···Br interactions which involve one μ_3-OH^- (H1) of a $[Ni_7]$ unit and the bromine atom (Br1) of a neighbouring $[Ni_7]$ moiety (H1···Br1 = 2.82 Å). These hydrogen bonds direct molecular cavities which differ from those in **8-10** as here they are tilted with respect to the $[Ni_7]$ planes and are interlocked in a staggered arrangement (Figure 3.4). The $[Ni_7]_{plane}$-$[Ni_7]_{plane}$ distance inside the cavity is 11.14 Å and represents a cavity height reduction of ~0.4 Å *cf.* **8-10**. We postulate that this is attributed to the significant H-bonding affinity of the pendant Br-atoms (Br1) in **11**, producing a more tightly embraced cavity of approximate volume 265.9 $Å^3$, which is significantly smaller than those of **8** (265.9 $Å^3$), **9** (293.7 $Å^3$) and **10** (283.8 $Å^3$).

Efforts to encapsulate MeCN and $MeNO_2$ solvent guests inside the cavities of **9** and **11**, respectively, were unsuccessful. These findings suggest that guest molecules can only be placed within such cavities if and when they are able to orientate themselves into certain topologies comprising symmetry elements

compatible with their host lattices. This hypothesis is supported by the formation of complex **10** in which three MeOH guests, linked via a three-fold rotation axis, are accommodated inside the trigonal P-3c1 cell whereas attempts at producing a MeOH guest analogue to **11** (in a monoclinic C2/c cell) remain fruitless. It must be noted that the size and shape of the molecular cavities in such complexes will also reflect their resultant guests and must also be considered here. Attempts at encapsulating larger organic moieties (inc. fluorophores, amino acids and anions) have so far been unsuccessful. Indeed all attempts at such encapsulation simply resulted in the recrystallisation of complexes **8**-**11** (depending on the synthon employed). We may postulate that this is due to the ubiquitious nature of the solvent molecules present in our reaction mixtures which will inevitably become guests within our host [Ni_7] discs.

3D Connectivity of 8-11

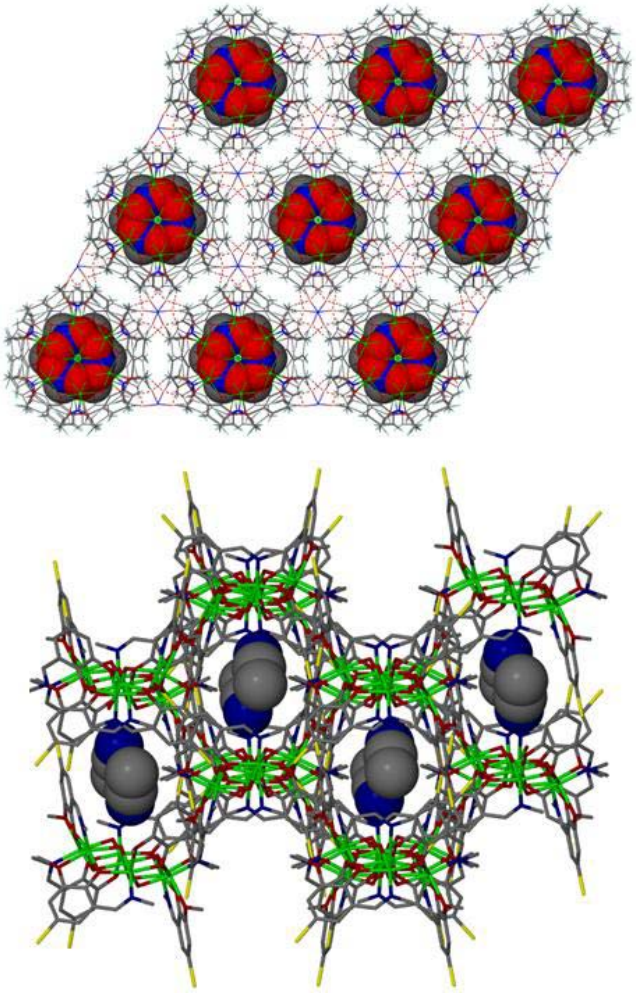

Figure 3.5: Crystal packing observed in the crystals of 10 (top) and 11 (bottom) showing the molecular cavities accommodating guest $MeNO_2$ (red spheres), and MeCN (grey / blue spheres) solvent molecules respectively. NO_3^- counter anions have been omitted for clarity.

Complexes **8-10** crystallise in the trigonal P-3c1 space group and only differ in terms of their guest occupancy and therefore are analogous in terms of their 3D connectivity. The $[Ni_7]$ columns in their unit cells are connected via H-bonds to adjacent 1D $[Ni_7]$ columns. These connections are manifested by a myriad of H-bonding interactions between the NO_3^- counter anions and the individual $[Ni_7]$ moieties. More specifically each $[Ni_7]$ is H-bonded to twelve NO_3^- counter anions which in turn connect to six other $[Ni_7]$ units thus creating a (6,12)-connected net with a $(4^{15})_2(4^{48}.6^{18})$-**alb** topology (Figure 3.6).[16,17] As previously stated,

$[Ni_7(OH)_6(L_2)_6](NO_3)_2.2MeCN$ (**11**) crystallises in the monoclinic C2/c space group and as such possesses a 3-D connectivity different to that of **8-10**. The 1D columnar stacks of $[Ni_7]$ units in **11** are linked by C-H···Br interactions through the Br atoms (Br2 and Br3) of the bridging L_2^- ligands and the $-CH_3$ protons (H18B and H27B) of adjacent $[Ni_7]$ moieties (H18B···Br3 = 2.93 Å, H27B···Br2 = 2.70 Å and *s.e*). The result is a 3-D connectivity comprising a 10-connected net with a $(3^{12}.4^{28}.5^5)$-**bct** topology (Figure 3.6).[16,17]

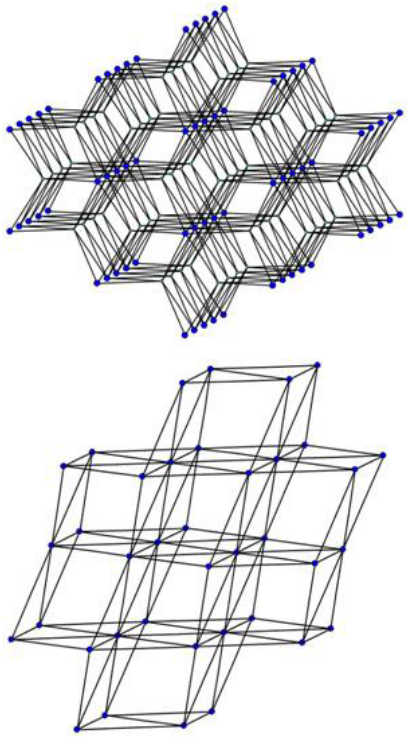

Figure 3.6: The (6,12)-connected net with a $(4^{15})_2(4^{48}.6^{18})$-alb topology in 8-10. Blue spheres represent the 12-connected $[Ni_7]$ units. Cyan spheres represent the 6-connected NO_3^-. (bottom) The 10-connected $(3^{12}.4^{28}.5^5)$-bct in 11 where the blue spheres represent the 10-connected $[Ni_7]$ units.

IR spectroscopic studies on the host complexes **9**, **10** and **11** were performed to ascertain whether their guest molecules remained within their respective H-bonded cavities on drying. CHN analysis on samples of complexes **9-11** were consistent with guest residency. The IR spectrum of $[Ni_7(OH)_6(L_1)_6](NO_3)_2.2MeOH$ showed broad OH stretching bands (centred at 3416 cm^{-1}) attributed to both the μ_3-OH^- bridges and MeOH guest solvent molecules. However there was also a possibility that such bands were due to adsorbed MeOH solvent molecules and therefore the

same sample was subsequently dried under vacuum for 2 h prior to re-analysis of its IR spectrum. It was found that the initial broad OH stretching band had lost intensity on drying and was now centred at 3406 cm^{-1} (Figure 3.7).

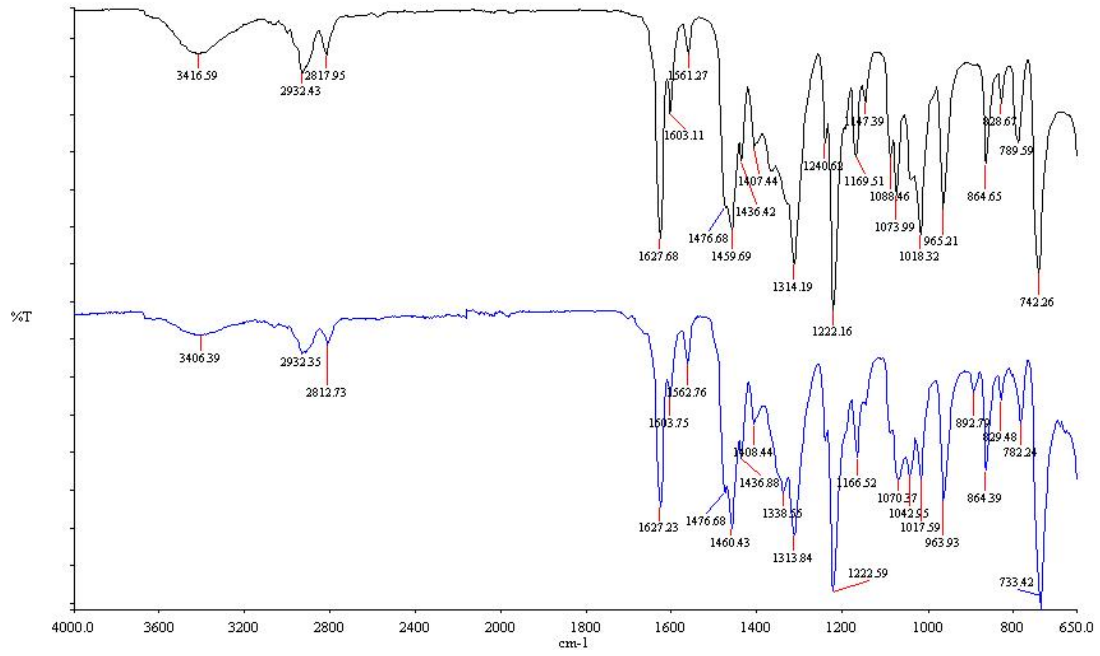

Figure 3.7: Infra-Red spectrum obtained from (top) a sample of $[Ni_7(OH)_6(L1)_6](NO_3)_2.2MeOH$ (9) and (bottom) the same sample of 9 dried under vacuum for 3 h prior to re-analysis.

Subsequent elemental analysis on this same sample analysed as the empty $[Ni_7(OH)_6(L_1)_6](NO_3)_2$ (**9**) complex. Similarly the IR spectrum of **10** gave peaks at 1337 and 1555 cm^{-1} which are characteristic for the asymmetric and symmetric NO stretching of the guest $MeNO_2$ molecules respectively. Subsequent vaccuum drying of **10** (for 2 h) resulted in the loss of these vibrational resonances indicating egress of the $MeNO_2$ guests which was also subsequently confirmed by elemental analysis. The facile removal of the MeOH and $MeNO_2$ guests in **9** and **10** respectively is consistent with their crystal structures and more specifically in the way that their host cavities are held only via weak hydrogen bonding interactions and by no means form tightly bound enclosures.

The IR spectrum of $[Ni_7(OH)_6(L_2)_6](NO)_3.2MeCN$ (**11**) exhibits a weak resonance at 2256 cm^{-1} corresponding to a CN stretch indicative of the enclosed MeCN guest

molecules. Interestingly and unlike complexes **9** and **10** this peak at 2256 cm^{-1} is not lost upon substantial vacuum drying (Figure 3.8), while no significant change is seen in its subsequent CHN microanalysis.

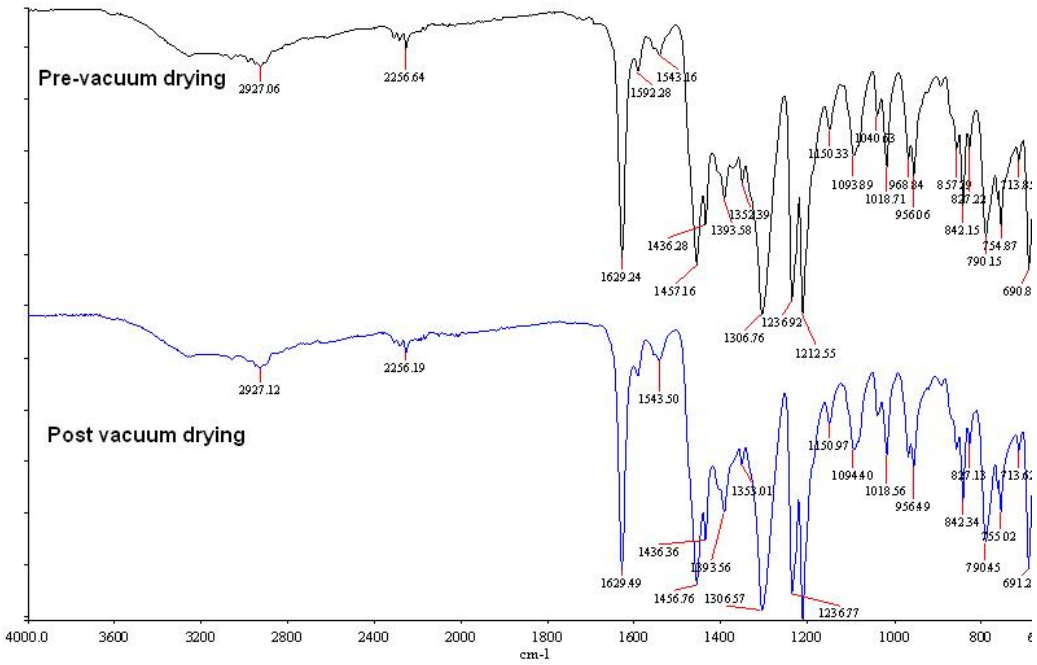

Figure 3.8: Infra-Red spectrum obtained from (top) a sample of $[Ni_7(OH)_6(L2)_6](NO_3)_2.2MeCN$ (11) and (bottom) the same sample of 11 dried under vacuum for 3 h prior to re-analysis.

This observation suggests the MeCN guests cannot readily exit the host cavities in **11**which may be attributed to its distinct (cf. **8-10**) and more tightly locked double-bowl enclosures formed via the H-bonding pendant Br-groups (vide infra).

In order to further probe potential affinities of our guest solvent molecules for their $[Ni_7]$ hosts using NMR techniques the diamagnetic $[Zn_7]$ analogues $[Zn_7(OH)_6(L_1)_6](NO_3)_2.2MeOH.H_2O$ (**12**) (Figure 3.9) and $[Zn_7(OH)_6(L_1)_6](NO_3)_2.3MeNO_2$ (**13**) (Figure 3.10) were synthesized (for crystallographic information see Table 3.3

	12	**13**
Formula	$C_{56}H_{66}N_8O_{27}Zn_7$	$C_{57}H_{66}N_{11}O_{30}Zn_7$
Formula Weight	1740.76	1842.80
Crystal system	Trigonal	Trigonal
Space group	P-3c1	P-3c1
a / Å	13.902(2)	14.082(2)
b / Å	13.902(2)	14.082(2)
c / Å	23.353(5)	22.759(5)
α, β, γ (°)	90, 90, 120	90, 90, 120
V / $Å^3$	3908.9(11)	3908.2(11)
Z	2	2
D_c (g cm^{-3})	1.479	1.566
μ (mm^{-1})	2.187	2.196
Reflections	2361	2338
Unique reflections	1766	2059
GOF on F^2	1.139	1.119
R_{int}	0.0628	0.0713
R1 [I>2σ(I)]	0.0838	0.0769
wR2 (all data)	0.1999	0.2035

Table 3.3: Crystal refinement data obtained from [Zn_7] complexes 12 and 13

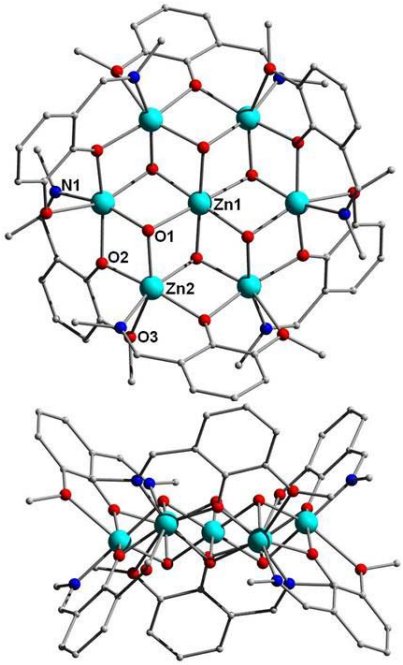

Figure 3.9: Crystal structure observed in 12 (minus MeOH guest molecules) as viewed perpendicular (top) and parallel (bottom) to the [Zn_7] plane.

The structure of $[Zn_7(OH)_6(L_1)_6](NO_3)_2.3MeNO_2$ (**13**) is analogous to that of its Ni^{II} analogue (complex **10**) with a slightly larger cavity volume of 295.4 $Å^3$;

however the connectivity in $[Zn_7(OH)_6(L_1)_6](NO_3)_2.2MeOH.H_2O$ (**12**) differs slightly to that of its counter part $[Ni_7(OH)_6(L_1)_6](NO_3)_2.2MeOH$ (**9**). The $[Zn_7]$ units in (**12**) are held in 2D layers running parallel to the *ab* plane *via* the NO_3^- anions, which sit above and below the individual heptanuclear complexes with C-H···O bonding interactions between the NO_3^- oxygen atoms (one unique, O4) and protons (one unique, H5) of the L_1^- ligands (H5···O4 = 2.46 Å). In this arrangement, each $[Zn_7]$ is H-bonded to six NO_3^- with the latter being connected to three $[Zn_7]$ units thus creating a (3,6) layer. Although the NO_3^- ions do not hold the $[Zn_7]$ moieties of neighbouring layers, the (3,6) layers stack with the $[Zn_7]$ forming columnar arrays like those found in complexes **8**, **9**, **11** and **12**, giving rise to molecular cavites (each of approximate volume ~280.4 $Å^3$ with a $[Zn_7]_{plane}$-$[Zn_7]_{plane}$ distance of 11.68 Å), formed by two juxtaposed pseudo metallocalix[6]arene $[Zn_7]$ bowl units. Those cavities are of the required size and shape to accommodate two guest MeOH and one H_2O solvent molecules. These are related crystallographically via a three fold rotation and a mirror plane.

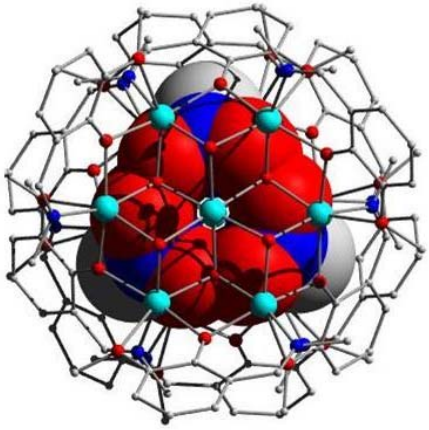

Figure 3.10: Crystal structure of 13 as viewed along a 1D column of $[Zn_7]$ units. Large space-fill spheres represent the three guest MeNO2 moieties.

By direct crystallographic comparison it becomes clear that the cavities of **8** (265.9 $Å^3$), **9** (293.7 $Å^3$), **10** (283.8 $Å^3$), **12** (280.4 $Å^3$) and **13** (295.4 $Å^3$) are very similar. The rather small differences are due to the slightly different orientations of the $[M_7]$ molecules in the crystals. From this we may draw the conclusion that the guests and / or the H-bonding with the NO_3^- do not play an important role in the resultant cavity size.

Solution studies

Despite the rather poor solubility of this class of compound UV-vis studies on MeOH and MeCN solutions of $[Ni_7(OH)_6(L_1)_6](NO_3)_2.2MeOH$ (**9**) were successfully performed (Figure 3.11).

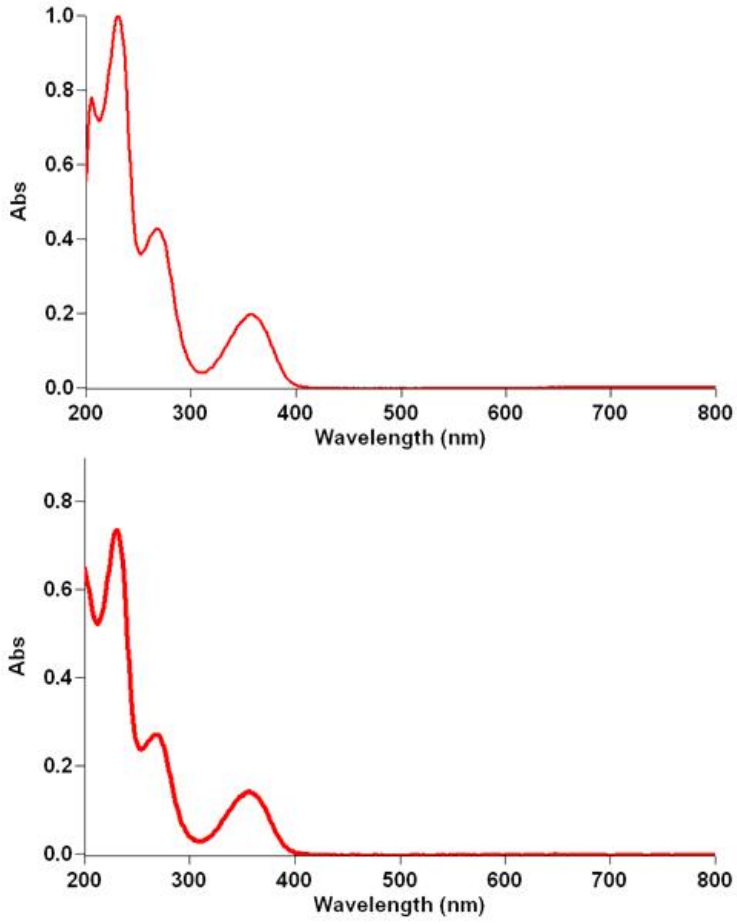

Figure 3.11: UV-vis spectra obtained from MeOH (top) and MeCN (bottom) solutions of $[Ni_7(OH)_6(L_1)_6](NO_3)_2.2MeOH$ (9).

Both solutions showed similar absorptions at approximately 230, 270 and 356 nm. A fourth sharp transition in the methanolic solution of **9** is observed at 205 nm which has been cut off in the analogous MeCN solution spectrum. The transtions at ~205,

230 and 270 nm are as a result of π→π* excitations (ε values ranging from 42.8-110.2 × 10^3 dm^3 mol^{-1} cm^{-1}), while the absorptions at 356 nm correspond to the n→π* excitations occurring in both solutions of **9**. No absorptions indicative of d-d transitions are observed and if present are presumably masked by the presence of L_1^- in **9**. This assumption is supported by the UV-vis spectra of MeOH and MeCN solutions of the Zn^{II} sibling $[Zn_7(OH)_6(L_1)_6](NO_3)_2.2MeOH.H_2O$ (**12**), whose absorptions are analogous to those observed in **9** (Figure. 3.12) with no possibility of any significant d-d transitions.

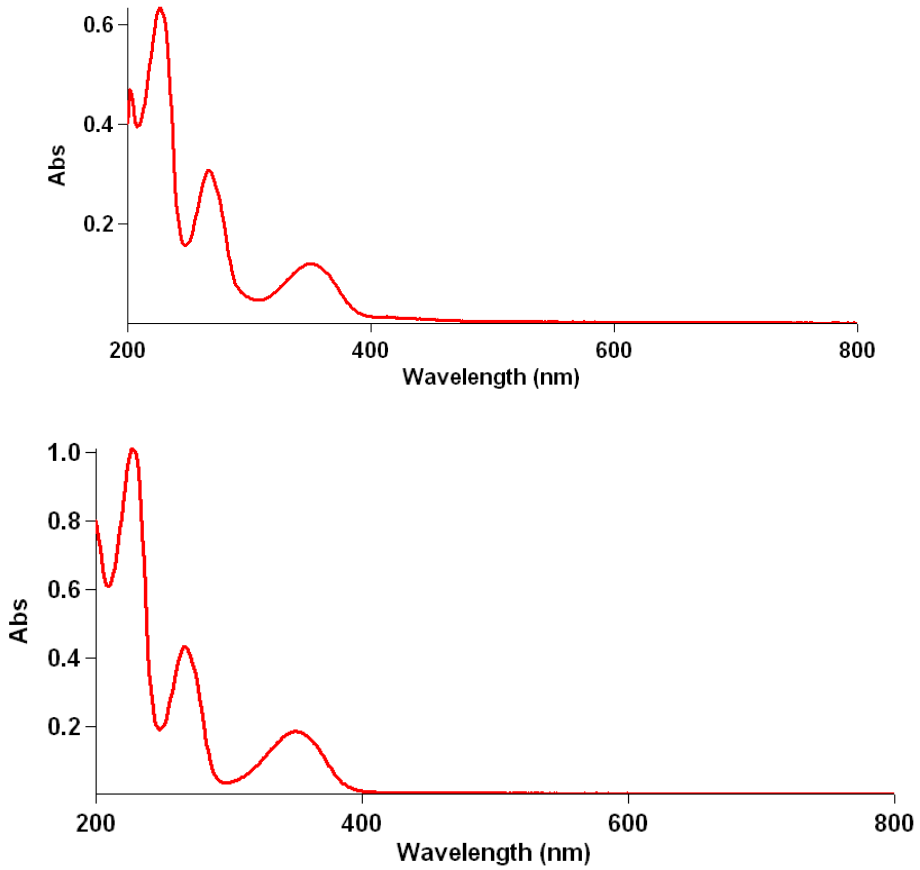

Fig. 3.12: UV-vis spectra obtained on a sample of $[Zn_7(OH)_6(L^1)_6](NO_3)_2.2MeOH.H_2O$ (12) in MeOH (top) and MeCN (bottom) solutions respectively.

Furthermore the UV-vis spectra obtained from MeOH and MeCN solution of HL_1 and HL_2 (Figure 3.11 and Figure 3.12 respectively) showed similar absorptions to those of $[Ni_7]$ (**9**) and $[Zn_7]$ (**12**), although on comparison appearing less defined presumably due to their more symmetric nature when incorporated into the $[M_7]$ complex.

Magnetic Susceptibility Studies

Magnetic susceptibility measurements were obtained on crystalline samples of $[Ni_7(OH)_6(L_1)_6](NO_3)_2$ (**8**) and $[Ni_7(OH)_6(L_2)_6](NO_3)_2.2MeCN$ (**11**) in the 300 - 5 K temperature range (Figure 3.13).

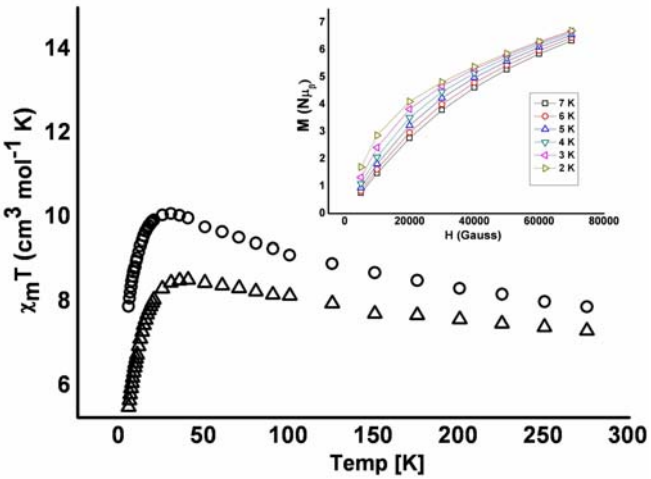

Figure. 3.13: Plot of $\chi_m T$ vs T for complex 8(Δ) and 11 (○) in the 300-5 K temperature range (measured in an applied field of 0.1 T). (Inset) Plot of M (Nμβ) vs H (G) carried out on complexes 8 in the 2-7 K temperature range and 0.5 – 7 T magnetic field range.

The room temperature $\chi_m T$ values of 7.76 and 7.90 cm^3 mol^{-1} K respectively are slightly larger than the value expected for seven non interacting Ni^{II} ions (~ 7.7 cm^3 mol^{-1} K assuming g = ~2.1). As the temperature is decreased the values of $\chi_M T$ increase slowly, reaching maximum values of ~8.5 cm^3 K mol^{-1} at 40 K for **8** and ~10 cm^3 K mol^{-1} at 25 K for **11**, before decreasing below these temperatures to minimum values at 5 K of ~5.5 cm^3 K mol^{-1} (**1**) and ~7.9 cm^3 K mol^{-1} (**11**). This behaviour is suggestive of very weak ferro- or ferrimagnetic intra-molecular exchange between the Ni^{II} ions in both complexes, with their low temperature (T < 40 K) decreases in $\chi_m T$ ascribed to relatively strong inter-molecular antiferromagnetic exchange, consistent with the extensive H-bonding observed in the crystals of **8** and **11**. The maxima in $\chi_m T$ for **8** and **11** are well below that expected for an isolated S = 7 spin ground state which would give a $\chi_m T$ value of approximately 31 cm^3 K mol^{-1} (assuming g = 2.10). Fitting of the $1/\chi_m$ versus T data to the Curie-Weiss law using only the 300-50 K data

affords Weiss constants (Θ) of +18.7 K (**8**) and +29.0 K (**11**) (Figure 3.14), suggestive of weak ferromagnetic exchange.

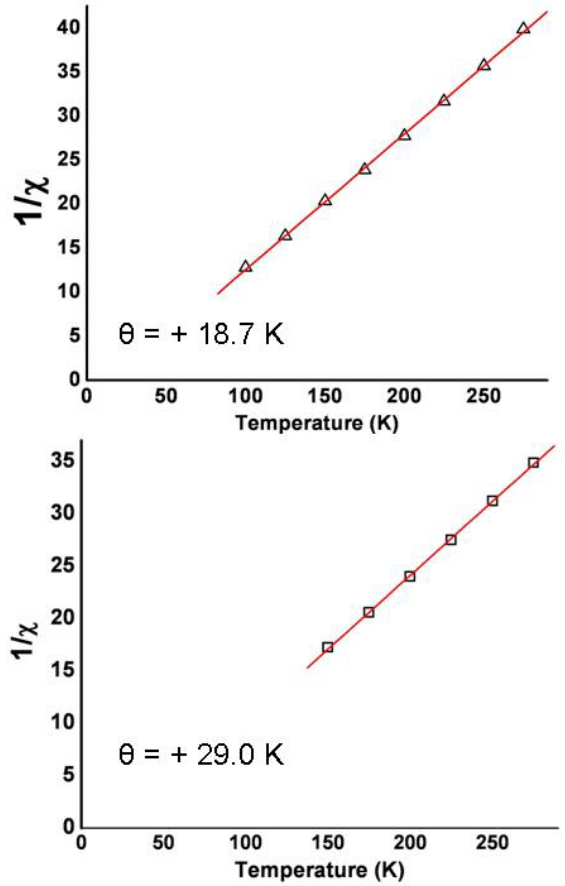

Figure 3.14: Plots of 1/χ vs. T obtained from complexes 8 (top) and 11 (bottom) giving Curie-Weiss constants (θ) of +18.7 and +29.0 K respectively.

Several factors proclude the fitting or simulation of the susceptibility data: a) the presence of numerous different exchange interactions; b) the presence of relatively strong intermolecular interactions; c) the weak exchange between the metal centres and the likelihood that *J* will be comparable to the single ion zfs (weak exchange limit) and thus the presence of multiple low lying states that cannot properly be described as total *S* states. This scenario is supported by the magnetisation versus field data carried out in the 2 – 7 K temperature and 0.5 – 7.0 T magnetic field ranges (Figure 3.13 (above) (**8**) and Figure 3.15 (**11**)).

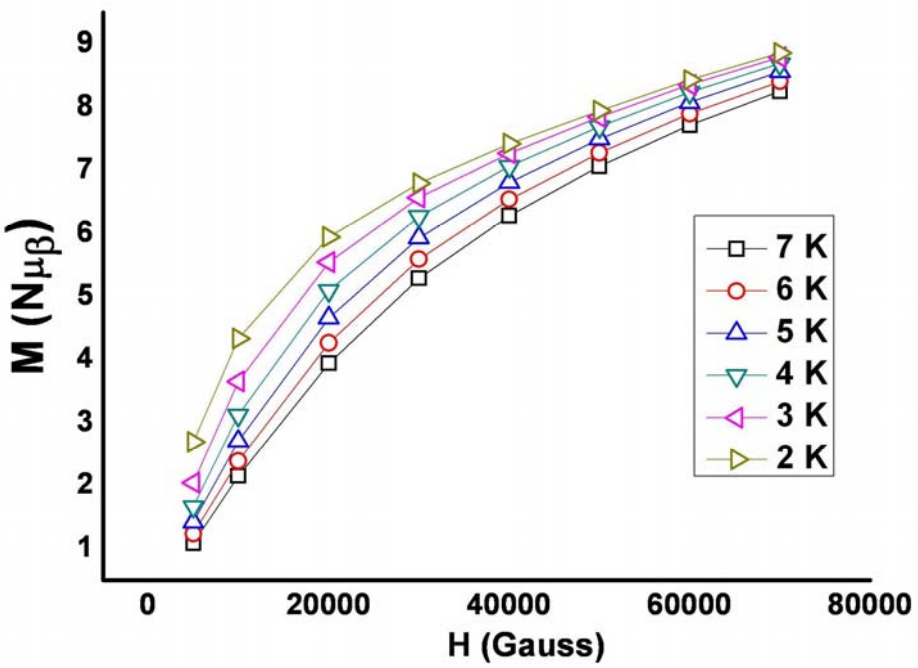

Figure 3.15: Plots of magnetisation (M/ Nμ$_B$) vs. H (G) obtained from complex 10 in the 2-7 K temperature range and fields of 0.5- 7 T.

For an isolated spin ground state one would expect a rapid initial increase in *M*, with saturation of the magnetisation achieved for relatively low fields. However for both **8** and **11** *M* increases only slowly with *H*, indicative of the population of low lying levels with smaller magnetic moment, which only become depopulated with the application of larger fields. Our ability to make the analogous Zn^{II} complexes will therefore prove important for future studies. Doping experiments in which we make highly diluted [Ni_7] clusters in [Zn_7] matrices and study their behaviour by both SQUID magnetometry and EPR spectroscopy are currently in progress and will reported later.

Conclusions

This work haa reported the syntheses, structures and solid and solution state characterisation of a family of [Ni_7] and [Zn_7] planar hexagonal disc complexes. This family may also be described as *pseudo* metallocalix[6]arene complexes due to their double-bowl topologies which have shown to act as host cavities accommodating numerous guest solvent molecules. The magnetic behaviour of the Ni^{II} discs is complicated by the presence of relatively strong intermolecular interactions and the weak intramolecular exchange and thus the isolation of the diamagnetic Zn^{II} analogues and the examination of the diluted [Ni_7] discs promises to afford much useful information.

Further progress of the work will include the functionalisation of the ligands HL_1 and HL_2 at their upper rim positions (R group in Scheme 1) in order to a) preferentially attract specific guest species and b) increase their solubility towards future ^{1}H NMR host-guest titration studies. Solid state NMR studies will also be investigated. [19]

Experimental Section

Infra-red spectra were recorded on a Perkin Elmer FT-IR *Spectrum One* spectrometer equipped with a Universal ATR Sampling accessory (NUI Galway). UV-visible studies were carried out on a Cary *100 Scan* (Varian) spectrophotometer.
Elemental analysis was carried out by Patrick McNaughton of the School of Chemistry microanalysis service at NUI Galway. Variable-temperature, solid-state direct current (dc) magnetic susceptibility data down to 1.8 K were collected on a Quantum Design MPMS-XL SQUID magnetometer equipped with a 7 T dc magnet. Diamagnetic corrections were applied to the observed paramagnetic susceptibilities using Pascal's constants.

Syntheses

All reactions were performed under aerobic conditions and all reagents and solvents were used as purchased.

Synthesis of $[Ni_7(\mu_3\text{-}OH)_6(L_1)_6](NO_3)_2$ (8)

$Ni(NO_3)_2.6H_2O$ (0.25 g, 0.85 mmol), HL_1 (0.14 g, 0.85 mmol) and NaOH (0.034 g, 0.85 mmol) were dissolved in 30 cm^3 EtOH and stirred for 4 h. The resultant green solution was then filtered and allowed to stand. X-ray quality crystals of **1** were obtained in 30% yield upon slow evaporation. Elemental analysis calculated (%) for $C_{54}H_{66}N_8O_{24}Ni_7$ (1): C, 39.98; H, 4.10; N, 6.91; Found: C, 40.44; H, 4.91; N, 7.02. FT-IR (cm^{-1}): 3415 (w), 2968 (w), 2932 (w), 1627 (s), 1602 (w), 1559 (w), 1459 (m), 1406 (w), 1315 (s), 1221 (s), 1171 (w), 1148 (w), 1072 (m), 1044 (w), 1018 (w), 963 (m), 864 (m), 828 (w), 793 (m), 743 (s).

$[Ni_7(OH)_6(L_1)_6](NO_3)_2$.2MeOH (9)

$Ni(NO_3)_2.6H_2O$ (0.25 g, 0.86 mmol), HL_1 (0.145 g, 0.86 mmol) and NaOH (0.04 g, 1.00 mmol) were dissolved in 30 cm^3 MeOH and stirred for 3 h. The resultant green solution was then filtered and allowed to stand. X-ray quality hexagonal crystals of **2** were obtained in 40% yield upon slow evaporation of the mother liquor. Elemental analysis on 'wet' sample of **2** calculated (%) for $C_{56}H_{74}N_8O_{26}Ni_7$ (**2**.2MeOH): C, 39.95; H, 4.10; N, 6.90; Found: C, 40.44; H, 4.91; N, 7.02. Elemental analysis on vaccuum dried sample of **2** calculated (%) as $C_{54}H_{66}N_8O_{24}Ni_7$ (**2**): C, 39.99; H, 4.10; N, 6.91; Found: C, 39.63; H, 4.37; N, 6.15. FT-IR (cm^{-1}): 3402 (b), 2932 (w), 2817 (w), 1627 (s), 1603 (w), 1561 (w), 1459 (m), 1436(m), 1407 (w), 1338(m), 1314 (s), 1240(w), 1222 (s), 1169 (w), 1147 (w), 1073 (m), 1042 (w), 1018 (w), 965 (m), 864 (m), 828 (w), 789 (m), 741 (s). UV/vis (MeOH): λ_{max} [nm] (ε_{max} 10^3 dm^3 mol^{-1} cm^{-1}): 205 (84.6), 231 (108.5), 268 (46.3), 356 (21.4). (MeCN): λ_{max} [nm] (ε_{max} 10^3 dm^3 mol^{-1} cm^{-1}): 230 (110.2), 268 (42.8), 356 (15.8).

$[Ni_7(\mu_3\text{-}OH)_6(L_2)_6](NO_3)_2$.3$MeNO_2$ (10)

The reaction mixture obtained from **1** was filtered and the filtrate left to evaporate to dryness. The resultant green solid was then redissolved in 10 cm^3 $MeNO_2$ wherby green hexagonal crystals of **3** were obtained in 10% yield upon slow Et_2O diffusion. Elemental analysis calculated (%) for $C_{57}H_{75}N_{11}O_{30}Ni_7$ (**3**.3$MeNO_2$): C, 37.93; H, 4.19; N, 8.54; Found: C, 38.31; H, 4.59; N, 8.29. FT-IR (cm^{-1}): 3625(w), 2931(w), 1628(s),

1601(m), 1555(s), 1476(s), 1460(s), 1433(m), 1407(m), 1337(m), 1316(m), 1221(m), 1171(w), 1147(w), 1086(w), 1072(w), 1018(w), 865(w), 795(w), 743(w).

$[Ni_7(\mu_3\text{-}OH)_6(L_2)_6](NO_3)_2.2MeCN$ (11)

$Ni(NO_3)_2.6H_2O$ (0.25 g, 0.85 mmol), HL_2 (0.21 g, 0.85 mmol) and NaOH (0.034 g, 0.85 mmol) were dissolved in 30 cm^3

EtOH and stirred for 4 h. The resultant green precipitous solution was then filtered and evaporated to dryness. The green solid was then redissolved in MeCN and from which crystals of **4** were obtained upon Et_2O diffusion in 23% yield. Elemental analysis calculated (%) for $C_{58}H_{66}N_{10}O_{24}Br_6Ni_7$ (**4.**2MeCN): C, 31.99; H, 3.06; N, 6.43; Found: C, 31.38; H, 3.34; N, 6.64. FT-IR (cm^{-1}): 3620(w), 3261(wb), 2927(w), 2256(w), 1629(s), 1592(w), 1543(w), 1457(m), 1457(m), 1393(m), 1352(m), 1306(s), 1236(m), 1212(m), 1150(w), 1093(w), 1040(w), 1018(w), 968(w), 956(w), 857(w), 842(w), 827(w), 790(w), 754(w), 713(w), 690(w).

$[Zn_7(OH)_6(L_1)_6)(NO_3)_2.2MeOH.1H_2O$ (12)

$Zn(NO_3)_2.6H_2O$ (0.25 g, 0.85 mmol), HL_1 (0.14 g, 0.85 mmol) and NaOH (0.034 g, 0.85 mmol) were dissolved in 30 cm^3 MeOH and stirred for 2 h. The resultant yellow solution was then filtered and X-ray quality crystals of **5** were obtained in 35% upon slow evaporation. Elemental analysis calculated (%) for $C_{56}H_{74}N_8O_{26}Zn_7$ (**5**): C, 38.81; H, 4.30; N, 6.47; Found: C, 38.87; H, 4.65; N, 6.61. FT-IR (cm^{-1}): 3406 (b), 2931 (w), 2823(w), 1636 (s), 1602 (w), 1561 (w), 1459 (m), 1408 (w), 1368(m), 1330(m), 1308 (s), 1221 (s), 1173 (w), 1148 (w), 1093 (m), 1077 (w), 1013 (w), 967 (m), 860 (m), 828 (w), 793 (m), 743 (s). UV/vis (MeOH): λ_{max} [nm] (ε_{max} 10^3 dm^3 mol^{-1} cm^{-1}): 202 (108.3), 226.9 (146.4), 267 (71.1), 350 (27.9). (MeCN): λ_{max} [nm] (ε_{max} 10^3 dm^3 mol^{-1} cm^{-1}): 227 (242.6), 267 (103.6), 350 (44.0).

$[Zn_7(\mu_3\text{-}OH)_6(L_1)_6](NO_3)_2.3MeNO_2$ (13)

$Zn(NO_3)_2.6H_2O$ (0.25 g, 0.85 mmol), HL_1 (0.14 g, 0.85 mmol) and NaOH (0.034 g, 0.85 mmol) were dissolved in 30 cm^3 EtOH and stirred for 3 h. The resultant yellow solution was then filtered and evaporated to dryness. The resultant solid

was then redissolved in $MeNO_2$ from which X-ray quality crystals of **6** were obtained in ~ 10%. Elemental analysis calculated (%) for $C_{57}H_{75}N_{11}O_{30}Zn_7$ (**6**): C, 36.97; H, 4.08; N, 8.32; Found: C, 37.02; H, 4.17; N, 8.44. FT-IR (cm^{-1}): 3418 (w), 2967 (w), 2930 (w), 1625 (s), 1601 (w), 1561 (w), 1459 (m), 1405 (w), 1319 (s), 1220 (s), 1168 (w), 1149 (w), 1072 (m), 1041 (w), 1016 (w), 960 (m), 860 (m), 829 (w), 789 (m), 743 (s).

References

1. J. O. Magrans, A. R. Ortiz, M. A. Molins, P. H. P. Lebouille, J. Sanchez-Quesada, P. Prados, M. Pons, F. Gago and J. de Mendoza. *Angew. Chem. Int. Ed.*, 1996, **35**, 1712.

2. (a) J. L. Atwood, K. T. Holman and J. W. Steed. *Chem. Commun*., 1996, 1401-1407. (b) P. D. Beer. *Chem. Commun.*, 1996, 659-696. (c) P. A. Gale, J. L. Sessler and V. Krail. *Chem. Commun*., 1998, 1-8.

3. S. J. Dalgarno, P. K. Thallapally, L. J. Barbour and J. L. Atwood. *Chem. Soc. Rev.*, 2007, **36**, 236.

4. (a) W. Yang and M. M. De Villiers. *Eur. J. Pharm. Biopharm*., 2004, 58, 629. (b) W. Yang and M. M. De Villiers. *J. Pharm. Pharmacol.*, 2004, 56, 703-708. (c) W. Yang and M. M. De Villiers. *AAPS J*., 2005, **7**, E241—E248.

5. For examples see : (a) T. Heinz, D. M. Rudkevich and J. Rebek Jr., *Nature*., 1998, **394**, 764-766. (b) M. D. Pluth and K. N. Raymond. *Chem. Soc. Rev*., 2007, **36**, 161-171 and references herein. (c) P. Restorp, O. B. Berryman, A. C. Sather, D. Ajami amd J. Rebek Jr., *Chem. Commun.,* 2009, 5692-5694.

6. (a) O. D. Fox, N. K. Dalley and R. G. Harrison., *Inorg. Chem*., 1999, **38**, 5860-5863. (b) R. G. Harrison, J. L. Burrows and L. D. Hansen., *Chem. Eur. J*., 2005, **11**, 5881-5888. (c) E. Pardo, K. Bernot, F. Lloret, M. Julve, R. Ruiz-Garcia, J. Pasan, C. Ruiz-Perez, D. Cangusso, V. Costa, R. Lescouezec and Y. Journaux., *Eur. J. Inorg. Chem.*, 2007, 4569-4575. (d) O. D. Fox, J. Cookson, E. J. B. Wilkinson, M. G. B. Drew, E. J. MacLean, S. J. Teat and P. D. Beer., *J. Am. Chem. Soc*., 2006, **128**, 6990-7002. (e) I. Imaz, J. Hemando, D. Ruiz-Molina and D. Maspoch., *Angew. Chem. Int.*

Ed., 2009, **48**, 2325-2329. (e) M. Yoshizawa, J. K. Klosterman and M. Fujita, *Angew. Chem. Int. Ed.,* 2009, **48**, 3418-3438 and references herein.

7. G. Karotsis, S. J. Teat, W. Wernsdorfer, S. Piligkos, S. J. Dalgarno and E. K. Brechin., *Angew. Chem. Int. Ed.*, 2009, **48**, 8285-8288.

8. G. Karotsis, M. Evangelisti, S. J. Dalgarno and E. K. Brechin., *Angew. Chem. Int. Ed.,* 2009, 48, 9928.

9. J. W. Steed and J. L. Atwood. *Supramolecular Chemistry* (Wiley). 2000.

10. J. W. Steed and J. L. Atwood. *Supramolecular Chemistry* (Wiley). 2000.

11. S. T. Meally, G. Karotsis, E. K. Brechin, G. S. Papaefstathiou, P. W. Dunne, P. McArdle, and L. F. Jones. *CrystEngComm*., 2010, DOI: 10.1039/b914538a.

12. (a) T. C. Stamatatos, K. M. Poole, D. Fouget-Alblol, K. A. Abboud, T. A. O`Brien and G. Christou, *Inorg. Chem.,* 2008, **47**, 6593. (b) N. C. Harden, M. A. Bolcar, W. Wernsdorfer, K. A. Abboud, W. E. Streib and G. Christou, *Inorg. Chem.,* 2003, **42**, 7067. (c) M. A. Bolcar, S. M. J. Aubin, K. Folting, D. N Hendrickson and G. Christou, *J. Chem. Soc., Chem. Commun.* 1997, 1485. (d) B. Pilawa, M. T. Kelemen, S. Wanka, A. Geisselmann and A. L. Barra, *Europhys. Lett*. 1998, **43**, 7. (e) T. C. Stamatatos, K. M. Poole, D. Foguet-Albiol, K. A. Abboud, T. E. O`Brien and G. Christou., *Inorg. Chem*., 2008, **47**, 6593.

13. H. Oshio, N. Hoshino, T. Ito, M. Nakano, F. Renz and H. Gütlich, *Angew. Chem. Int. Ed.,* 2003, **42**, 223.

14. S.-H. Zhang, Y. Song, H. Liang and M.-H. Zeng, *CrystEngComm.*, 2009, **11**, 865.

15. L. J. Barbour, MCAVITY: Program for calculating the molecular volume of closed capsules, University of Missouri-Columbia, Columbia, MO, USA, 2003, http://www.x-seed.net/cavity.html. The free volume within the cavities of **1-4** was calculated in the absence of guests.

16. http://www.topos.ssu.samara.ru; V. A. Blatov, *IUCr CompComm Newsletter*, 2006, **7**, 4.

17. M. O'Keeffe, M. A. Peskov, S. J. Ramsden, O. M. Yaghi, *Acc. Chem. Res.,* 2008, **41,** 1782.

18. (a) M. A. Halcrow, J.-S. Sun, J. C. Hoffman and G. Christou., *Inorg. Chem*., 1995, **34**, 4167-4177 and references herein.

Chapter 4: Polymetallic clusters of manganese with N,N Bis(2-hydroxyethyl)ethylenediamine (heedH_2)

Introduction

The specific design and synthesis of *tetranuclear* Mn clusters, although of interest from a spin frustration perspective, has mainly been pursued in order to make models for the complex responsible for the oxidation of water in the oxygen evolving centre (OEC) of Photosystem II (PSII) in green plants and cyanobacteria.[1,2] Recent crystallographic[3] and polarised EXAFS studies[4] on the PSII reaction centre of *Thermosynechococcus elongatus* confirm the cluster to be an oxide-bridged [Mn_4Ca] complex with (mainly) peripheral carboxylate ligation.

The most common [Mn_4] complexes in the literature possess [Mn_4O_2] 'butterfly' cores which are best described as consisting of two fused or vertex-sharing [$Mn_3(\mu_3\text{-}O)$] triangles (Figure 4.1).[5] Less common is the [Mn_4O_4] cubane topology where the Mn centres occupy the four alternate corners of a cube (Fig. 4.1);[6] and less common still are those with a linear zig-zag arrangement which may take either a *cis* or (much rarer) *trans* conformation (Figure 4.2).[7]

For some years the Brechin group have been building SMMs with tripodal alcohol ligands of general formula R-C(CH_2OH)$_3$ (where R = H, CH_3, Et *etc*) and their many derivatives (Scheme 4.1).[8] A natural extension to these studies is the investigation of the coordination chemistry of analogous organic molecules in which one (or more) of the alcohol 'arms' is replaced by an alternative functional group(s), for example an amine group. While each alkoxide arm has the potential to bridge up to three metals (and thus a maximum of seven metals per tripodal ligand), the -NH_2 'arm' is likely, if bonded, to act solely as a monodentate/terminal capping unit and should give rise to a number of related, yet different, structural topologies.[8] We herein report our initial investigations into the reactivity of N,N-Bis(2-hydroxyethyl)ethylenediamine (heedH_2); a relatively unexplored ligand whose coordination chemistry is thus far restricted to the

dimeric complexes $[Cu_2(heedH)_2](PF_6)_2$[9] and $[Zn_2(\mu_2\text{-}O)(heedH_2)](BF_4)_2$.[10]

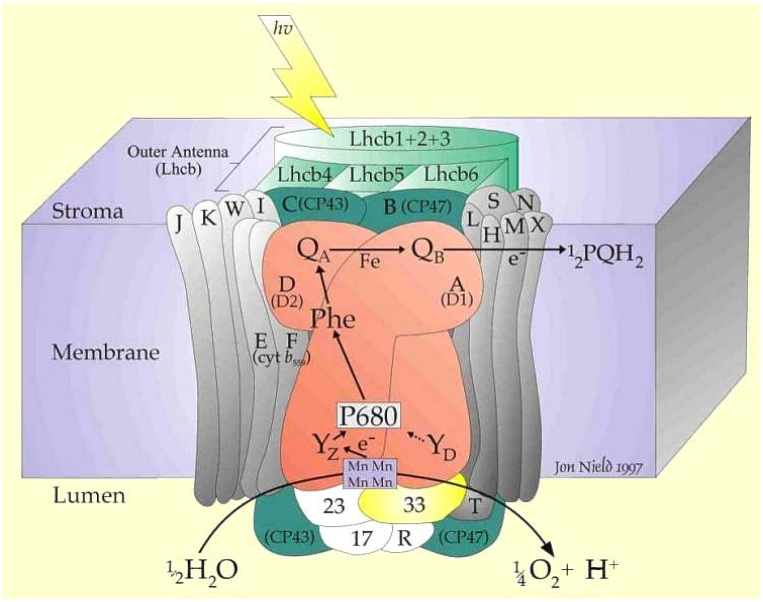

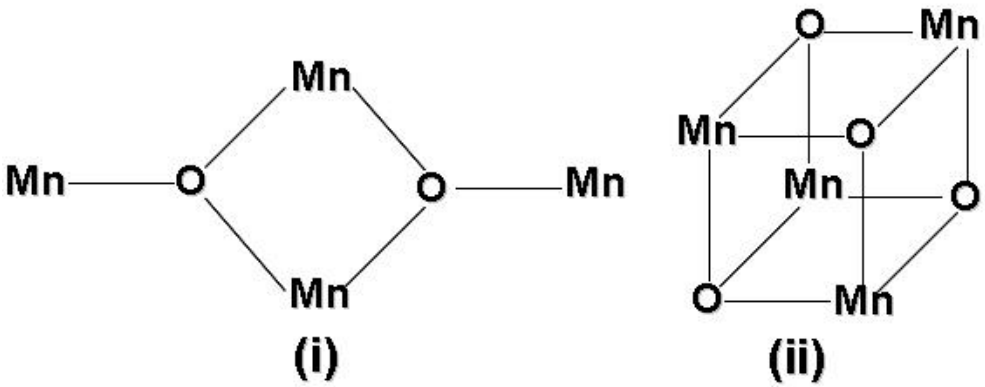

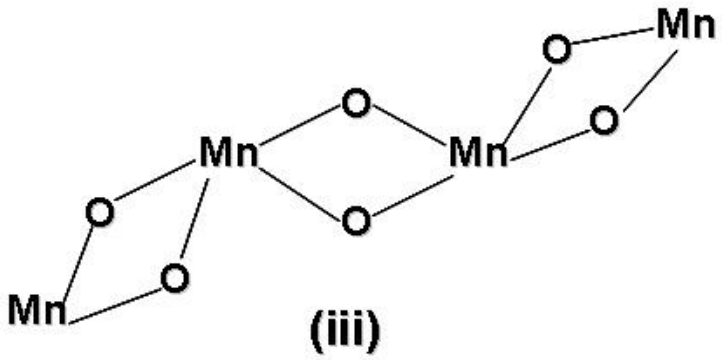

Figure 4.1: Schematic representation of PSII (top) and the common tetranuclear $[Mn_4O_2]$ 'butterfly' (i); $[M_4O_4]$ cubane (ii) and linear trans zig-zag (iii) topologies.

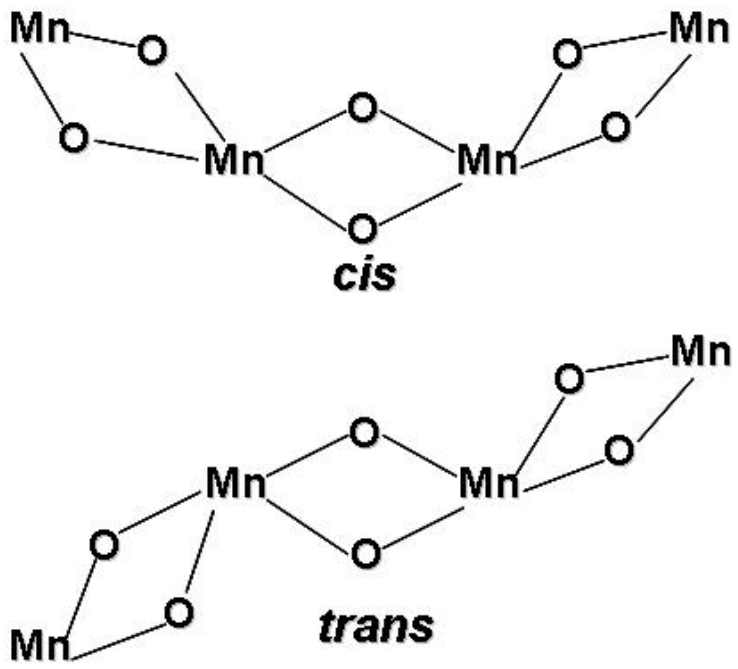

Figure 4.2: Schematic illustrating the *cis* and *trans* structural conformers of tetranuclear Mn - complexes with a linear $[Mn_4O_6]$ core.

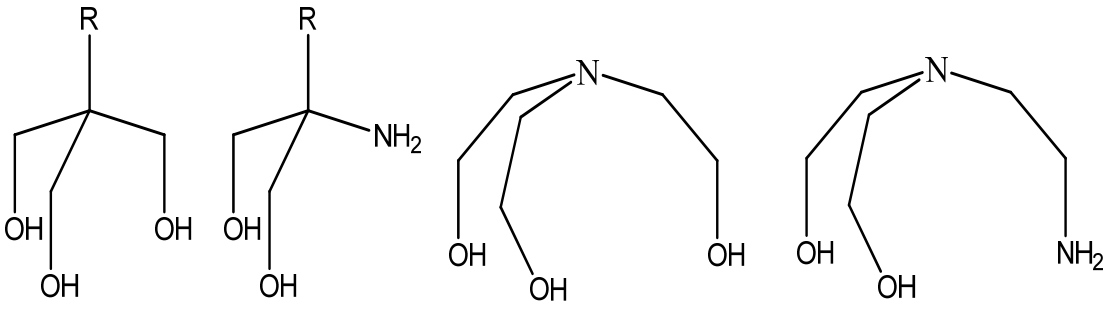

Scheme 4.1. (from left to right) Structures of R-$C(C_2H_4OH)_3$ (R=CH_3, H_3thme; R = CH_3CH_2, H_3tmp); R-$C(CH_2OH)_2NH_2$ (R = CH_3, ($ampH_2$); R = CH_3CH_2, ($aepH_2$); triethanolamine (H_3tea); and $heedH_2$.

Reaction of $Mn^{II}X_2$ salts (X = Br, Cl, ClO_4) in the presence of the tripodal ligand $heedH_2$ in suitable solvents (MeOH, EtOH or MeCN) has produced the family of tetranuclear mixed valent Mn complexes: $[Mn^{II}_2Mn^{IV}_2O_2(heed)_2(EtOH)_6Br_2]Br_2$ (**14**), $[Mn^{II}_2Mn^{IV}_2O_2(heed)_2(H_2O)_2Cl_4]$ (**15**),

$[Mn^{II}_2Mn^{IV}_2O_2(heed)_2(heedH_2)_2](ClO_4)_4$ (**16**),
$[Mn^{II}_2Mn^{IV}_2O_2(heed)_2(MeCN)_2(H_2O)_2(bpy)_2](ClO_4)_4$ (**17**),
$[Mn^{II}_2Mn^{IV}_2O_2(heed)_2(bpy)_2Br_4]$ (**18**); and the 2-D network of tetranuclear $Mn^{II/IV}$ clusters $\{[Mn^{II}_2Mn^{IV}_2O_2(heed)_2(H_2O)_2(MeOH)_2(dca)_2]Br_2\}_n$ (**19**). This family represents only the third example of Mn complexes exhibiting the linear zig-zag *trans* topology first seen in the compounds $[Mn^{IV}_4O_6(bipy)_6](ClO_4)_4$[11] and $[Mn^{II}_4(H_2L3)_2(OAc)_2(py)_5]$ (where H_2L3 = 2-hydroxy-1,3-bis[3-(2-hydroxyphenyl)-3-oxopropionyl]benzene)[12] and are the first to exhibit a $[Mn^{II}_2Mn^{IV}_2]$ mixed-valent charge distribution. **14-19** are isostructural, comprising identical $\{Mn_4O_6\}$ cores and differ only in their terminal ligation at the peripheral Mn^{II} sites. For this reason we will restrict our discussion to complex **14**, highlighting any differences. Crystallographic data are collected in Table 1 with a complete list of bond lengths and angles in the Appendix.

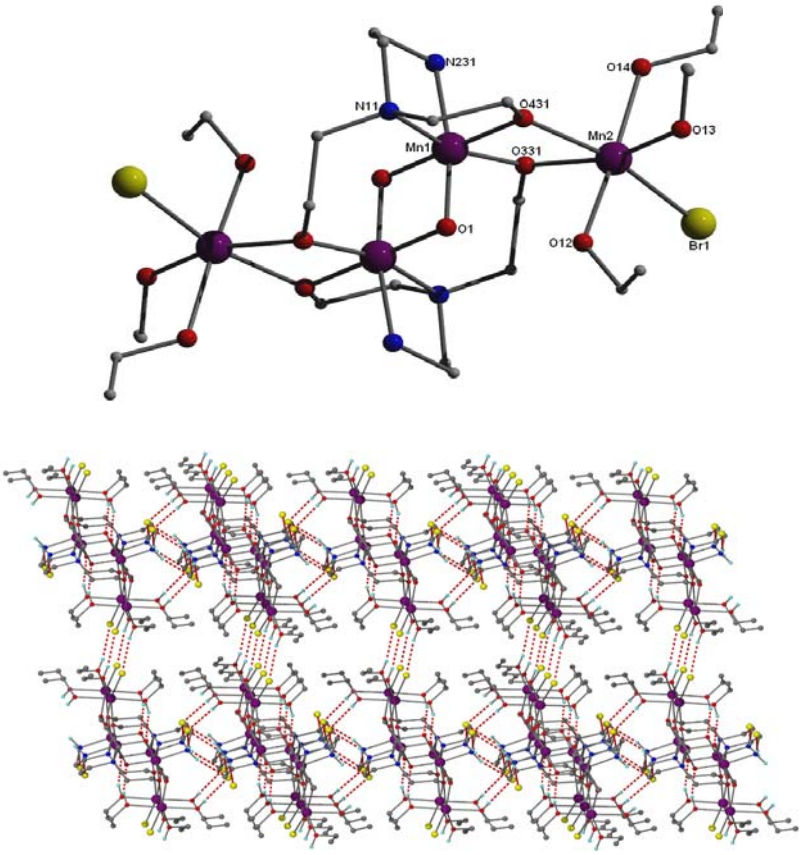

Figure 4.3. Molecular structure of $[Mn_4O_2(heed)_2(EtOH)_6Br_2]Br_2$ (14, top). H-atoms and Br^- counter anions omitted for clarity. Selected bond lengths (Å): Mn1-O1 = 1.816(2), Mn1 – N11 = 2.089(2), Mn1-N231 = 2.053(2), Mn2-Br1 = 2.5716(5), Mn2-O331 = 2.189(2), Mn2-O431 = 2.142(2). The packing of the layers in 14 demonstrating the brickwall arrangement of the $[Mn_4]$ clusters (bottom). Colour code: Mn = purple, O = red, N = blue, C = grey, Br = yellow.

Table 4.1 Crystallography data obtained for 14-19

	14	**15·2EtOH·H_2O**	**16**	**17**	**18·2MeOH**	**19**
fomula[a]	$C_{24}H_{64}N_4O_{12}Br_4Mn_4$	$C_{12}H_{32}N_4O_8Cl_4Mn_4$	$C_{24}H_{60}N_8O_{26}Cl_4Mn_4$	$C_{36}H_{54}N_{10}O_{24}Cl_4Mn_4$	$C_{34}H_{52}N_8O_8Br_4Mn_4$	$C_{10}H_{24}N_5O_6Br_1Mn_2$
fw (g mol $^{-1}$)	1140.12	1112.48	1238.30	1431.46	1240.16	500.09
Crystal System	Monoclinic	Trigonal	Monoclinic	Triclinic	Triclinic	Monoclinic
space group	P 1 21/c 1	R-3	P 1 21/c 1	P -1	P -1	P 1 21/c 1
a (Å)	13.6721(3)	23.5608(3)	11.1558(10)	9.8751(3)	9.1916(3)	14.6719(4)
b (Å)	9.1130(2)	23.5608(3)	10.9531(10)	13.9986(4)	9.4296(3)	10.8780(3)
c (Å)	17.2367(4)	15.5896(6)	18.8477(10)	14.1558(4)	14.1811(5)	14.9952(4)
α (deg)	90	90	90	63.722(2)	103.468(2)	90
β (deg)	99.485	90	100.282(10)	73.229(2)	90.430(2)	113.4910(10)
γ (deg)	90	120	90	78.714(2)	111.896(2)	90
V (Å^3)	2118.23(8)	7494.6(3)	2266.0(3)	1674.73(9)	1103.01(7)	2194.90(10)
Z	2	9	2	1	1	4
ρ_{calcd} (g cm^{-3})	1.787	1.497	1.815	1.361	1.867	1.51
T (K)	150	150	150	150	150	150
λ (Å)	0.7103	0.71073	0.71073	0.71073	0.71073	0.71073
μ (mm^{-1})	4.991	1.854	1.422	0.973	4.798	3.000
Measd/indep (R_{int}) reflns	**25247/5196(0.043)**	33942/4268 (0.025)	55249/ 13087(0.039)	21077/ 9231(0.043)	24353/6465(0.036)	26611/5814(0.033)
Obsd reflns [I>4σ (*I*)]	**3655**	3261	11011	6997	5134	4369
*R*1[b]	**0.0308**	0.0378	0.0460	0.0701	0.0317	0.0483
*wR*2[c]	**0.0699**	0.1062	0.1000	0.1755	0.0800	0.1389
GOF on F^2	**0.7442**	0.9935	0.9051	0.9925	0.9266	0.9159
Δ $\rho_{max,min,}$ e Å^{-3}	1.23-0.91	1.04-0.53	1.46-1.54	1.22-0.94	1.05-0.93	3.27-0.57

Table 4.2 Bond lengths (Å) and angles (°) for 14-19.

14		**15**		**16**	
Mn1-O1	1.8158(18)	Mn1-N11	2.097(2)	Mn1-O422	2.0949(14)
Mn1-N11	2.089(2)	Mn1-O12′	1.8384(18)	Mn1-O412′	2.2294(14)
Mn1-N231	2.053(2)	Mn1-N21	2.049(2)	Mn1-O411	2.1815(17)
Mn1-O431	1.9134(18)	Mn1-O41	1.8978(18)	Mn1-O421	2.2005(16)
Mn1-O331′	1.8719(18)	Mn1-O61	1.8796(17)	Mn1-N11	2.3987(19)
Mn1- O1′	1.8280(17)	Mn1-O12	1.8186(17)	Mn1-N431	2.212(2)
Mn2-O13	2.188(2)	Mn2-O41	2.1470(18)	Mn2-O1	1.8149(13)
Mn2-O14	2.2196(19)	Mn2-O61	2.1659(18)	Mn2-O1′	1.8209(14)
Mn2-O12	2.221(2)	Mn2-C113	2.3929(8)	Mn2-O422	1.9131(14)
Mn2-Br1	2.5716(5)	Mn2-C114	2.4364(8)	Mn2-O412′	1.8681(14)
Mn2′-O431	2.1421(19)	Mn2-O15	2.090(2)	Mn2-N12	2.0987(17)
Mn2-O331	2.1877(18)			Mn2-N432	2.0556(18)
Mn1′-O1-Mn1	96.18(8)	Mn2-O61-Mn1	103.96(8)	Mn2′-O1-Mn2	95.95(6)
Mn1′-O331-Mn2	102.51(8)	Mn1′-O12-Mn1	96.89(8)	Mn1′-O412-Mn2′	101.42(6)
Mn2′-O431-Mn1	102.79(8)	Mn2-O41-Mn1	104.04(8)	Mn1-O422-Mn2	104.90(6)

17		**18**		**19**	
Mn1-O9′	1.882(3)	Mn1-O23′	1.8667(16)	Mn1-O13′	1.819(2)
Mn1-O6	1.912(3)	Mn1-O27′	1.8070(16)	Mn1-O6	1.905(2)
Mn1-O29′	1.831(2)	Mn1-O20	1.9211(17)	Mn1-O9	1.865(2)
Mn1-O29	1.817(2)	Mn1-O27	1.8212(16)	Mn1-O13	1.820(2)
Mn1-N3	2.089(3)	Mn1-N17′	2.100(2)	Mn1-N3	2.093(3)
Mn1-N12	2.047(3)	Mn1-N26	2.068(2)	Mn1-N12	2.071(3)
Mn2-O28	2.201(3)	Mn2-Br3	2.6723(4)	Mn2-O14	2.215(3)
Mn2-N14	2.236(3)	Mn2-Br4	2.6372(4)	Mn2-O16	2.211(3)
Mn2-N24	2.236(3)	Mn2′-N10	2.254(2)	Mn2-N23	2.148(4)
Mn2-N25	2.211(4)	Mn2-N12	2.278(2)	Mn2-N18	2.161(4)
Mn2-N25	2.211(4)	Mn2-N12	2.278(2)	Mn2-N18	2.161(4)
Mn1′-O29-Mn1	96.15(11)	Mn1-O27-Mn1′	96.15(7)	Mn1-O13-Mn1′	96.44(11)
Mn2-O6-Mn1	102.86(12)	Mn2-O20-Mn1	105.66(7)	Mn2-O6-Mn1	104.13(11)
Mn2′-O9-Mn1′	101.42(12)	Mn2′-O23-Mn1′	102.54(7)	Mn2-O9-Mn1	102.36(10)

Table 4.3. Bond Valence Sum calculations for complexes 14-19.

Complex **14**					Complex **15**				
Atom	**$Mn^{(II)}$**	**$Mn^{(III)}$**	**$Mn^{(IV)}$**	**Ox.**	**Atom**	**$Mn^{(II)}$**	**$Mn^{(III)}$**	**$Mn^{(IV)}$**	**Ox.**
Mn1	**4.45**	**4.15**	**4.06**	**(IV)**	**Mn1**	**4.43**	**4.13**	**4.04**	**(IV)**
Mn2	**1.99**	**1.86**	**1.83**	**(II)**	**Mn2**	**2.12**	**2.03**	**2.01**	**(II)**
Complex **16**					Complex **17**				
Atom	**$Mn^{(II)}$**	**$Mn^{(III)}$**	**$Mn^{(IV)}$**	**Ox.**	**Atom**	**$Mn^{(II)}$**	**$Mn^{(III)}$**	**$Mn^{(IV)}$**	**Ox.**
Mn1	**1.97**	**1.84**	**1.80**	**(II)**	**Mn1**	**3.68**	**4.13**	**4.05**	**(IV)**
Mn2	**4.46**	**4.16**	**4.07**	**(IV)**	**Mn2**	**2.11**	**2.03**	**1.99**	**(II)**
Complex **18**					Complex **19**				
Atom	**$Mn^{(II)}$**	**$Mn^{(III)}$**	**$Mn^{(IV)}$**	**Ox.**	**Atom**	**$Mn^{(II)}$**	**$Mn^{(III)}$**	**$Mn^{(IV)}$**	**Ox.**
Mn1	**4.45**	**4.15**	**4.06**	**(IV)**	**Mn2**	**4.47**	**4.17**	**4.08**	**(IV)**
Mn2	**1.86**	**1.78**	**1.75**	**(II)**	**Mn4**	**2.21**	**2.08**	**2.03**	**(II)**

Reaction of anhydrous $MnBr_2$ with $heedH_2$ in EtOH produces the complex $[Mn^{II}_2Mn_2{}^{IV}_2O_2(heed)_2(EtOH)_6Br_2]Br_2$ (**14**) which crystallises in the monoclinic space group $P2_1/c$ (Table 1). The core of the complex consists of a linear zig-zag arrangement of four Mn ions (Fig. 4.3), with charge balance considerations, Analysis of the bond lengths and Bond Valence Sum (BVS) calculations (Tables 4.2 and 4.3) showing that the two outer Mn ions (Mn2 and s.e) are in the II+ oxidation state and the two central Mn ions (Mn1 and s.e) are in the IV+ oxidation state. The two central Mn^{IV} ions are linked via two symmetry equivalent μ-O^{2-} ions (O1) - an inversion centre lying at the midpoint between O1 and O1′ (Fig. 4.3). The tripodal $heed^{2-}$ ligands are doubly deprotonated lying above and below the Mn1…Mn1′ plane, bonding terminally to the central Mn^{IV} centres through their N-atoms (Mn1-N11 = 2.089(2), Mn1-N231 = 2.053(2) Å), while the two alkoxide arms (O331, O431) bridge the central Mn^{II} ions to the outer Mn^{IV} ions in a η^1:η^1:μ-fashion. Each metal centre exhibits distorted octahedral geometry with the coordination spheres at the peripheral Mn^{II} sites completed by terminal Br^- ions (Br1) and EtOH molecules. The resultant $[Mn_2{}^{II}Mn_2{}^{IV}O_2(heed)_2(EtOH)_6Br_2]^{2+}$ cation is charge balanced by the presence of two Br^- anions (Br2 and s.e) which "link" the $[Mn_4]$ clusters through H-bonding to their $-NH_2$ protons (N231-H23···Br2 = 3.483 Å, N231-H4···Br2 [1-x, 0.5+y, 1.5-z] = 3.491 Å) and terminal EtOH ligands (O14-H28···Br2 [x, 1.5-y, -0.5+z] = 3.275 Å) to form layers running parallel to the *bc* plane (Figure 4.4).

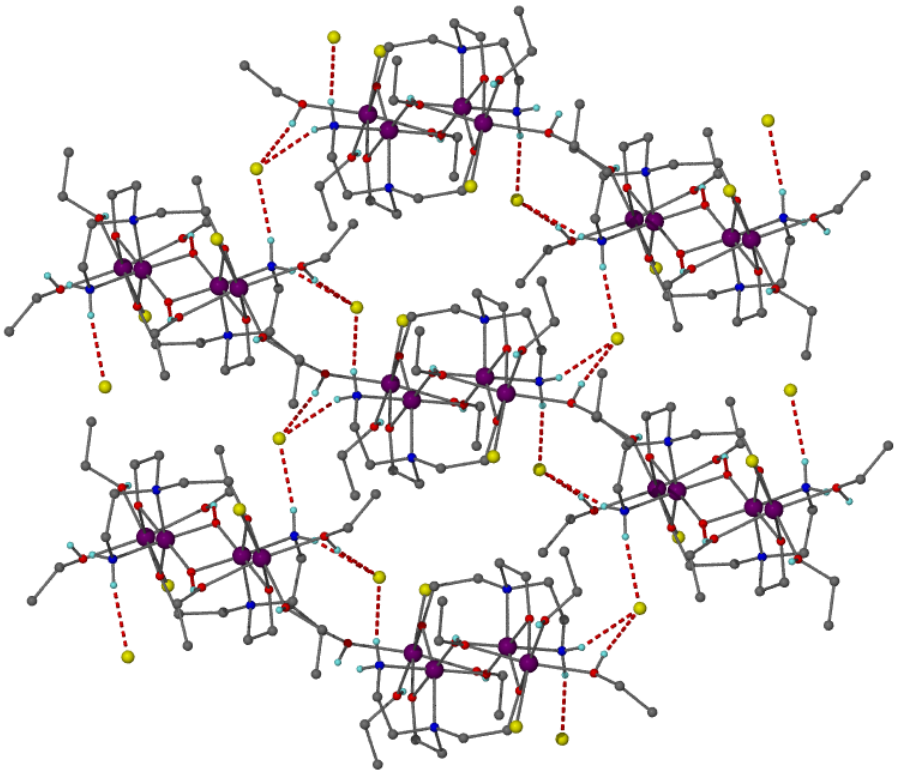

Figure 4.4: The H-bonded layer in 14 running parallel to the *bc* plane. Most hydrogen atoms have been omitted for clarity

Those layers are further bridged through two complementary H-bonds that involve the second EtOH molecule and the terminal Br^- ions (O13-H24···Br1 [2-x, 2-y, 1-z] = 3.234 Å). The third EtOH molecule forms an intra-molecular H-bond with one μ-O^{2-} ion. The (numerous) inter-molecular H-bonding interactions lead to the individual [Mn_4] clusters packing in the common brickwall formation in the crystal (Fig. 4.3).

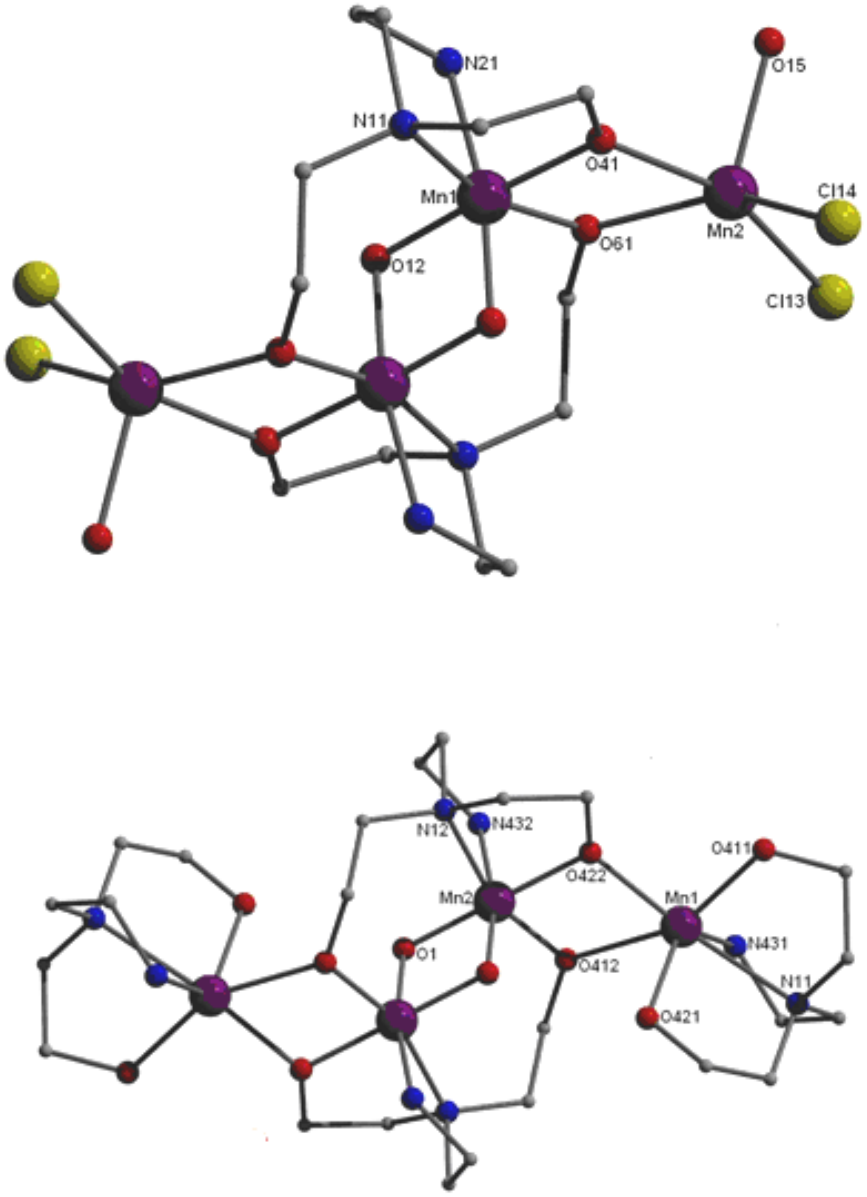

Figure 4.5. Molecular structures of $[Mn_4O_2(heed)_2(H_2O)_2Cl_4]$ (15, top) and $[Mn_4O_2(heed)_2(heedH_2)_2](ClO_4)_4$ (16, bottom). Colour code: Mn = purple, O = red, N = blue, C = grey

The same reaction using $MnCl_2 \cdot 6H_2O$ produces the analogous complex $[Mn^{II}_2Mn^{IV}_2(heed)_2(H_2O)_2Cl_4] \cdot 2EtOH \cdot H_2O$ (**2**·2EtOH·H_2O). **15** (Figure 4.5) crystallises in the rhombohedral R-3 space group and differs from **14** only in that

it contains four terminally bound Cl^- ions and two H_2O molecules on the peripheral Mn^{II} ions, instead of two halides and six solvent molecules. The result is a neutral complex. Numerous H-bonding interactions are observed between the discrete [Mn_4] molecules, primarily forged by the four terminal Cl^- ligands (Cl3 and Cl4). Both interact with protons from two nearby heed^{2-} (NH_2) protons (N21-H21···Cl13 [1/3+y, 2/3-x+y, 2/3-z] = 3.308, N21-H22···Cl14 [1/3-x+y, 2/3-x, -1/3+z] = 3.315 Å) on two neighbouring [Mn_4] units. A strong H-bond is also formed between the μ-bridging O^{2-} ion (O12 and s.e) situated at the centre of the [$Mn^{II}_2Mn^{IV}_2O_6$] core and the terminal H_2O molecule of an adjacent cluster (O15-H15···O12 [1/3+x-y, -1/3+x, 2/3-z] = 2.601 Å), which in turn is also H-bonded to a neighbouring Cl^- ligand (O15-H16···Cl14 [1/3-x+y, 2/3-x, -1/3+z] = 3.140 Å). In this arrangement each [Mn_4] unit is H-bonded to four other [Mn_4] units *via* 16 H-bonds (Figure 4.6) giving rise to a three-dimensional (3D) framework which adopts the **sod** topology[13-15] (Fig. 4.7) with Schlafli symbol $4^2.6^4$. Hexagonal channels with ca. 9Å diameter running along the *c* axis are formed within the 3D framework of **15** (Fig. 4.7).

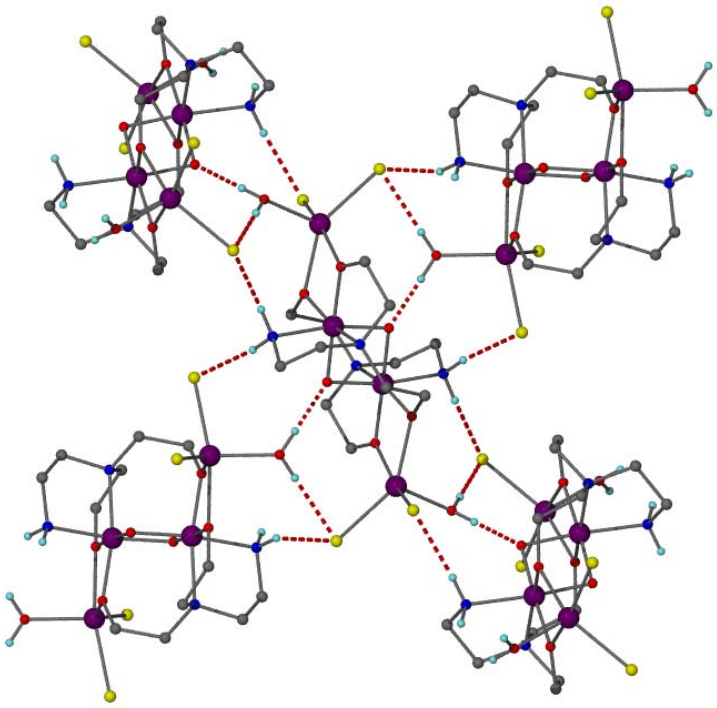

Figure 4.6. The H-bonding around 15. Most hydrogen atoms have been omitted for clarity

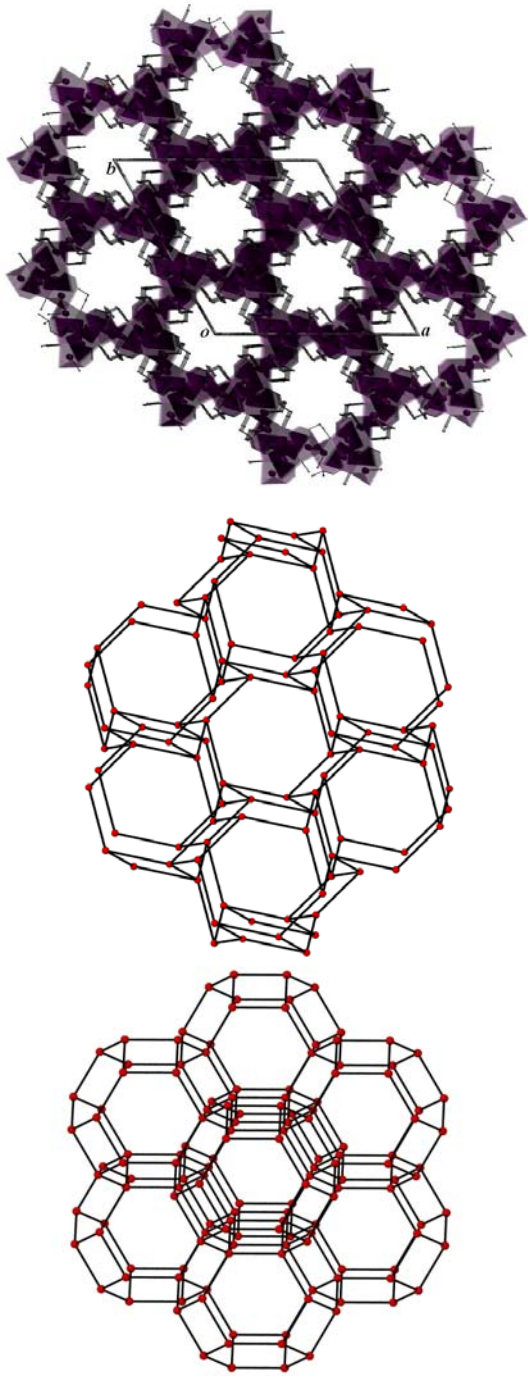

Figure 4.7. R-3 packing motif in 15 shown down the c-axis. H atoms have been omitted for clarity and the {MnO_4N_2} polyhedra are shaded in purple (top). The sod network adopted by 15 (middle) and the ideal sod net (bottom).

Using $Mn^{II}(ClO_4)\cdot 6H_2O$ removes the availability of terminal ligands (i.e Hal^-) and gives rise to the formation of the complex $[Mn^{II}_2Mn^{IV}_2O_2(heed)_2(heedH_2)_2](ClO_4)_4$ (**16**, Figure 4.5). Although the $\{Mn^{II}_2Mn^{IV}_2O_6\}$ core remains identical, the peripheral ligation is markedly different. The four $heed^{x-}$ ligands (two crystallographically unique pairs) in **16** appear in two different levels of deprotonation, which leads to different bonding motifs. As in **14** and **15**, two doubly deprotonated $heed^{2-}$ ligands sit above and below the central $Mn^{IV}\cdots Mn^{IV}$ plane using their $=N–CH_2CH_2O^-$ arms to bridge the outer Mn^{II} ions to the central Mn^{IV} centres. The second type remain neutral ($heedH_2$) and face-cap the outer Mn^{II} ions through N-atoms (N431 and N11) and their alcohol arms (O411 and O421) (Fig. 4). The $[Mn^{II}_2Mn^{IV}_2O_2(heed)_2(heedH_2)_2]^{4+}$ complex is charge balanced by four ClO_4^- counter ions (two symmetry related pairs) linked to the tetranuclear cluster via H-bonding interactions with the –OH and $–NH_2$ protons on the capping $heedH_2$ and bridging $heed^{2-}$ arms of the tripodal ligands. This inter-molecular H-bonding between the clusters and the perchlorates in **16** creates a 2D layer running parallel to the *ab* plane. The layers are connected to the third dimension *via* weaker H-bonds that involve the perchlorate oxygen atoms and alkyl protons of $heed^{2-}$ ligands on adjacent $[Mn_4]$ moieties.

Introduction of the chelating ligand 2,2-bipyridine (bpy) to the general reaction scheme, expands this family further with the formation of the similar complexes $[Mn^{II}_2Mn^{IV}_2O_2(heed)_2(bpy)_2(MeCN)_2(H_2O)_2](ClO_4)_4$ (**17**) and $[Mn^{II}_2Mn^{IV}_2O_2(heed)_2(bpy)_2Br_4]$ (**18**, Figure 4.9) which crystallize in the same crystal system and space group(see table 4.1).

The $\{Mn^{II}_2Mn^{IV}_2O_6\}$ core remains intact in both cases and differ to their siblings only in the presence of two chelating 2,2-bpy ligands capping the ends of the $[Mn_4]$ complexes at the Mn^{II} sites. The remaining coordinating sites at the Mn^{II} ions are occupied by terminal MeCN and H_2O ligands in **17**, and four terminal Br^- ions in **18**.

The clusters of **17** form H-bonded chains along the *a* axis which involve one hydrogen atom of the terminal H_2O molecules, one $–NH_2$ proton of the heed^{2-} ligand and one of the two crystallographically independed ClO_4^- anions (O28-H282···O39 = 2.966 Å, N12-H122···O38 [1+x,y,z] = 3.027 Å) (Figure 4.8).

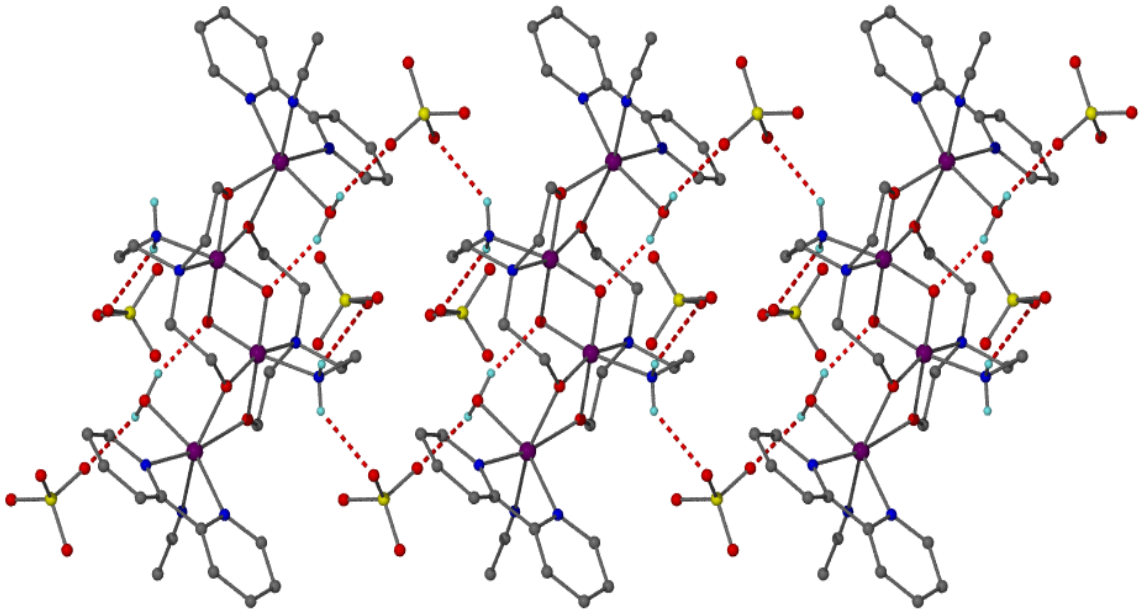

Figure 4.8. The H-bonded chain in 17 along the *a* axis. Most hydrogen atoms have been omitted for clarity.

The second crystallographically independent ClO_4^- anion is H-bonded to a $[Mn_4]$ cluster *via* a single H-bond. These linear chains of **17** pack in parallel rows along the *b* axis due to intermolecular π-π stacking interactions ($\pi_{centroid}\cdots\pi_{centroid}$ = 3.605 Å and 3.775 Å) between the chelating bpy ligands forming a 2D layer parallel to the *ab* plane.

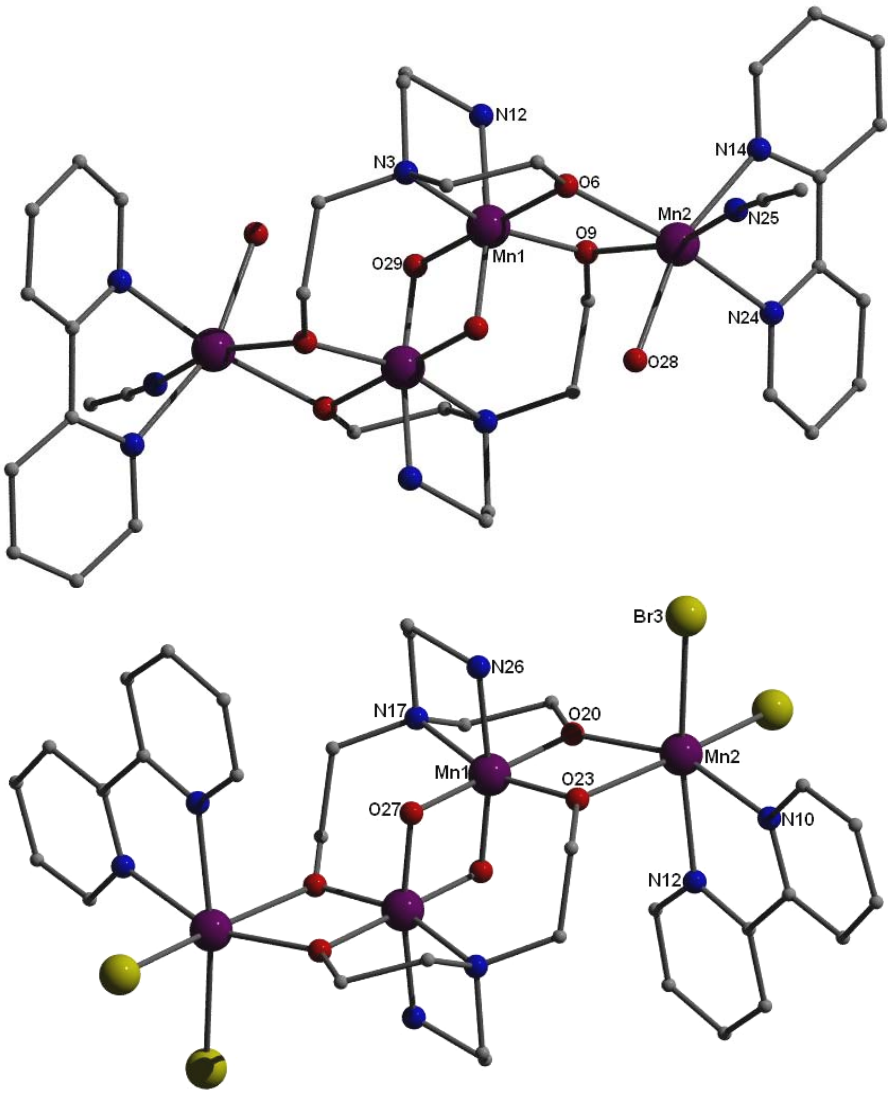

Figure 4.9. Molecular structures of $[Mn_4O_2(heed)_2(MeCN)_2(H_2O)_2(bpy)_2]$ (17) (top) and $[Mn_4O_2(heed)_2(bpy)_2Br_4]$ (18) (bottom). Colour code: Mn = purple, O = red, N = blue, C = grey, Br = yellow

The $[Mn_4]$ clusters in **18** are also arranged in H-bonded chains running along the *b* axis which involve the terminal Br^- ions (Br3) and the hydrogen atoms of the $-NH_2$ groups of the $heed^{2-}$ ligands of adjacent $[Mn_4]$ clusters (N26-H261···Br3 = 3.567 Å, N26-H262···Br3 [-x,2-y,1-z] = 3.521 Å), forming $R_2^2(8)$ rings (Figure

4.10). The MeOH solvent molecule of crystallisation in **18** hydrogen bonds to the other terminal Br^- ion (Br4) at a distance of 3.276 Å (O29-H291···Br4). Akin to **17**, the [Mn_4] chains in **18** interact through π-π stacking interactions ($\pi_{centroid}\cdots\pi_{centroid}$ = 3.789 Å) to form a layer parallel to the *bc* plane. Weaker H-bonding interactions stabilise the packing of the molecules in the crystal. Those interactions involve the Br^- ions and both the aromatic bpy protons and the aliphatic protons of the alkyl arms of the $heed^{2-}$ ligands on neighbouring [Mn_4] clusters.

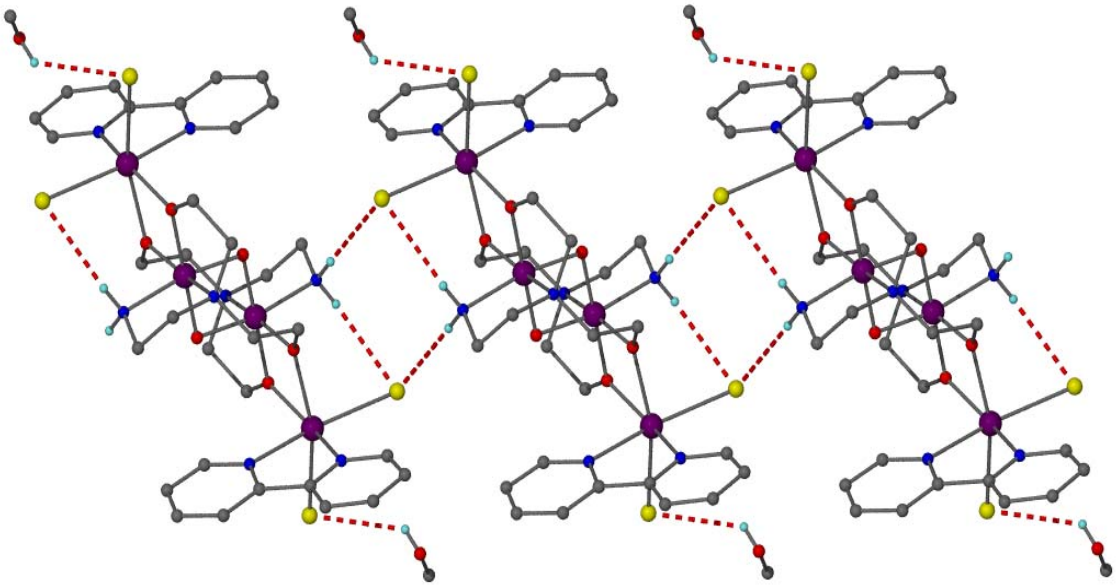

Figure 4.10. The H-bonded chain in 18 along the *b* axis. Most hydrogen atoms have been omitted for clarity.

The presence of terminal halide ions and solvent molecules in complexes **14**, **15** and **18** alerted us to the possibility of replacing these with (linear) connector ligands in order to introduce 1-, 2- or 3-dimensionality. The linking of paramagnetic clusters into such arrays may provide new and important insights into the transition from purely molecular magnetic properties to long range 1, 2 and 3-D bulk magnetic order. Furthermore, the ordering or templating of such paramagnetic systems may eventually form the basis for commercial fabrication of arrays of such magnetic materials.[16] To this end reaction of anhydrous $MnBr_2$,

heedH_2 and sodium dicyanamide (Na(dca); $NaN(CN)_2^-$) produces $[\{Mn^{II}_2Mn^{IV}_2O_2(heed)_2(H_2O)_2(MeOH)_2(dca)_2\}Br_2]_n$ (**19**, Figures 4.11-4.13). The $[Mn^{II}_2Mn^{IV}_2O_6]$ core in **19** is isostructural to its siblings and coordination at the peripheral Mn^{II} sites (Mn2) is completed by two H_2O and EtOH ligands and four dca^- ligands which occupy two equatorial positions at each Mn^{II} centre (Figure 4.11).

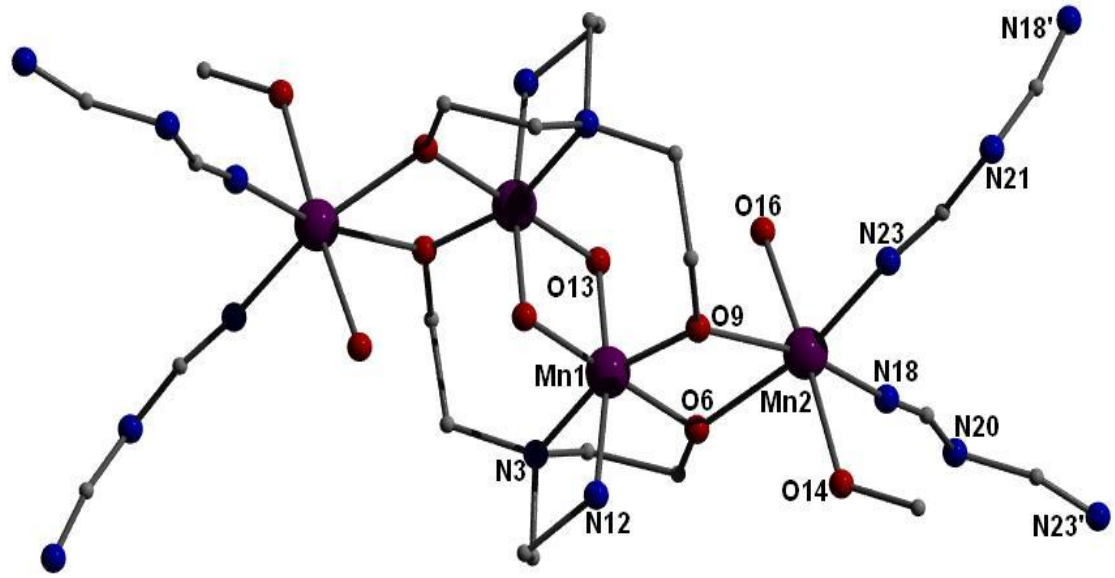

Figure 4.11 Structure of the $[Mn^{II}_2Mn^{IV}_2O_2(Heed)_2(EtOH)_2(H_2O)_2(dca)_2]Br_2$ building block in 19. Br- ions and H-atoms have been omitted for clarity.

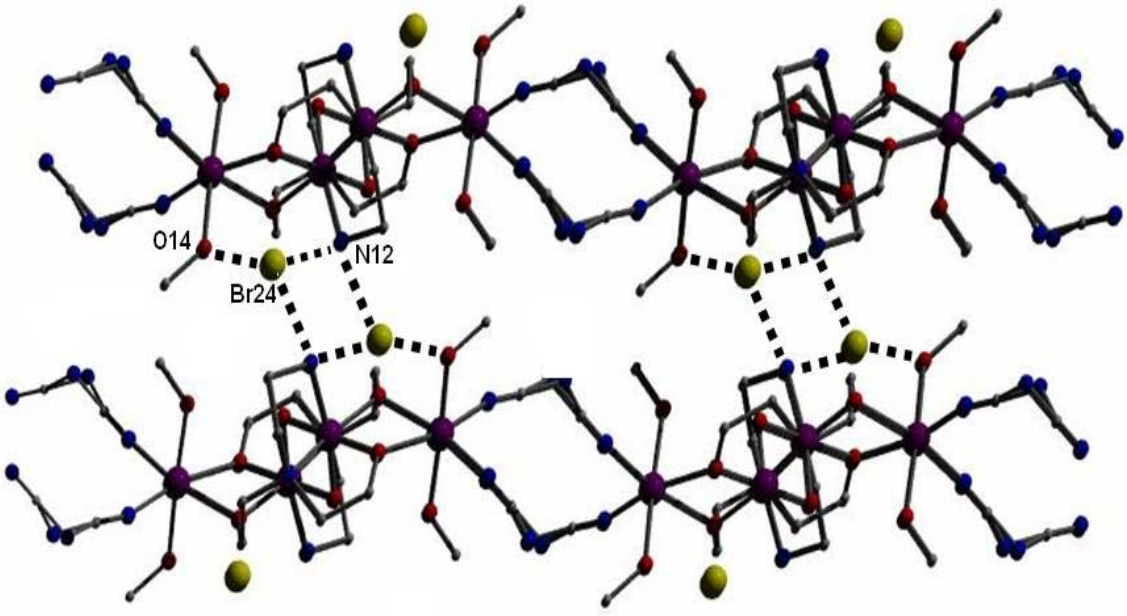

Figure 4.12 H-bonding interactions (dashed lines) linking the 2-D sheets in 19. Colour code: Mn = purple, O = red,

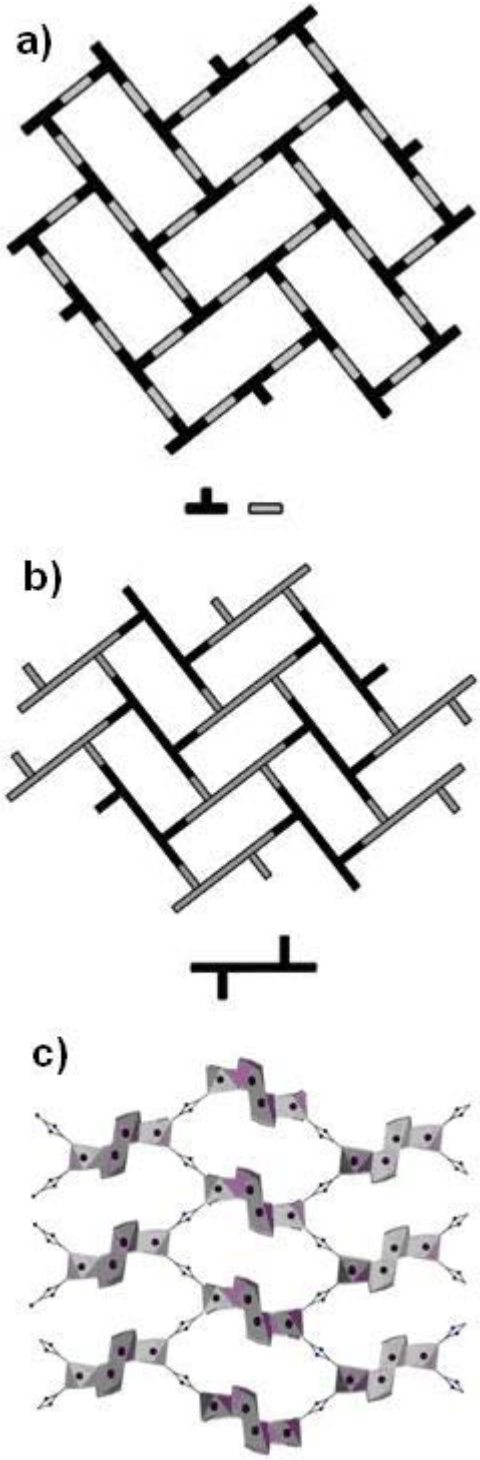

Figure 4.13 (a) Schematic illustrating (a) the common herring-bone 2-D topology built from 3-connector 'T' shaped nodes (inset). (b) The much rarer version of this topology comprising our $[Mn^{II}_2Mn^{IV}_2]$ building blocks (inset). (c) Crystal structure of the actual 2-D herring-bone topology observed in 19.

As observed in numerous dca- based 1, 2- and 3-D extended networks comprising monometallic nodes,[17] each dca^- ligand then bridges to another $[Mn^{II}_2Mn^{IV}_2]$ cluster to form a 2-D sheet with a [4, 4] grid-like topology (Figure 4.13c). More specifically the 2-D network in **19** joins a small family of extended networks possessing a rare form of the 2-D herring bone topology (Fig. 4.13a).[18-21] The more familiar 2-D herring bone motif comprises 3-connector nodes linked by linear spacer ligands (Fig. 4.13a), however we may best describe the connectivity in **19** by thinking of the $[Mn^{II}_2Mn^{IV}_2O_6]$ moieties as two fused 'T'-shaped 3-connector nodes which link to give our 2-D extended network (Figure 4.13b and 4.13c).

The 2-D sheets in **19** lie in the *ab* plane and propagate along the *c* axis to form an angle of approximately 30º with the *ab* plane, with respect to the cell origin. These planar sheets then stack in an off-set fashion along the *c* axis. The Br^- anions sit in between the 2-D sheets (Figure 4.12) and are "locked" there by three H-bonding interactions. Two H-bonds arise from the lower 2-D layer via a hydroxyl proton from a terminal MeOH ligand (O14-H142···Br24 [-x,1/2+y,1/2-z] = 3.250 Å) and a NH_2 proton from one amine arm of a $heed^{2-}$ ligand (N12 N12-H122···Br24 [-x,1/2+y,1/2-z] = 3.570 Å). The third and final H-bond is formed via a NH_2 proton from a symmetrically equivalent $heed^{2-}$ arm belonging to the upper 2-D sheet (N12-H121···Br24 = 3.621 Å). The second MeOH molecule forms an intra-molecular H-bond with one μ-O^{2-} ion (O16-H162···O13 [-x,2-y,1-z] = 2.736 Å). Each $[Mn_4]$ is H-bonded to two Br^- ions below the layer and to two Br^- ions above the layer. Therefore, each $[Mn_4]$ connects to four other $[Mn_4]$ moieties *via* the Br^- links. In this arrangement each $[Mn_4]$, which is connected to four other $[Mn_4]$ clusters through the dca^- anions, is also attached to four other $[Mn_4]$ clusters *via* the the H-bonded Br^- links. Therefore, each $[Mn_4]$ cluster serves as an 8-connected node within the resultant framework which adopts the **bcu** topology[14,15,22] with Schlafli symbol $4^{24}.6^4$ (Figure 4.14).

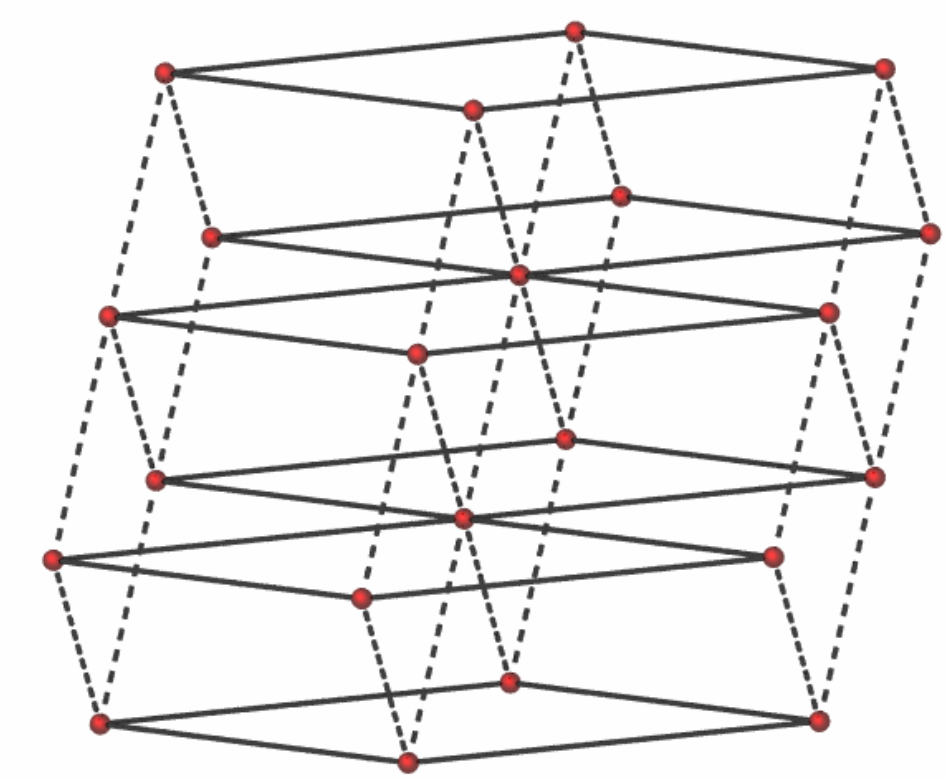

Figure 4.14. The 3D 8-connected bcu net adopted by 19. Solid lines represent the connections through the dca^- anions while dashed lines represent the H-bonded links.

Magnetic studies

Dc magnetic susceptibility studies were carried out on crystalline samples of **14-19** in the 300-4 K temperature range in an applied field of 0.1 T. The behaviour of **14-19** is essentially identical (within this temperature range) and so here we limit our discussion to complex **14**. The room temperature value of $\chi_m T$ in **14** (Figure 4.15) is slightly lower (10.67 cm^3 mol^{-1} K) than the expected value of ~12.5 cm^3 mol^{-1} K for four non-interacting Mn ions (2 × Mn^{II}, 2 × Mn^{IV}), indicative of dominant antiferromagentic exchange between the metal centres. $\chi_m T$ then slowly decreases with temperature before dropping more abruptly at approximately 125 K, reaching a value of 3.36 cm^3 mol^{-1} K at 4 K . Fitting of these data using the 2-*J* model described in Scheme 1 and spin-Hamiltonian (1) afforded the parameters $S = 0$, $g = 1.98$, $J_1 = -1.50$ cm^{-1} and $J_2 = -11.80$ cm^{-1}. The 1st ($S = 1$) and 2nd ($S = 2$) excited states lie just 0.32 and 1.01 cm^{-1} above the $S = 0$ ground state, explaining the relatively large value of 3.36 cm^3 mol^{-1} K observed at 4 K.

$$\mathcal{H} = -2J_1(\hat{S}_1 \cdot \hat{S}_2 + \hat{S}_3 \cdot \hat{S}_4) - 2J_2(\hat{S}_2 \cdot \hat{S}_3) \quad (1)$$

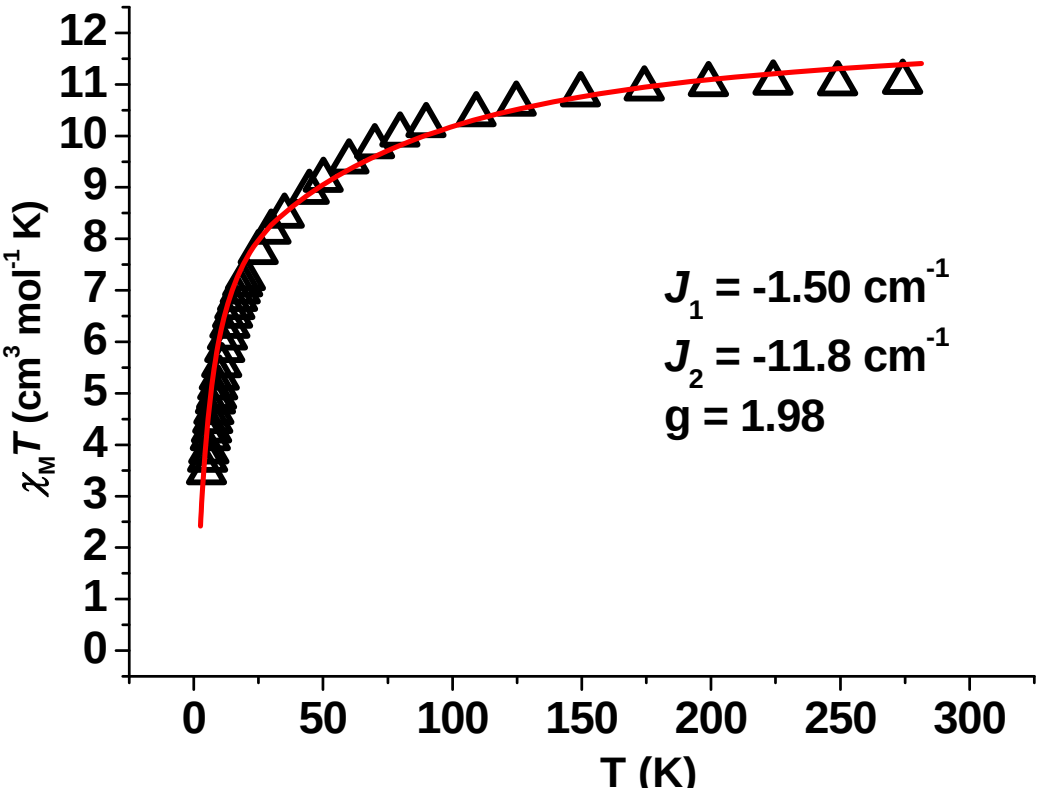

Figure 4.15 Plot of $\chi_M T$ vs. T obtained for 14 (Δ) along with the best-fit (solid red line) affording the spin-Hamiltonian parameters $J_1 = -1.50$ cm^{-1}, $J_2 = -11.8$ cm^{-1} and $g = 1.98$.

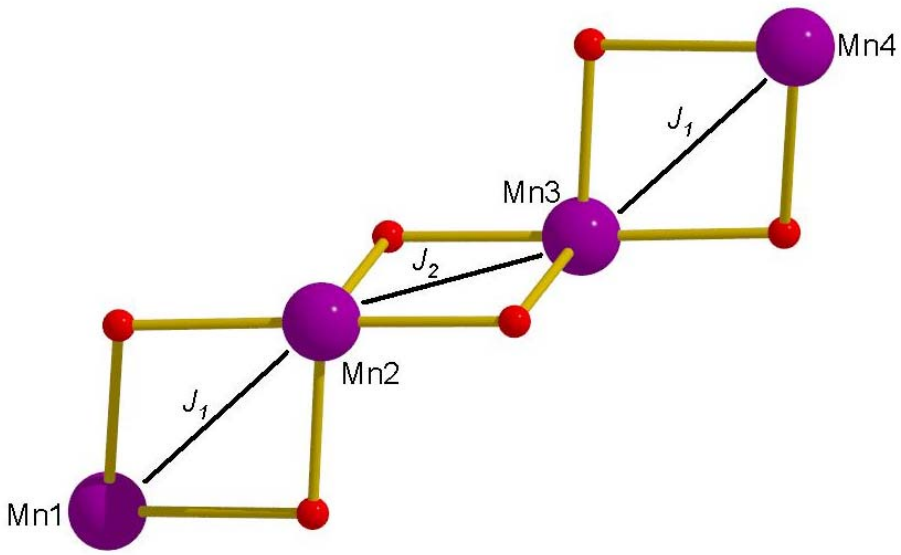

Figure 4.16. The exchange interaction scheme employed for 19.

Detailed field-dependent heat capacity experiments were conducted for **19** (Figure 4.16). The first striking feature is a λ-type anomaly observed at T = 3 K, having a relative height of ~ 1.2 R. Because its position and height are insensitive to the applied-field (Figure 4.17.a) and there is no counterpart in the magnetic susceptibility (Figure 4.15), we conclude this anomaly is of non-magnetic origin, and likely associated with a structural transition. At much lower temperatures, a second sharp peak occurring at T_N = 0.72 K reveals the onset of a phase transition, whose magnetic origin is proven by the fact that it is completely removed by applying fields of sufficient intensity (Fig. 4.17.a). One can notice though that it is hardly affected by the relatively large field B_0 = 1 T, suggesting the transition is to an antiferromagnetically ordered state. To get a deeper understanding of the magnetic ordering, we estimate the magnetic contribution C_m. Noting that fields higher than ~ 5 T are enough to shift any magnetic contribution well above 2 K (Fig. 4.17.a), we obtain C_m by subtracting the experimental specific heat measured for B_0 = 7 T to the total zero-field specific heat C. The result is depicted in Fig. 4.17.b, together with the curve obtained similarly for B_0 = 1 T.

The long tail above T_N reflects the presence of magnetic correlations, probably existing within the 2-D extended networks. At the lowest temperatures, the experimental specific heat displays a T^2-dependence, $C_m \propto AT^2$ with $A \cong 23$ mJK^{-1}mol^{-1}, suggesting the existence of 2-D spin waves with a linear dispersion relation. Finally, the estimate of the zero- field magnetic entropy content $\Delta S_m/R = \int C_m/(RT)\mathrm{d}T$ provides a curve tending at the higher-T to the value of ~ 1.5 R. The latter is in fair agreement with the magnetic entropy expected, R ln(2S+1) = 1.61 R, provided the spin value is S = 2; in agreement with the dc susceptibility data that showed both S = 1 and S = 2 states within 1 cm^{-1} of the S = 0 ground state.

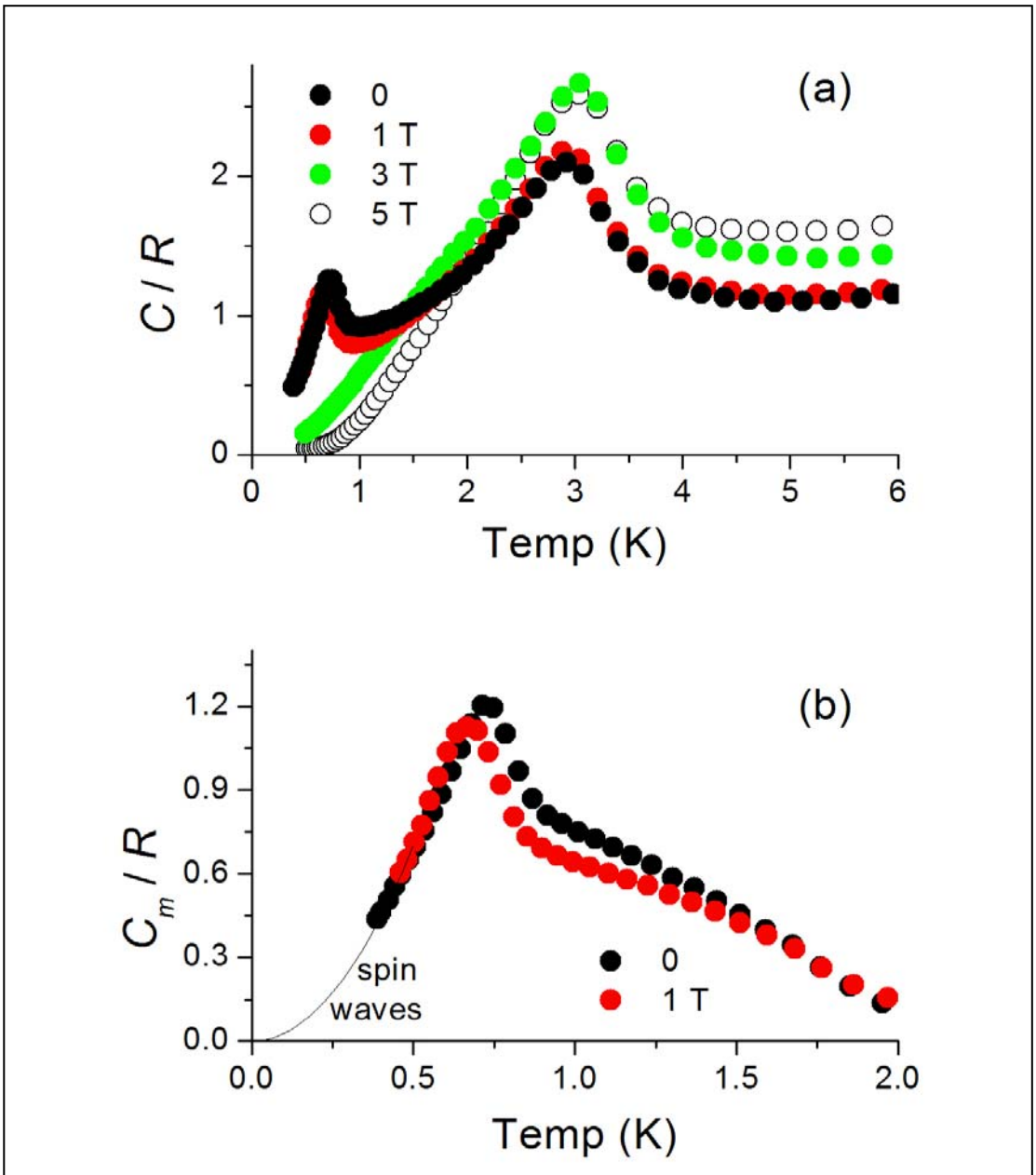

Figure 4.17a and 4.17b (a): Plot of the experimental specific heat *C* normalized to the gas constant *R* in the indicated temperature and field ranges. (b) Low-temperature magnetic contribution C_m to the specific heat. Solid line is the calculated contribution associated with spin-wave excitations

Conclusions

Initial investigations into the coordination chemistry of the unexplored tripodal ligand N,N-Bis(2-hydroxyethyl)ethylene diamine (heedH2) has produced a series of mixed-valent MnII/IV complexes [MnII2MnIV2O2(heed)2(EtOH)6Br2]Br2] (14), [MnII2MnIV2O2(heed)2(H2O)2Cl4].2EtOH.H2O (15), [MnII2MnIV2O2(heed)2(heedH2)2](ClO4)4 (16), [MnII2MnIV2O2(heed)2(MeCN)2(H2O)2(bpy)2](ClO4)4 (17) and [MnII2MnIV2O2(heed)2(bpy)2Br4].2MeOH (18). Clusters 14-18 represent rare examples of tetranuclear [Mn4O6] complexes exhibiting the linear zig-zag (trans) topology. Replacement of the terminal ligands (Br-, Cl-) with the linear connector dicyanamide (dca^-) anion results in the formation of the [4, 4] grid-like [{MnII2MnIV2O2(heed)2(H2O)2(EtOH)2(dca)2}Br2]n (19). The structure in 19 comprises a rare form of the 2-D sheet-like 'herring-bone' topology made up of two fused T-shaped 3-connector units, as opposed to the more common T-shaped 3-connector moieties observed in standard 2-D herring-bone architectures.

Experimental Section

All manipulations were performed under aerobic conditions, using materials as received. CAUTION! Although no problems were encountered in this work, care should be taken when using the potentially explosive perchlorate anion.

$[Mn_4O_2(heed)_2(EtOH)_6Br_2]Br_2$ (14)

Anhydrous $MnBr_2$ (0.5 g, 2.3 mmol) and $heedH_2$ (0.34 g, 2.3 mmol) were dissolved in 25 cm^3 of EtOH and stirred for 1 h. The solution was then filtered and X-ray quality crystals of **14** were obtained upon slow Et_2O diffusion into the mother liquor in ~42% yield. Elemental analysis (%) calculated for $C_{24}H_{64}N_4O_{12}Br_4Mn_4$: C 25.28, H 5.66, N 4.91; Found: 24.92, H 5.39, N 4.53.

$[Mn_4O_2(heed)_2(H_2O)_2(Cl)_4]$ (15)

$MnCl_2{\cdot}4H_2O$ (0.4 g, 2 mmol) and $heedH_2$ (0.29 g, 2 mmol) were dissolved in 25

cm^3 of EtOH and stirred for 1 h. X-ray quality crystals of **15** were obtained in good yield (35%) after slow evaporation of the mother liquor. Elemental analysis (%) calculated for $C_{12}H_{32}N_4O_8Cl_4Mn_4$: C 19.96, H 4.47, N 7.76; Found: C 19.20, H 4.90, N 7.35.

$[Mn_4O_2(heed)_2(heedH_2)_2](ClO_4)_4$ (16)

$Mn(ClO_4)_2.4H_2O$ (0.72 g, 2.8 mmol) and $heedH_2$ (0.4 g, 2.8 mmol) were dissolved in 25 cm^3 of MeCN and stirred for 1 h. Upon filtration and Et_2O diffusion, black crystals of **16** were formed in ~40% yield after 2 days. Elemental analysis (%) calculated for $C_{24}H_{60}N_8O_{26}Cl_4Mn_4$: C 23.28, H 4.88, N 9.05; Found: C 23.75, H 4.73, N 9.76.

$[Mn_4O_2(heed)_2(MeCN)_2(H_2O)_2(bpy)_2](ClO_4)_4$ (17)

$Mn(ClO_4)_2.6H_2O$ (0.35 g, 1.38 mmol), $heedH_2$ (0.2 g, 1.38 mmol) and 2,2-bipyridyl (0.215 g, 1.38 mmol) were dissolved in 25 cm^3 of MeCN and stirred for 1 h. The solution was then filtered and diffused slowly with Et_2O. After 3 days black crystals of **17** were obtained in ~40% yield. Elemental analysis (%) calculated for $C_{36}H_{54}N_{10}O_{24}Cl_4Mn_4$: C 31.51, H 3.97, N 4.21; Found: C 31.43, H 4.22, N 4.36.

Synthesis of $[Mn_4O_2(heed)_2(bpy)_2Br_4]$ (18)

Anhydrous $MnBr_2$ (0.30 g, 1.38 mmol), $heedH_2$ (0.20 g, 1.38 mmol) and 2,2-bipyridyl (0.215 g, 1.38 mmol) were dissolved in MeOH (25 cm^3) and stirred for 1 h. X-ray quantity crystals of **18** were obtained in good yield (~40%) after slow evaporation of the mother liquor. Elemental analysis (%) calculated for $C_{32}H_{44}N_8O_6Br_4Mn_4$: C 32.68, H 3.77, N 9.53; Found: C 33.11, H 3.91, N 9.87.

$[\{Mn^{II}_2Mn^{IV}_2O_2(heed)_2(H_2O)_2(MeOH)_2(dca)_2\}Br_2]_n$ (19)

Anhydrous $MnBr_2$ (0.30 g, 1.38 mmol), $heedH_2$ (0.20 g, 1.38 mmol) and Na(dca) (0.13 g, 1.38 mmol) were dissolved in MeOH (25 cm^3) and stirred for 2 h. X-ray quality crystals of **19** were obtained upon slow evaporation of the mother liquor in ~42 % yield after 3 days. Elemental analysis (%) calculated for

$C_{10}H_{24}N_5O_6Br_1Mn_2$: C 24.02, H 4.84, N 14.00; Found: C 24.84, H 5.30, N 14.43.

X-ray Crystallography

Diffraction data were collected at 150 K on a Bruker Smart Apex CCDC diffractometer, equipped with an Oxford Cryosystems LT device, using Mo radiation. The structures **14-19** were solved by direct methods (SIR92) and refined by full matrix least-squares against F^2 (CRYSTALS).[23] See Table 4.1

(**14**): Hydrogen atoms attached to carbon were placed geometrically. All hydrogens on oxygen and nitrogen were located in a difference map. Hydrogens were refined subject to geometric contraints on bond lengths and angles before finally being contrained to ride on their host atoms.

(**15**): Disordered solvent was dealt with using Platon SQUEEZE and amounted to 2EtOH and $1H_2O$ per formula unit (see CIF for full details).

(**16**): The data obtained from **16** were integrated as a twin with 2 domains. Structure solution and initial refinement were carried out using data from only domain 1. Refinement was then carried out using all data from both domains. Hydrogens attached to carbon were placed geometrically. Hydrogens on nitrogen were located in a difference map and refined subject to geometric restraints. The hydroxy hydrogen atoms were placed along H-bonding interations as the difference map indicated they were disordered due to 2 possible H-bonding interactions. Hydrogens were placed along both interations with occupancy of 0.5. The occupancy was not refined. All H-atoms were constrained to ride on their host atoms.

(**17**) and (**18**): The hydrogen atoms were all located in a difference map, but those attached to carbon atoms were repositioned geometrically. The H atoms were initially refined with soft restraints on the bond lengths and angles to regularise their geometry (C---H in the range 0.93--0.98, N---H in the range 0.86--0.89, N---H to 0.86, O---H = 0.82 \%A) and U~iso~(H) (in the range 1.2-1.5 times U~eq~ of the parent atom), after which the positions were refined with riding constraints.
(**19**): The structure in **19** is disordered with two Mn coordination sites (Mn^{II} ions) being part occupied by MeOH and water, refined to give a total occupancy of one

for each coordinating molecule. The central nitrogen on the dca ligand is also disordered and here the occupancy of the two atomic sites has been fixed at 0.5. There is also disordered solvent which has been dealt with using Platon SQUEEZE (see refinement details). Hydrogen atoms on the disordered groups were positioned geometrically. Other H-atoms were located in a difference map, and those attached to carbon atoms were repositioned geometrically. The H atoms were initially refined with soft restraints on the bond lengths and angles to regularise their geometry (C---H in the range 0.93--0.98, N---H in the range 0.86--0.89, N---H to 0.86 O---H = 0.82) and U~iso~(H) (in the range 1.2-1.5 times U_{eq} of the parent atom), after which the positions were refined with riding constraints.

Data collection parameters and structure solution and refinement details are listed in Table 1. Full details can be found in the CIF files provided in the supporting information and CCDC.

References

1 (a) A. Caneschi, D. Gatteschi, R. Sessoli, A. L. Barre, L. C. Brunel and M. Guillot., *J. Am. Chem. Soc.,* 1991, **113**, 5873-5874. (b) R. Sessoli, D. Gatteschi, A. Caneshi and M. A. Novak, *Nature,* 1993, **365**, 141. (c) R. Sessoli, H. L. Tsai, A. R. Schake, S. Y. Wang, J. B. Folting, D. Gatteschi, G. Christou and D. N. Hendrickson, *J. Am. Chem. Soc,* 1993, **115**, 1804.

2. (a) V. K. Yachandra, K. Sauer and M. P. Klein., *Chem. Rev.,* 1996, **96**, 2927. (b) V. K. Yachandra, K. Sauer., *Biochim. Biophys. Acta.,* 2004, **1655**, 140. (c) B. Kok, B. Forbrush and M. McGloin, *Photochem. Photobiol.,* 1970, **11**, 457. (d) M. Haumann, P. Liebisch, C. Muller, M. Barra, M. Grabolle and H. Dau., *Science*, 2005, **310**, 1019. (d) S. Mukhopadhyay, S. K. Mandal, S. Bhaduri, and W. H. Armstrong,*Chem. Rev*. **2004**, 104, 3981.

3. (a) K. Ferreira, T. M. Iverson, K. Maghlaoui, J. Barber and S. Iwata., *Science*, 2004, **303**, 1831. (b) S. Iwata and J. Barber., *Curr. Opin. Struct. Biol.* 2004, **14**, 447. (c) B. Loll, W. Saenger, J. Messinger, A. Zouni and J. Biesiadka., *Nature*, 2005, **438**, 1040.

4. J. Yano, J. Kern, K. Sauer, M. J. Latimer, Y. Pushkar, J. Biesiadka, B. Loll, W. Saenger, J. Messinger, A. Zouni and V. K. Yachandra., *Science*, 2006, **314**, 821.

5. Examples include: (a) J. B. Vincent, C. Christmas, J. C. Huffman, G. Christou, H.-R. Chang and D. N. Hendrickson., *Chem. Commun.,* 1987, 236. (b) R. J. Kalawiec, R. H. Crabtree, G. W. Brudvig and G. K. Schulte., *Inorg. Chem.,* 1988, **27**, 1309. (c) J. B. Vincent, C. Christmas, H.-R. Chang, Q. Li, P. D. W. Boyd, J. C. Huffman, D. N. Hendrickson and G. Christou., *J. Am. Chem. Soc.,* 1989, **111**, 2086. (d) S. Wang, M. S. Wemple, J. Yoo, K. Folting, J. C. Huffman, K. S. Hagen, D. N. Hendrickson and G. Christou., *Inorg. Chem*., 2000, **39**, 1501. (e) G. S. Papaefstathiou, A. Escuer, C. P. Raptopoulou, A. Terzis, S. P. Perlepes, R. Vicente, *Eur. J. Inorg. Chem*., 2001, 1567. (f) D. J. Price, S. R. Batten, K. J. Berry, B. Moubaraki and K. S. Murray., *Polyhedron*, 2003, **22**, 165. (g) A. J. Tasiopoulos, W. Wernsdorfer, K. A. Abboud and G. Christou., *Inorg. Chem*., 2005, **44**, 6324. (h) H. Miyasaka, K. Nakata, L. Lecren, C. Coulon, Y. Nakazawa, T. Fujisaki, K. Sugiura, M. Yamashita and R. Clerac, *J. Am. Chem. Soc*., **2006**,

128, 3770 (i) L. M. Wittick, L. F. Jones, P. Jensen, B. Moubaraki, L. Spiccia, K. J. Berry and K. S. Murray., *Dalton Trans*., 2006, 1534.

6. Examples include: (a) V. McKee, W. B. Sheperd and S. J. Lippard., *Chem. Commun.,* 1985, 158. (b) S. Brooker, V. McKee, W. B. Sheperd, and L. K. Parnell, *J. Chem. Soc. Dalton Trans*., 1987, 2555. (c) K. L. Taft, A. Caneschi, C. D. Delfs, G. C. Papeafthymiou and S. J. Lippard., *J. Am. Chem. Soc.,* 1993, **115**, 11753. (d) G. Aromi, S. Bhaduri, P. Artus, K. Folting and G. Christou, *Inorg. Chem*., 2002, **41**, 805. (e) J.-Z. Wu, E. Sellitto, G. P. A. Yap, J. Shealts and G. C. Dismukes., *Inorg. Chem*., 2004, **43**, 5795. (f) B. F. Abrahams, T. A. Hudson and R. Robson., *Chem. Eur. J.,* 2006, **12**, 7095.
7. Examples include: (a) J. C. Jeffrey, P. Thornton and M. D. Ward. *Inorg. Chem.,* 1994, **33**, 3612-3615. (b) D. A. Bardwell, J. C. Jeffrey and M. D. Ward. *Dalton Trans.,* 1995, **18**, 3071. (c) J. Yoo, A. Yamaguchi, M. Nakano, J. Krzystek, W. E. Streib, L.-C. Brunel, H. Ishimoto, G. Christou and D. N. Hendrickson. *Inorg. Chem.,* 2001, **40**, 4604. (d) C. Desroches, G. Pilet, S. A. Borshch, S. Parola and D. Luneau. *Inorg. Chem.,* 2005, **44**, 9112.
8. (a) E. K. Brechin., *Chem. Commun*., 2005, 5141. and references therein. (b) M. Manoli, R. D. L. Johnstone, S. Parsons, M. Murrie, M.Affronte, M. Evangelisti and E. K. Brechin. *Angew. Chem. Int. Ed.* 2007, 46, 4456.
9. C. Jocher, T. Pape, W. W. Seidel, P. Gamez, J. Reedjik and F. E. Hahn, *Eur. J. Inorg. Chem*, 2005, 4914.
10. B. Song, J. Reuber, C. Ochs, F. E. Hahn, T. Lugger and C. Orvig, *Inorg. Chem.,* 2001, **40**, 1527.
11. C. Philouze, G. Blondin, J.-J. Cirerd, J. Guilhem, C. Pascard and D. Lexal. *J. Am. Chem. Soc*., 1994, **116**, 8557.
12. G. Aromí, P. Gamez, C. Boldron, H. Koojiman, A. L. Spek and J. Reedijk. *Eur. J. Inorg. Chem*., 2006, 1940.
13. O. Delgado Friedrichs, M. O'Keeffe and O. M. Yaghi, *Acta Cryst*., 2003, **A59**, 515.
14. The topological analysis of the net was performed using the TOPOS program package http://www.topos.ssu.samara.ru.

15. V. A. Blatov, “Multipurpose crystallochemical analysis with the program package TOPOS, *IUCr CompComm Newsletter*, 2006, 4.

16. M. Mannini, D. Bonacchi, L. Zobbi, F. M. Piras, E. A. Speets, A. Caneschi, A. Cornia, A. Magnani, B. J. Ravoo, D. N. Reinhoudt, R. Sessoli and D. Gatteschi., *Nano. Lett.* 2005, **5**, 1435.

17. S. R. Batten and K. S. Murray, *Coord. Chem. Rev.,* 2003, **246**, 103 and references therein.

18. A. V. Powell, R. Paniagua, P. Vaquiero and A. M. Chippendale., *Chem. Mater*., 2002, **14**, 1220.

19. Y. Wan, L. Zhang, L. Jin, S. Gao and S. Lu. *Inorg. Chem*., 2003, **42**, 4985.

20. S. Zang, Y. Su, Y. Li, Z. Ni and Q. Meng. *Inorg. Chem.,* 2006, **45**, 174.

21. K. Eda, Y. Iriki, K. Kawamura, T. Ikuki and M. Hayashi. *J. Solid State Chem*., 2007, **180**, 3588.

22. O. Delgado Friedrichs, M. O'Keeffe and O. M. Yaghi, *Acta Cryst*., 2003, **A59**, 22.

23. P. W. Betteridge, J. R. Carruthers, R. I. Cooper, K. Prout and D. J. Watkin, *J. Appl. Cryst.,* 2003, **36**, 1487.

Publications

13. Calix[4]arene clusters as enhanced magnetic coolers *and* molecular magnets G. Karotsis, S. Kennedy, S. J. Teat, C. M. Beavers, D. A. Fowler, J. J. Morales, M. Evangelisti,* S. J. Dalgarno,* E. K. Brechin *J. Am. Chem. Soc* **2010**, 132, 12983.

12. Metal-organic calixarene nanotubes. S. Kennedy, G. Karotsis, C. M. Beavers, S. J. Teat, E. K. Brechin, S. J. Dalgarno. *Angew. Chem. Int. Ed*., **2010**, 49, 4205.

11. Calixarene supported enneanuclear Cu(II) clusters. G. Karotsis, S. Kennedy, S. J. Dalgarno, E. K. Brechin. *Chem. Commun*.,**2010**, 46, 3884.

10. Planar [Ni-7] discs as double-bowl, pseudo metallacalix[6]arene host cavities. S. T. Meally, G. Karotsis, E. K. Brechin, G. S Papaefstathiou, P. W. Dunne, P. McArdle, L. F. Jones. *Cryst. Eng. Comm*.,**2010**, 12, 59.

9. A Calix[4]arene 3d/4f magnetic cooler. G. Karotsis, M. Evangelisti, S. J. Dalgarno, E. K. Brechin. *Angew. Chem. Int. Ed*.,**2009**, 48, 9928.

8. Calix[4]arene- based single molecule magnets. G. Karotsis, S. J. Teat, W. Wernsdorfer, S. Piligkos, S. J. Dalgarno, E. K. Brechin. *Angew. Chem. Int. Ed*. **2009**, 48, 8285.

7. Supramolecular entanglement from interlocked molecular nanomagnets. C. Stoumpos, R. Inglis, G. Karotsis, L. F. Jones, A. Collins, S. Parsons, C. J. Milios, G. S. Papaefstathiou, E. K. Brechin. *Cryst. Growth and Des*. **2009**, 9, 24.

6. Molecular and supramolecular Ni(II) wheels from alpha-benzoin oxime. G. Karotsis, C. Stoumpos, A. Collins, F. White, S. Parsons, A. M. Z. Slawin, G. S. Papaefstathiou, E. K. Brechin. *Dalton Trans*. **2009**, 18, 3388.

5. Rare tetranuclear mixed-valent [$Mn^{II}2Mn^{IV}$] clusters as building blocks for extended networks. G. Karotsis, L. F. Jones, G. S. Papaefstathiou, A. Collins. S. Parsons, T. D. Nguyen, M. Evangelisti, E. K. Brechin. *Dalton Trans*. **2008**, 36, 4917.

4. Enhancing SMM properties via axial distortion of Mn-3(III) clusters. R. Inglis, L. F. Jones, G. Karotsis, A. Collins, S. Parsons, S. Perlepes, W. Wernsdorfer, E. K. Brechin. *Chem. Commun*., 2008, 45, 5924.

3. High temperature orbital order melting in $KCrF_3$ perovskite. S. Margadonna and G. Karotsis. *Journ.of Mater. Chem* **2007,** 17**,** 2013.

2. Cooperative Jahn-Teller distortion, phase transitions and weak ferromagnetism in the $KCrF_3$ perovskite. S. Margadonna and G. Karotsis. *J. Am. Chem. Soc* **2006**, 128, 16436.

1. Dynamic mechanical behaviour of polymers containing silica nanoparticles
A. Kraft, V. Arrighi, P.M.E. Adams, G. Karotsis, A. McAnaw, I.J. McEwen, L. Ragupathy, C. Waring. *Polymer Preprints* **2007,** *48 (2),* 203.

Conferences attended

"MAG-NET Magnetism Workshop", Edinburgh, U.K, August 2006 (poster presentation).

"**Royal Society of Chemistry Discussion Group Meetings: Inorganic Reaction Mechanisms Coordination Chemistry"**, University of Edinburgh, June 2008 (poster presentation).

"**11th ICMM Conference: International Conference on Molecule-based Magnets"**, Florence, Italy, September 2008 (poster presentation)